The University Of Sheffield.

Access To Thesis.

- A bound copy of every thesis which is accepted as worthy for a higher degree, must be deposited in the University of Sheffield Library, where it will be made available for borrowing or consultation in accordance with University Regulations.
- All students registering from 2008–09 onwards are also required to submit an electronic copy of their final, approved thesis. Students who registered prior to 2008–09 may also submit electronically, but this is not required.

Author: Ming-Huei Yen Dept: Materials Science and Engineering

Thesis Title: Self-assembly of minidendrons in 2D and 3D liquid crystal lattices and superlattices Registration No: 110209805

For completion by all students:

Submit in print form only (for deposit in the University Library): ☐

Submit in print form and also upload to the *White Rose eTheses Online* server: In full ☐

Edited eThesis ☐

Please indicate if there are any embargo restrictions on this thesis. Please note that if no boxes are ticked, you will have consented to your thesis being made available without any restrictions.

Embargo details: (complete only if requesting an embargo to either your print and/or eThesis)	Embargo required?		Length of embargo (in years)
Print Thesis	Yes ☐	No ☐	_____
eThesis	Yes ☐	No ☐	_____

Supervisor: I, the supervisor, agree to the named thesis being made available under the conditions specified above.

Name: Goran Ungar Dept: Materials Science and Engineering

Signed: ..... Date: .....

Student: I, the author, agree to the named thesis being made available under the conditions specified above.

I give permission to the University of Sheffield to reproduce the print thesis in whole or in part in order to supply single copies for the purpose of research or private study for a non-commercial purpose.

I confirm that this thesis is my own work, and where materials owned by a third party have been used copyright clearance has been obtained. I am aware of the University's *Guidance on the Use of Unfair Means* (www.sheffield.ac.uk/lets/design/unfair)

I confirm that all copies of the thesis submitted to the University (including electronic copies on CD/DVD) are identical in content.

Name: Ming-Huei Yen Dept: Materials Science and Engineering

Signed: ..... Date: .....

For completion by students also submitting an electronic thesis (eThesis):

I, the author, agree that the University of Sheffield's eThesis repository (currently WREO) will make my eThesis available over the internet via an entirely non-exclusive agreement and that, without changing content, WREO may convert my thesis to any medium or format for the purpose of future preservation and accessibility.

I, the author, agree that the metadata relating to the eThesis will normally appear on both the University's eThesis server and the British Library's EThOS service, even if the thesis is subject to an embargo. I agree that a copy of the eThesis may be supplied to the British Library.

I confirm that the upload is identical to the final, examined and awarded version of the thesis as submitted in print to the University for deposit in the Library (unless edited as indicated above).

Name: Ming-Huei Yen Dept: Materials Science and Engineering

Signed: ..... Date: .....

THIS SHEET MUST BE BOUND IN THE FRONT OF THE PRINTED THESIS BEFORE IT IS SUBMITTED

The University Of Sheffield.

Self-Assembly of Minidendrons in 2D and 3D Liquid Crystal Lattices and Superlattices

By:

Ming-Huei Yen

A thesis submitted in partial fulfilment of the requirements for the degree of Doctor of Philosophy

The University of Sheffield
Faculty of Engineering
Department of Materials Science and Engineering

May 2015

Abstract

Tapered mesogens self-assemble into supramolecular columns or spheres. The resulting supramolecules further form 2-D columnar phases or 3-D cubic phases. In this project, a series of alkali 3,4,5-trialkyloxybenzoate salts and their blends with n-alkanes are investigated by small angle X-ray scattering (SAXS), oriented fibre wide angle X-ray scattering (WAXS), and small angle neutron scattering (SANS) to reveal the packing mechanism.

The transition between two hexagonal columnar phases (the Colh-Colh transition) in sodium 3,4,5-tridodecyloxybenzoate salts (12-12-12Na) was found to be the result of conformation disorder of alkyl tails. From SAXS and WAXS experiments, in the low temperature Colh-**1** phase, the diameter of the columns is independent of temperature and there are four minidendrons in one of the supramolecular disks ("stratum") that stack up to form a column. Upon the transition to the high temperature Colh-**2** phase, the diameter of the columns suddenly shrinks, which is accompanied by a slight increase in spacing between two layers. The increase in gauche conformations in the alkyl chains makes the minidendrons expand laterally. Excess molecules are thus expelled and only three minidendrons remain in a stratum.

The absence of close packed structures in liquid crystal dendrimers is due to the inability of alkyl tails to reach the octahedral interstices. With the addition of n-alkane to 12-12-12Na, HCP phase is obtained. The same was observed in rubidium 3,4,5-tridodecyloxybenzoate salts (12-12-12Rb) + n-alkane. According to the electron density map and neutron scattering length density map, the free alkane segregates in the octahedral interstices. The first close packed structure in thermotropic liquid crystals is therefore stabilised.

In blends of lithium minidendrons with n-alkane, a 2-D hexagonal columnar superlattice is observed. It was found that two different sizes columns co-exist in the superlattice of *p*6*mm* symmetry. From neutron scattering length density maps it was concluded that the shortfall of narrow-column volume is compensated for by the free alkane. The lattice strain that would arise from non-equal column diameters is thus alleviated and the superlattice phase becomes stable in the blends.

Acknowledgements

First of all, I appreciate Prof. Goran Ungar and Dr. Xiangbing Zeng to offer me an opportunity for my PhD. Their knowledge and passion on science help me to overcome the problems in my research. I am also grateful to our previous and current group members, Dr. Feng Liu and Dr. Zhihong Chen. Their assistances and experiences always encourage me.

I would like to thanks Dr. Liliana Cseh for synthesis of the materials. I appreciate her brilliant work. Without her assistance, my research cannot go smoothly. Also, I need to thanks for Prof. Mehl providing space for my laboratory work.

Thanks for ILL (France) for providing the beamtime in the last three years. Also, I appreciate Dr. Patrick Baker in Department of Molecular Biology and Biotechnology to provide XRD tool time for my research.

Finally, I would like to thank my family. Without their support during my Phd, I cannot have the chance to finish my PhD.

Contents

Chapter 1 Introduction

1.1 Concept of Liquid Crystal

1.1.1 Liquid Crystalline Materials

Liquid crystalline materials are widely used in display technology due to their specific anisotropic optical and fluid properties[1]. Friedrich Reinitzer, seen as the discoverer of liquid crystal, observed and described a unique melting behaviour of a derivative of cholesterol in 1885[2, 3]. There are two melting points of this material. First it melts from solid state into a cloudy fluid at 145.5 °C. When the temperature is raised to 178.5 °C, the opaque fluid melts again into transparent liquid. Furthermore, this process is reversible on cooling. This peculiar phenomenon drew his attention. If the matter melts at 145.5°C from solid phase and turns into liquid phase at 178.5 °C, what is the phase in between?

Now, we know that this phase (or sometimes termed “mesophase”) is the liquid crystal phase. A matter in the liquid crystalline state would have some characteristics of a liquid or a crystal, but some of their behaviours are quite dissimilar. For instance, liquid crystals can flow like liquid but at the same time can possess long-range order, and unlike in a crystal, molecules in a liquid crystal may arrange only along certain direction(s). These unconventional properties are between that of liquid and crystal. That is reason why we call this state “liquid crystal”. To date, many organic materials (or mesogens) were found to form liquid crystal phases[4, 5]. Ultimately, the physical properties of a liquid crystal are determined by the structure of its constituent mesogens. The design of mesogens becomes an interesting task in investigating liquid crystals.

Main types of liquid crystals and their classification are introduced in the next section.

1.1.2 Liquid Crystal Phases

In 1922, Georges Friedel classified liquid crystals depending on their different type of ordered arrangement. He catalogued liquid crystals into three mesophases: nematic phase, smectic phase, and cholesteric phase[1, 2, 4, 6, 7].

The type of ordering is influenced by the intermolecular forces, which are determined by the chemical structure and shape of molecules/mesogens.

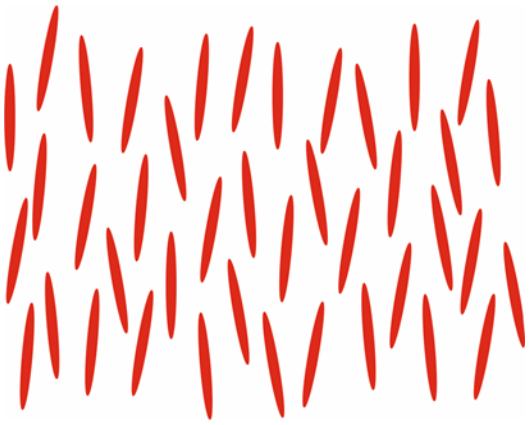

Figure 1.1. Arrangement of molecules in the nematic phase.

In the nematic phase, the molecules would align along one specific orientation. However, the arrangement of the molecules has no positional order. As shown in Figure 1.1, rod-like molecules in nematic phase tend to point in the same direction (along their long axis), hence the structure has 1-D long range orientational order. In other directions molecules are randomly oriented (or cylindrically averaged). There is no long range positional order in the structure either.

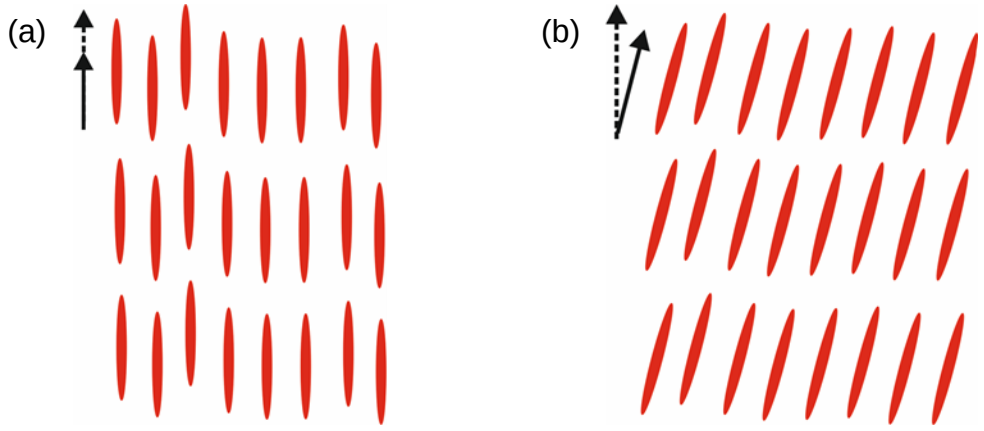

Figure 1.2. Molecular arrangement in the (a) smectic A and (b) smectic C phases.

The molecules in the smectic phases, on the other hand, form a periodic layered structure. In each layer, the molecules still align along certain direction and the structure hence has orientaional order as well. There is still no long range positional order within each individual layer, so the structure has only 1-D long range positional order of the layers. There are many different kinds of smectic phases that are observed having different degrees of order. Two of most commonly observed smectic phases are shown in Figure 1.2. In smectic A phase the orientation of the molecules is parallel to the layer normal, while in smectic C phase the molecular orientation is tilted to it.

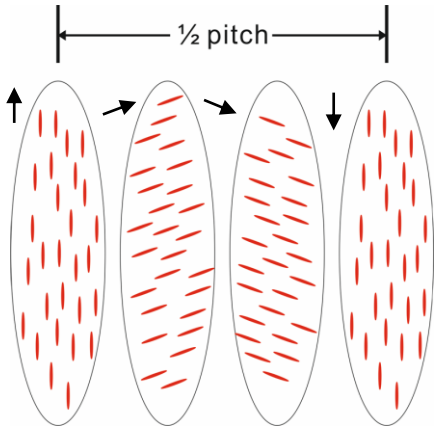

Figure1.3. Molecules alignment in the cholesteric phase.

The cholesteric phase, also called chiral nematic phase, was first observed in the cholesterol derivatives, which are chiral molecules. Figure 1.3 shows the arrangement of molecules in the cholesteric phase. In a thin strip the molecules aligns in one direction like in the nematic phase. However, the orientation of molecules between such strips twist due to the chirality of mesogens and consequently form a helical structure. That means the molecules on adjacent planes perpendicular to the helical axis will twist a little between each other. The distance along the helical axis between which the molecular direction rotate a full 360° is periodic and called “pitch”. The length of the pitch influences the optic properties of the cholesteric phase and normally changes with temperature.

There are still other liquid crystal phases such as blue phases and discotic phases[3, 4]. Blue phases are usually found in the temperature range between isotropic and chiral nematic phase[2]. The mesogens assemble 3-D cubic structure in the blue phase. The discotic phase is observed in disc-like mesogens[8-10]. The molecules form supramolecular columns and arrange into 1-D or 2-D periodic structures.

1.1.3 Thermotropic and Lyotropic Liquid Crystals

Liquid crystals can be also classified into thermotropic and lyotropic liquid crystals depending on the factors inducing them to form mesophases[1-3]. The mesogen generally consists of a rigid part and one/many flexible chains. The packing in the liquid crystal is mainly contributed by the rigid functional group(s) of the mesogen. The intermolecular force between the mesogens would be influenced by temperature. Thus, temperature is the most dominant factor in thermotropic liquid crystals. The mesogens arrange into a particular liquid crystal phase at a specific temperature range. Moreover, a thermotropic liquid crystal may show more than one kind of liquid crystal phase at different temperatures. Normally, thermotropic liquid crystals form crystalline phases at low temperature. The smectic phase is observed firstly with rising temperature followed by the nematic phase and, finally, the isotropic liquid.

The lyotropic liquid crystals are quite different from thermotropic ones. There are at least two components, normally one mesogen and the other solvent, in a lyotropic liquid crystal. Not only temperature, the concentration of the mesogen(s) plays an important role as well. Unlike thermotropic liquid crystals, they will show a particular liquid crystalline phase at certain concentration range. The solute molecules in lyotropic liquid crystals are typically bipolar. They have a hydrophilic (polar) head and a hydrophobic (nonpolar) tail. At low concentrations, the molecules normally form spherical micelles and assemble into 3-D cubic phases. When the concentration is increased, they form more loose structures like rod-shape or columnar micelles depending on the shape of mesogens. Both rod-shape and columnar micelles arrange into 2-D hexagonal lattice and form hexagonal columnar phase. At higher

concentrations, the lamellar phase is observed. In some mesogens, they would form inverse micelles at higher concentration. These inverse micelles would self-organise onto inverse phases, such as inverse hexagonal columnar phase and inverse micellar cubic phase.

1.1.4 Application of Liquid Crystals[1, 3]

Nowadays, liquid crystals are widely used in display technology. It mainly uses the electric-field sensitive liquid crystalline materials. Under different electric field, such mesogens show different alignment, hence their optical properties change. Accompanied with polarizers and colour filter, different colour can be shown on the display devices.

The thermotropic chiral liquid crystals can be used as thermometers due to their temperature sensitive characteristics. The pitch is varied at different temperature and thus different wavelength of light can be reflected at different temperature. Moreover, they can be used as failure detectors in semiconductors. The hot spot can be located by change of colour of coated liquid crystals. The lyotropic liquid crystals are used more in the biological field. For example, due to their amphiphilic properties, they could be carriers for drug delivery.

1.2 Dendrimeric Liquid Crystals

1.2.1 Dendrimers and Dendrons

Dendrimers are repeated hyper-branched (dendritic/tree-like) molecules, or supramolecules composed of such molecules held together by non-covalent bonds[11-13]. They are spherical-shape and symmetric around the core. Dendrons are also dendritic molecules. However, the dendron molecules have a single focal point[12-14]. The differences between a dendrimer and dendron are shown in Figure 1.4. The dendritic structure macromolecules were proposed by P. Flory in 1940s[13, 15]. However, the branched structure molecule was firstly prepared by divergent method reported by Fritz Vögtle only in 1978[13, 16, 17]. The convergent method to prepare dendrimers was introduced by Jean Fréchet in 1990[13, 14, 17, 18].

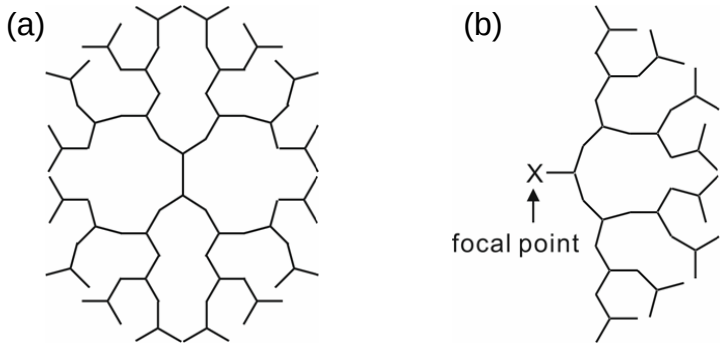

Figure 1.4. The schematic of (a) a dendrimer and (b) a dendron.

Now, these two methods are commonly used to prepare dendrimers or dendrons. The divergent method starts from an initiator core with multifunctional groups in the periphery. The growth of the core of dendrimer is the resultant of repetition of coupling and activation steps around the periphery functional groups, like a growing trunk (Figure 1.5(a)). For example, in synthesis of poly(propylene imine) dendrimer, the initiator core is $H_2N(CH_2)_4NH_2$. CH_2=CH-C≡N is added for the cyanoethylation reactions with amine groups of the core (Coupling step). After the coupling step, the cyanide groups at the periphery can be converted into amine groups (Activation step) for the growth of the next generation. The growth of each generation thus can be carried out stepwise. It

is easy to obtain a high molecular weight dendrimer/dendron. However, the number of coupling and activation reactions increases exponentially with generation. Defects or impurities therefore exist once incomplete growth or side reactions occur. Such imperfect dendrimers/dendrons are very difficult to eliminate from the system since their dimension is very similar to that of the perfect ones.

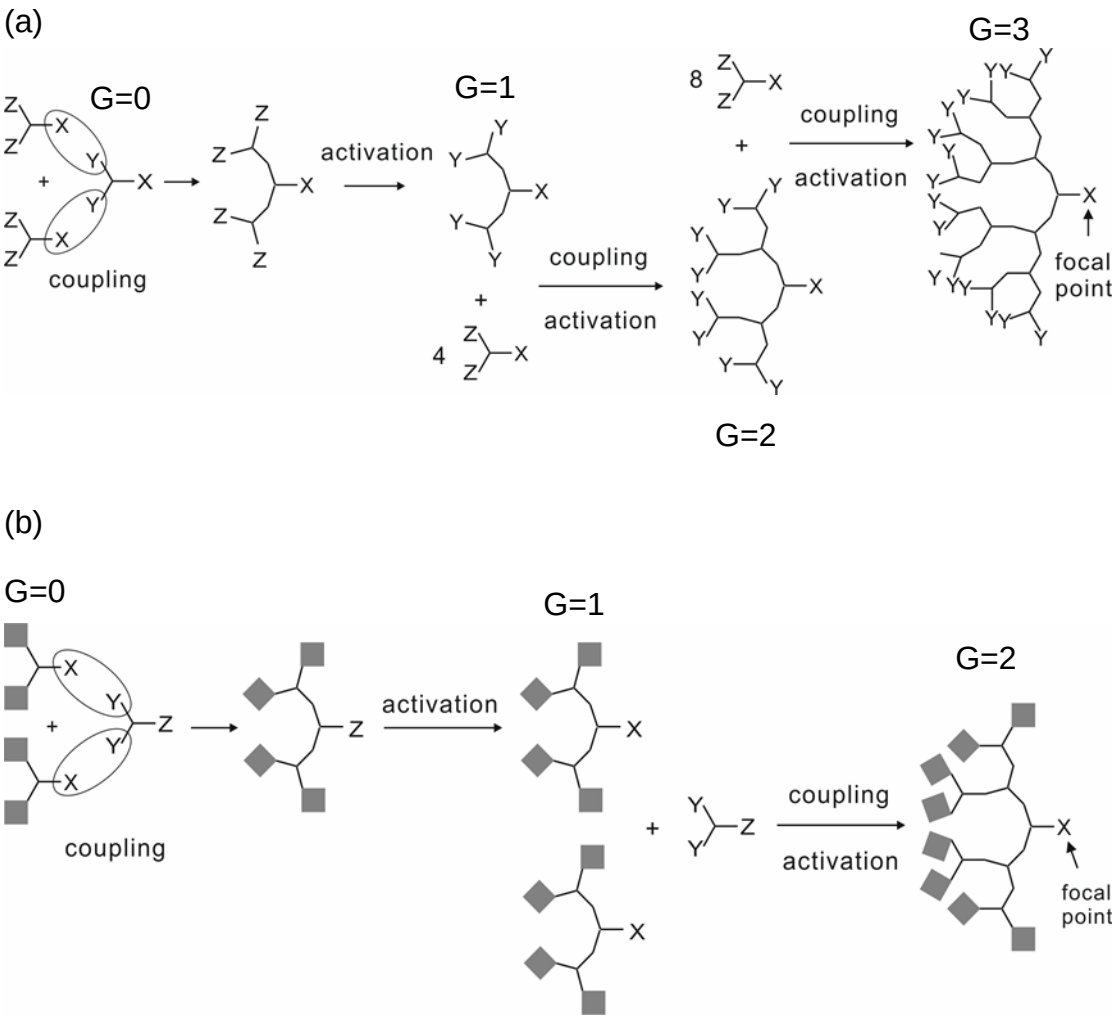

Figure 1.5. (a) Divergent synthesis method and (b) convergent method to prepare dendrimers/dendrons.

If in the divergent method the molecular tree is grown from the trunk to branches and then to leaves, in the convergent method it is grown from the leaves to

branches and then to the trunk. Instead of coupling reactions with monomers at the periphery of the dendrimer/dendron, the molecule grows in generation by reaction of the functional group at its focal point with the monomer (Figure 1.5(b)). After the coupling reaction, the functional group at the focal point of the dendrons can be activated for reactions to produce dendrons of next generation. The desired generation of the dendrons can be prepared by repetition of such coupling and activation steps. A dendrimer can be obtained by these dendrons attached to a multifunctional core at their focal points. This method provides more precise control and avoids incomplete or side reactions. The impurity or imperfect dendrimer can be purified much easier than that formed by divergent method. However, the molecular weight of the final product is limited due to steric effects.

The properties of the dendrimers or dendrons can be adjusted by modification of functional groups at the molecular surface, such as solubility, toxicity, crystallinity and chirality. Thus, they are now used as biomaterials like drug carriers and bio-sensors. Furthermore, the liquid crystalline dendrimeric materials are widely investigated. By adjusting the shape and the taper angle of the dendritic mesogens, they show different mesophase architecture. It can be achieved by control the branching groups, generation number of dendron, and apex groups[19].

1.2.2 Dendronized Molecules

Dendritic molecules can be classified as low molecular weight and high molecular weight ones. Dendrimers and dendrons are the low molecular weight ones. The high molecular weight species include dendronized polymer and hyperbranched polymer[13, 17, 20, 21]. Dendronized polymers are typically comb polymers, where the teeth of the comb are the dendron molecules. Dendronized polymer can be synthesised by two different ways.

Figure 1.6 shows the two synthetic routes of dendronized polymer. The monomer is modified and dendrons attached before polymerization by route (A). The defects of the dendrons or on the backbone can be avoided via route (A) since the monomer is dendronized firstly. However, it is hard to find a suitable

dendron which is stable enough during the polymerization. By route (B), the backbone of the polymer is prepared firstly. The dendrons will react at the anchor points on the backbone, either divergent or convergent method. The problem of this route is the defects or incomplete reaction during dendronization. Control the process of the divergent or convergent method of the dendrons plays an important role on this technique to obtain a perfect dendronized polymer.

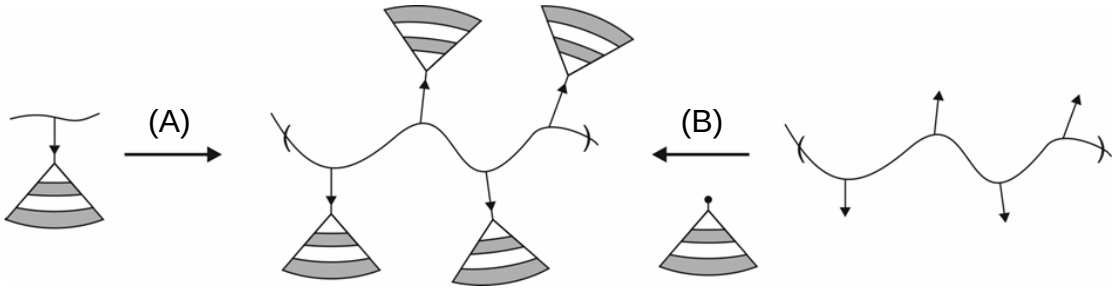

Figure 1.6. Synthesis procedure of dendronized polymer.

The shape and the rigidity of dendronized polymer can be tuned by the size of the attached dendron. A large dendron would cause steric repulsive force and that lead to the backbone suffering strain. In the extreme case, the polymer forms cylindrical structure in order to reduce the repulsive force. These cylinders further arrange into ordered structure such as 2-D columnar phases. The mesogenic dendrons can be also used for the dendronized polymer. When the attachment of the dendrons is designed loose on the backbone, the mesogenic groups self-assemble into ordered arrangement. The dendrons can be a modifier of the crystallinity and be used to design the desirable liquid crystalline phase.

It is interesting to control the desirable liquid crystalline phase by dendronization. Since the packing of the molecules influences their properties, the dendronization of semiconductor molecules leads to different electrical or optical characteristics. For example, the dendronized perylene bisimide (PBI) have different packing depending on the spacer length[22-25]. If close packing of the cores are achieved, higher charge mobility will result. The dendronized

cyclotriveratrylene (CTV) forms dendritic crown conformation and self-organise into 2-D columnar phase or 3-D cubic/tetragonal phase. Consequently, non-chiral or chiral dendronized CTV result in different chirality of the liquid crystal phases[26].

1.2.3 Dendron-Based Tapered Mesogen

Based on their shapes, mesogen can be divided into several categories[2, 12]. Calamitic mesogens are rod-like molecules which arrange into nematic or smectic liquid crystal phases. Discotic mesogens are disc-shaped. Typically, they will self-assemble into columnar supramolecules. These columnar supramolecules may form nematic phase or 2-D columnar phase. There are still other kinds of shapes of mesogen like banana-shaped and cone-like mesogens. Here, we are interested in the tapered mesogens which composed of dendron. These wedged molecules display different shape at different temperature range and self-assemble into different liquid crystal phase[19, 27-38].

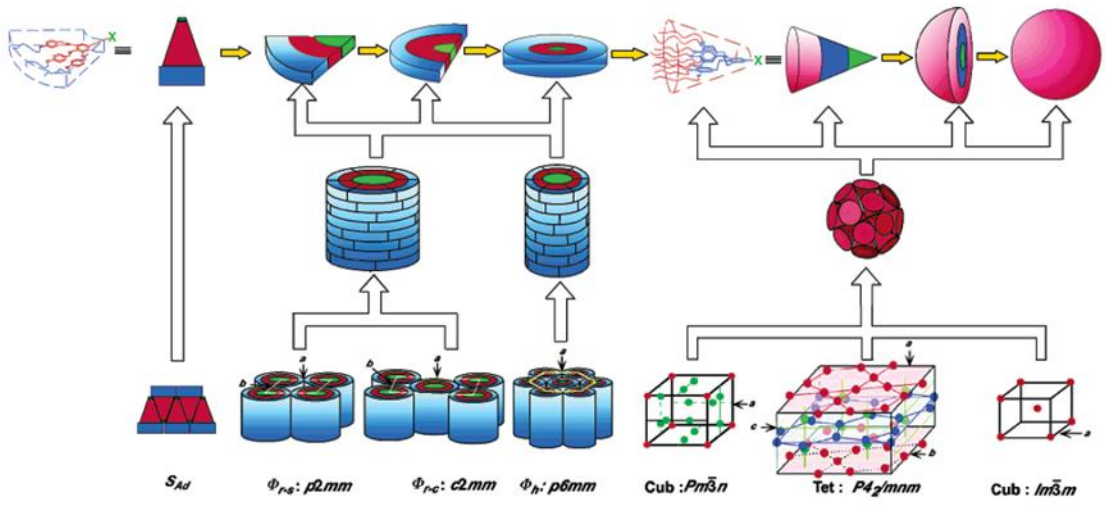

Figure 1.7. The different shapes of the dendron-based mesogen and the liquid crystal phase formed by dendron-based mesogen from low to high temperatures[31].

Figure 1.7 shows the different liquid crystalline phases formed by the dendron-based mesogens from low to high temperatures. At different temperatures, the mesogen displays different shapes, due to change of conformation of the aliphatic chains at periphery. At low temperatures, the wedged mesogens display smectic phases. When the temperature is increased, the shape of the tapered mesogens becomes more like a slice of pizza. The taper angle may increase with increasing temperature. The pizza-like molecules assemble into discs and form supramolecular columns. These columns further organise into columnar liquid crystals with 2-D symmetry, like *p*6*mm*, *p*2*mm*, and *c*2*mm*.

The shape of the dendron-based tapered mesogens become conical from pizza-like when the temperature rises even higher. The conical mesogens aggregate and form micellar spherical supramolecules. Like hard spheres, the spherical aggregates also self-organise into 3-D cubic or tetragonal liquid crystal phases. Generally, the $Pm\bar{3}n$ phase is observed at the lowest temperatures and the $Im\bar{3}m$ phase at highest temperatures. The driving force is to reduce the surface energy of the micellar supramolecules.

Recently, monodendrons drew much attention due to their richness of phase behaviour and potential application in electrolyte materials[39]. Kato's group reported that ionic transport in monodendron derivatives depends on liquid crystalline phase.[40, 41]. The monodendrons self-assemble into columnar phase or 3-D bicontinuous phase by micro-segregation of the ionic apex groups. The domains formed by ionic apex groups can be used as ionic pathways. Chvalun et al. reported the phase behaviour of benzenesulfonic acid derivatives influenced by the size of the apex group[42, 43]. Different size of the focal point leads to changes in the shape of monodendrons. They found that the shape of dendrons with smaller cations is more conical and these dendrons tend to form sematic phase at low temperatures and spherical aggregates packing into 3-D cubic phase at high temperatures. Bulky cations at focal groups make ordered and disordered columnar phases more stable. Moreover, low-symmetry monodendrons are also designed to investigate their phase behaviours[44, 45].

1.3 Objective of Project

Liquid crystal displays unique physical and optical properties due to their peculiar structure. In organic electronics, the packing of molecules influences the mobility and transportation efficiency of charge carriers. Dendronized compounds may pack in different structures due to the shape and the taper angle of the molecules. It can be achieved by modification of the branching pattern, control generation number of dendron, or changing the apex groups. The characteristics of these materials therefore relies on the packing of molecules.

The family of alkali gallate salts is an interesting and simple model for us to investigate the structure of dendron-based compounds. They are dendron-based tapered mesogens, and they display both 2-D columnar and 3-D cubic phases at different temperatures. In this work, interesting liquid crystal phases formed by the minidendrons and minidendron-alkane blends is resolved and explained. A combination of Small angle X-ray scattering (SAXS) and Wide angle X-ray scattering (WAXS) methods are used on powder and oriented fibre samples. While SAXS patterns show the 2-D and 3-D long range order of the liquid crystalline phases, WAXS patterns reveal more details about the packing of the molecules in them. In order to distinguish the added n-alkane from the alkyl tails of the minidendrons, small angle neutron scattering (SANS) technique will be employed as well in this work.

In our previous study of series alkali metal 3,4,5-tri(alkyloxy)benzoate salts, the lattice parameter is continuously decreasing with the rising temperature, however, this rule does not apply to lithium salts[46, 47]. The lattice parameter of lithium minidendrons is almost independent of temperature. Moreover, when the suitable amount of n-paraffin are mixed with lithium 3, 4–didodecyl–5–octadecyl-oxybenzonates salts (12-12-18Li)[47], a columnar superlattice phase was observed. We are interested in the specific behaviour of the lithium salts and wondering what the role of added n-alkane of the blends is in the superlattice phase. In this work we attempt to interpret the reason inducing superlattice structure and the molecular packing in the superlattice.

Another interesting aspect of the project is about sodium gallate salts. A discontinuous change of the lattice parameter is observed in sodium 3,4,5–tri(dodecyl-oxy)benzonates salts (12-12-12Na)[46] and sodium 3,4–didodecyl–5–octadecyl-oxybenzonates salts (12-12-18Na)[47], i.e. two adjacent hexagonal columnar phases in the heating scan. The lattice parameter in lower temperature hexagonal columnar phase (Colh**1**) is almost independent of temperature. However, the lattice parameter is suddenly dropped and continuously decreasing with rising temperature in the following high temperature hexagonal columnar phase (Colh**2**). These two phases display the same symmetry but the size of the columns are dramatically shrinking. The reason of the Colh-Colh phase transition are revealed by studying oriented samples.

The final part of the work is about the close packed structure. The inaccessibility of the close packed structure in the thermotropic liquid crystals is due to the octahedral interstices present in such structure is hard to reach. How to make the close packed structure possible becomes an interesting task to investigate. According to our previous work[47], when suitable amount of n-paraffin mixed with sodium minidendron salts and rubidium minidendron salts, hexagonal close packed (HCP) structure was observed. This is the first time that the close packed phase is obtained in the dendron-based tapered mesogen, and, in the thermotropic liquid crystals. This project has revealed how the close packed structure is stabilised, and how the close packed structure can be interpreted.

Reference:

1. http://plc.cwru.edu/tutorial/enhanced/files/textbook.htm.

2. Chandrasekhar, S., *Liquid crystals*. 2 ed.; Cambridge University Press: 1992.

3. http://en.wikipedia.org/wiki/Liquid_crystal.

4. Vertogen, G.; de Jeu, W. H., *Thermotropic liquid crystals, fundamentals*. Springer: 1987.

5. http://en.wikipedia.org/wiki/Mesogen.

6. *The molecular physics of liquid crystals*. Academic Press: 1979.

7. Demus, D.; Goodby, J.; Gray, G. W.; Spiess, H. W., *Handbook of liquid crystals*. WILEY VCH: 1998; Vol. 1-3.

8. Chandrasekhar, S.; Sadashiva, B. K.; Suresh, K. A., Liquid crystal of disc-like molecules. *Pramana* **1977,** 9, (5), 471-480.

9. Destrade, C.; Tinh, N. H.; Gasparoux, H.; Malthete, J.; Levelut, A. M., Disc-like mesogens - A classification. *Mol. Cryst. Liq. Cryst.* **1981,** 71, (1-2), 111-135.

10. Levelut, A. M., Structures of mesophases of disc-loke molecules. *J. Chim. Phys. Phys.-Chim. Biol.* **1983,** 80, (1), 149-161.

11. Bosman, A. W.; Janssen, H. M.; Meijer, E. W., About dendrimers: Structure, physical properties, and applications. *Chem. Rev.* **1999,** 99, (7), 1665-1688.

12. Donnio, B.; Buathong, S.; Bury, I.; Guillon, D., Liquid crystalline dendrimers. *Chem. Soc. Rev.* **2007,** 36, (9), 1495-1513.

13. Tomalia, D. A.; Christensen, J. B.; Boas, U., Dendrimers, dendrons, and dendritic polymers: discovery, applications, and the future. In Cambridge University Press: 2012.

14. Tomalia, D. A., starburst cascade dendrimers - fundamental building-blocks for a new nanocsopic chemistry set. *Adv. Mater.* **1994,** 6, (7-8), 529-539.

15. Flory, P. J., *Principles of polymer chemistry*. 4 ed.; Cornell University Press: 1953.

16. Mekelburger, H. B.; Jaworek, W.; Vogtle, F., Dendrimers, arborols, and cascade molecules - breakthrough into generations of new materials. *Angew. Chem. Int. Ed. Engl.* **1992,** 31, (12), 1571-1576.

17. Matthews, O. A.; Shipway, A. N.; Stoddart, J. F., Dendrimers - Branching out from curiosities into new technologies. *Prog. Polym. Sci.* **1998,** 23, (1), 1-56.

18. Grayson, S. M.; Frechet, J. M. J., Convergent dendrons and dendrimers: from synthesis to applications. *Chem. Rev.* **2001,** 101, (12), 3819-3867.

19. Crane, A. J.; Mueller, E. A., Global phase behaviour of polyphilic tapered dendrons. *Soft Matter* **2011,** 7, (16), 7465-7476.

20. Schluter, A. D.; Rabe, J. P., Dendronized polymers: Synthesis, characterization, assembly at interfaces, and manipulation. *Angew. Chem. Int. Ed.* **2000,** 39, (5), 864-883.

21. Frauenrath, H., Dendronized polymers - building a new bridge from molecules to nanoscopic objects. *Prog. Polym. Sci.* **2005,** 30, (3-4), 325-384.

22. An, Z. S.; Yu, J. S.; Jones, S. C.; Barlow, S.; Yoo, S.; Domercq, B.; Prins, P.; Siebbeles, L. D. A.; Kippelen, B.; Marder, S. R., High electron mobility in room-temperature discotic liquid-crystalline perylene diimides. *Adv. Mater.* **2005,** 17, (21), 2580-2583.

23. Percec, V.; Hudson, S. D.; Peterca, M.; Leowanawat, P.; Aqad, E.; Graf, R.; Spiess, H. W.; Zeng, X. B.; Ungar, G.; Heiney, P. A., Self-repairing complex helical columns generated via kinetically controlled self-assembly of

dendronized perylene bisimides. *J. Am. Chem. Soc.* **2011,** 133, (45), 18479-18494.

24. Percec, V.; Peterca, M.; Tadjiev, T.; Zeng, X. B.; Ungar, G.; Leowanawat, P.; Aqad, E.; Imam, M. R.; Rosen, B. M.; Akbey, U.; Graf, R.; Sekharan, S.; Sebastiani, D.; Spiess, H. W.; Heiney, P. A.; Hudson, S. D., Self-assembly of dendronized perylene bisimides into complex helical columns. *J. Am. Chem. Soc.* **2011,** 133, (31), 12197-12219.

25. Heek, T.; Fasting, C.; Rest, C.; Zhang, X.; Wurthner, F.; Haag, R., Highly fluorescent water-soluble polyglycerol-dendronized perylene bisimide dyes. *Chem. Commun.* **2010,** 46, (11), 1884-1886.

26. Percec, V.; Imam, M. R.; Peterca, M.; Wilson, D. A.; Heiney, P. A., Self-Assembly of Dendritic Crowns into Chiral Supramolecular Spheres. *Journal of the American Chemical Society* **2009,** 131, (3), 1294-1304.

27. Balagurusamy, V. S. K.; Ungar, G.; Percec, V.; Johansson, G., Rational design of the first spherical supramolecular dendrimers self-organized in a novel thermotropic cubic liquid-crystalline phase and the determination of their shape by X-ray analysis. *J. Am. Chem. Soc.* **1997,** 119, (7), 1539-1555.

28. Percec, V.; Cho, W. D.; Mosier, P. E.; Ungar, G.; Yeardley, D. J. P., Structural analysis of cylindrical and spherical supramolecular dendrimers quantifies the concept of monodendron shape control by generation number *J. Am. Chem. Soc.* **1998,** 120, (43), 11061-11070.

29. Percec, V.; Ahn, C. H.; Cho, W. D.; Jamieson, A. M.; Kim, J.; Leman, T.; Schmidt, M.; Gerle, M.; Moller, M.; Prokhorova, S. A.; Sheiko, S. S.; Cheng, S. Z. D.; Zhang, A.; Ungar, G.; Yeardley, D. J. P., Visualizable cylindrical macromolecules with controlled stiffness from backbones containing libraries of self-assembling dendritic side groups. *J. Am. Chem. Soc.* **1998,** 120, (34), 8619-8631.

30. Percec, V.; Cho, W. D.; Ungar, G.; Yeardley, D. J. P., Synthesis and structural analysis of two constitutional isomeric libraries of AB(2)-based monodendrons and supramolecular dendrimers. *J. Am. Chem. Soc.* **2001,** 123, (7), 1302-1315.

31. Percec, V.; Mitchell, C. M.; Cho, W. D.; Uchida, S.; Glodde, M.; Ungar, G.; Zeng, X. B.; Liu, Y. S.; Balagurusamy, V. S. K.; Heiney, P. A., Designing libraries of first generation AB(3) and AB(2) self-assembling dendrons via the primary structure generated from combinations of (AB)(y)-AB(3) and (AB)(y)-AB(2) building blocks. *J. Am. Chem. Soc.* **2004,** 126, (19), 6078-6094.

32. Zeng, X. B.; Ungar, G.; Liu, Y. S.; Percec, V.; Dulcey, S. E.; Hobbs, J. K., Supramolecular dendritic liquid quasicrystals. *Nature* **2004,** 428, (6979), 157-160.

33. Rosen, B. M.; Wilson, D. A.; Wilson, C. J.; Peterca, M.; Won, B. C.; Huang, C. H.; Lipski, L. R.; Zeng, X. B.; Ungar, G.; Heiney, P. A.; Percec, V., Predicting the structure of supramolecular dendrimers via the analysis of libraries of AB3 and constitutional isomeric AB2 biphenylpropyl ether self-assembling dendrons *J. Am. Chem. Soc.* **2009,** 131, (47), 17500–17521.

34. Ungar, G.; Percec, V.; Holerca, M. N.; Johansson, G.; Heck, J. A., Heat-shrinking spherical and columnar supramolecular dendrimers: Their interconversion and dependence of their shape on molecular taper angle. *Chem. Eur. J.* **2000,** 6, (7), 1258-1266.

35. Percec, V.; Holerca, M. N.; Uchida, S.; Cho, W. D.; Ungar, G.; Lee, Y. S.; Yeardley, D. J. P., Exploring and expanding the three-dimensional structural diversity of supramolecular dendrimers with the aid of libraries of alkali metals of their AB(3) minidendritic carboxylates. *Chem. Eur. J.* **2002,** 8, (5), 1106-1117.

36. Ungar, G.; Liu, Y. S.; Zeng, X. B.; Percec, V.; Cho, W. D., Giant supramolecular liquid crystal lattice. *Science* **2003,** 299, (5610), 1208-1211.

37. Ungar, G.; Zeng, X. B., Frank-Kasper, quasicrystalline and related phases in liquid crystals. *Soft Matter* **2005,** 1, (2), 95-106.

38. Li, Y. Y.; Lin, S. T.; Goddard, W. A., Efficiency of various lattices from hard ball to soft ball: Theoretical study of thermodynamic properties of dendrimer liquid crystal from atomistic simulation. *J. Am. Chem. Soc.* **2004,** 126, (6), 1872-1885.

39. Cho, B. K., Spontaneous bulk organization of molecular assemblers based on aliphatic polyether and/or poly(benzyl ether) dendrons. *Polym. J.* **2012,** 44, (6), 475-489.

40. Shimura, H.; Yoshio, M.; Hoshino, K.; Mukai, T.; Ohno, H.; Kato, T., Noncovalent approach to one-dimensional ion conductors: Enhancement of ionic conductivities in nanostructured columnar liquid crystals. *J. Am. Chem. Soc.* **2008,** 130, (5), 1759-1765.

41. Soberats, B.; Yoshio, M.; Ichikawa, T.; Taguchi, S.; Ohno, H.; Kato, T., 3D anhydrous proton-transporting nanochannels formed by self-assembly of liquid crystals composed of a sulfobetaine and a sulfonic acid. *J. Am. Chem. Soc.* **2013,** 135, (41), 15286-15289.

42. Shcherbina, M. A.; Bakirov, A. V.; Yakunin, A. N.; Beginn, U.; Yan, L. L.; Moeller, M.; Chvalun, S. N., The effect of the shape of the mesogenic group on the structure and phase behavior of 2,3,4-tris(dodecyloxy)benzenesulfonates with alkaline cations. *Soft Matter* **2014,** 10, (11), 1746-1757.

43. Shcherbina, M. A.; Bakirov, A. V.; Yan, L. L.; Beginn, U.; Zhu, X. M.; Moller, M.; Chvalun, S. N., Self-assembling of tapered benzenesulfonate-based dendrons with bulky aromatic focal groups. *Mendeleev Commun.* **2015,** 25, (2), 142-144.

44. Shcherbina, M. A.; Bakirov, A. V.; Yakunin, A. N.; Percec, V.; Beginn, U.; Moeller, M.; Chvalun, S. N., Self-assembling supramolecular systems of

different symmetry formed by wedged macromolecular dendrons. *Crystallogr. Rep.* **2012,** 57, (2), 151-168.

45. Lejnieks, J.; Zhu, X. M.; Wang, J. B.; Mourran, A.; Keul, H.; Moller, M.; Anokhin, D. V.; Ivanov, D. A., Self-assembly of a low-symmetry monodendron containing two asymmetrically linked molecular wedges. *Chemphyschem* **2010,** 11, (17), 3638-3644.

46. Liu, Y. S. Two- and three-dimensional liquid crystalline structures in self-assembled supramolecular dendrimers. University of Sheffield, 2004.

47. Chaiprapa, J. New supramolecular liquid crystal structures in wedge-shaped molecules. Univ. of Sheffield, 2012.

Chapter 2 X-rays Diffraction

2.1 Production of X-rays

X-rays is a kind of electromagnetic radiation and the wavelength range of X-rays is from 0.01 to 10 nm[1]. X-rays were discovered by Wilhelm Röntgen[2]. In 1895, he found that when cathode rays are produced, fluorescence was observed on a screen with barium platinocyanide coating. Moreover, Röntgen found many properties of X-rays, such as high penetrating ability, invisibility to human eyes, and so on.

Depending on the energy of X-rays, they could be divided into two different types. X-rays with higher energy, typically greater than 10 keV, are called hard X-rays. When the energy of X-rays is lower than 10 keV, they are called soft X-rays[3]. X-rays can be generated in two different ways. One is generated by synchrotron. The electrons are moving in circular motion in a storage ring and the velocity is approaching the speed of light. The applied magnetic field will change the direction of the electrons and the radiation is emitted. The other way is by the collision between the accelerated electron beam and the metal target. In a vacuum tube, the free electrons are released from the heated cathode. The free electrons then are accelerated by the high voltage and collide with the anode.

There are two different type of X-rays produced during the collision[4, 5]. One is continuous X-rays. Figure 2.1 (a) shows the generating procedure of continuous X-rays. The continuous X-rays is resulted from the deceleration of the incident electrons. When high speed electrons approach a high atomic number atom, they will be attracted by the proton of nucleus. The kinetic energy of the electrons is decreased and the loss energy will be converted into photon and X-rays are emitted. Since X-rays are resulted from the deceleration of the electrons, the continuous X-rays are also called “bremsstrahlung” or braking radiation.

The other one is characteristic X-rays. The process of producing characteristic X-rays is shown in Figure 2.1 (b). During the collision between incident electrons and target, the incident beam would hit the electron in an inner

orbital. The orbital electrons are therefore knocked out of inner shell and there is a hole left in the inner shell. The electron on the outer orbital then jumps in to fill the inner shell vacancy. The energy difference during this relaxation would be converted into photon and the characteristic X-rays are generated. Since the electrons on the specific orbital have specific energy level, the energy of the electrons jumping between orbitals is fixed. The spectrum of wavelength of characteristic X-rays thus is at few specific frequencies.

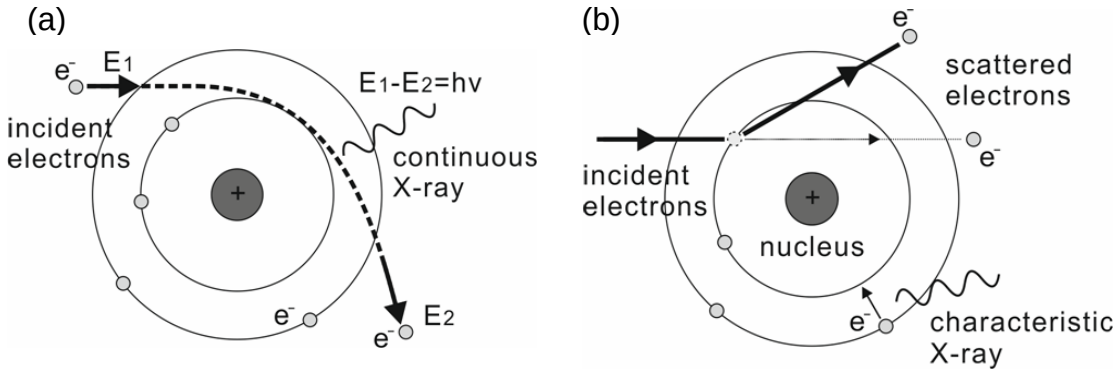

Figure 2.1 The procedure of generating (a) continuous X-rays and (b) characteristic X-rays

Elastic X-ray scattering is used in crystallography to reveal the structure of materials. The scattering condition is displayed in Figure 2.2. The moving direction of incident X-rays beam is along $\overrightarrow{k_0}$. At P, the incident beam is scattered with an angle φ. The vector $\vec{r}$ is defined the position of P. The moving direction of the scattered wave is thus changed and is along $\vec{k}$. The path difference between the scattered waves through an angle ψ at O and P is:

$$OA - PB = \vec{r} \cdot \vec{k} - \vec{r} \cdot \overrightarrow{k_0} = \vec{r} \cdot \left(\vec{k} - \overrightarrow{k_0}\right) \quad ----- \quad (2.1)$$

When the path difference is equal to the wavelength, the constructive interference of the scattered beams is observed.

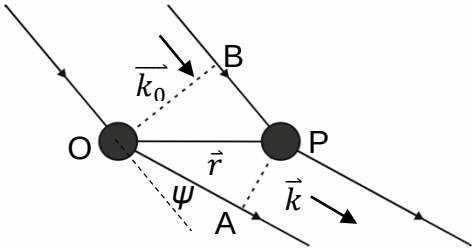

Figure 2.2 The incident and scattered beam directions and the path difference

In a crystal, there is long range order. The spacing of the periodic planes is fixed. When the spacing of the adjacent planes is equal to the wavelength or integer times of the wavelength, the constructive interference of the scattered X-rays would be produced. From the diffraction pattern, we can determine the structure of the material and identify a specific material. Bragg's Law is used to interpret the diffraction patterns. The details will be stated in the following section.

2.2 Geometry of Diffraction

2.2.1 Bragg's Law[6]

As mentioned in 2.1, X-rays are scattered by the electrons, most of the scattered waves interfere destructively. Only in some specific directions, the constructive interference occurs. These constructive waves are shown as spots and in a single crystal an array of spots, or diffraction pattern, is observed. The phenomenon was first discovered by von Laue. The diffraction pattern is most important in determining the structure of crystalline materials. It can be used to identify the materials as well. The diffraction pattern is interpreted by Bragg's law.

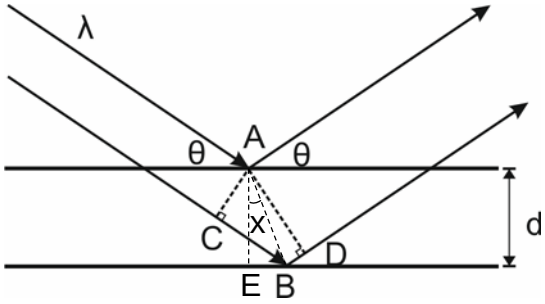

Figure 2.3 The illustration of Bragg diffraction

Figure 2.3 is the illustration of Bragg's condition. X-rays would interact with the electrons of the atoms and are scattered by the electrons. Laue suggested that crystals are periodic arrays of atoms along three different directions. The scattered angle of X-rays thus is considered in three dimensions. Bragg simplified the process of scattering. They supposed that the array of atoms in a crystal would act like periodic planes. Thus, when X-rays incidents on a crystal, the elastic scattering condition can be thought as X-rays reflected by a mirror. Referring to Figure 2.3, two parallel X-ray beams hit on two adjacent crystalline planes and the incident angle is θ. The spacing between these two planes is d. The path difference of the X-rays can be calculated by the incident angle and the spacing between two planes and is

$$BC + BD = AB[\sin(\theta + x) + \sin(\theta - x)]$$
$$= d\frac{1}{\cos x}[\sin(\theta + x) + \sin(\theta - x)] = 2d\sin\theta$$

The strongest constructive interference between the scattered X-rays is Bragg's condition. The path difference is integer times of the wavelength of incident beam, λ. The diffraction pattern thus can be interpreted by Bragg's law expressed as

$$n\lambda = 2d \sin\theta$$

, where n is an integer. The number n is related to the order of the spacing between two planes.

2.2.2 Reciprocal Space[6-8]

Reciprocal space is introduced to help handle the geometry of the scattered beam by a body. In Equation 2.1, the path difference between the incident and scattered beams is $\vec{r} \cdot (\vec{k} - \overrightarrow{k_0})$. The phase difference is then:

$$\frac{2\pi}{\lambda}\vec{r} \cdot (\vec{k} - \overrightarrow{k_0})$$

The vector *q* is defined by:

$$\vec{q} = \frac{2\pi}{\lambda}\left(\vec{k} - \overrightarrow{k_0}\right) \quad ----- \ (2.2)$$

Thus, the phase difference between the incident beam and the scattered beam is $\vec{r} \cdot \vec{q}$.

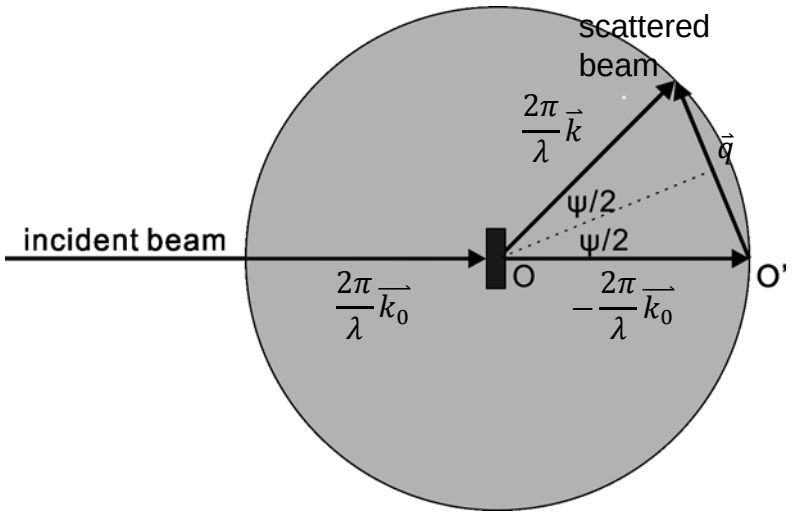

Figure 2.4 Definition of $\vec{q}$

Figure 2.4 shows the definition of $\vec{q}$ in Equation 2.2. In this figure, the origin of the *q* space is at O', which is λ/2π away from the origin of the real space, O. The amplitude of *q* vector is:

$$q = |\vec{q}| = \frac{4\pi}{\lambda}\sin\frac{\psi}{2} \quad -----(2.3)$$

The vector *q* thus is used to describe the direction and modulus of reciprocal point corresponding to the scattered beam.

The reciprocal lattice is introduced as a simple geometrical basis for interpreting X-rays and electron diffraction patterns. In the real space, a lattice can be defined by lattice parameters. The lattice vectors are $\vec{a}$, $\vec{b}$, and $\vec{c}$. The angles between pairs of vectors, $\vec{a}$ and $\vec{b}$, $\vec{a}$ and $\vec{c}$, and $\vec{b}$ and $\vec{c}$, are denoted as γ, β, and α respectively. In real space, the lattice points can be specified by three integer coordinative (*uvw*). The position of *j*th lattice point thus can be represented as:

$$\vec{r_j} = u_j\vec{a} + v_j\vec{b} + w_j\vec{c} \quad -----(2.4)$$

The reciprocal lattice can be defined by three vectors, $\overrightarrow{a^*}$, $\overrightarrow{b^*}$, and $\overrightarrow{c^*}$ as well. The angle between $\overrightarrow{a^*}$ and $\overrightarrow{b^*}$ is denoted as γ*, $\overrightarrow{b^*}$ and $\overrightarrow{c^*}$ is α*, and $\overrightarrow{a^*}$ and $\overrightarrow{c^*}$ is β*. The relationship between real lattice vector and reciprocal lattice vector is:

$$\begin{cases} \overrightarrow{a^*} = 2\pi\dfrac{\vec{b}\times\vec{c}}{\vec{a}\cdot(\vec{b}\times\vec{c})} \\ \overrightarrow{b^*} = 2\pi\dfrac{\vec{c}\times\vec{a}}{\vec{b}\cdot(\vec{c}\times\vec{a})} \\ \overrightarrow{c^*} = 2\pi\dfrac{\vec{a}\times\vec{b}}{\vec{c}\cdot(\vec{a}\times\vec{b})} \end{cases} \quad -----(2.5)$$

In the reciprocal lattice, each lattice point can be expressed as three integer coordinative (*hkl*). The *q* vector of the lattice point is thus given by:

$$\vec{q} = h\overrightarrow{a^*} + k\overrightarrow{b^*} + l\overrightarrow{c^*} \quad -----(2.6)$$

Thus, for a specific lattice point in the reciprocal lattice, considering both Equation 2.3 and 2.6, the Bragg angle of specific lattice plane is equal to *ψ/2*. The corresponding *d*-spacing of the lattice plane thus can be deduced by the modulus of *q*:

$$q = \frac{4\pi}{\lambda}\sin\frac{\psi}{2} = \frac{4\pi}{\lambda}\sin\theta\ ;\ \sin\theta = \frac{\lambda}{2d}$$

$$\therefore d = \frac{2\pi}{q} = \frac{2\pi}{\left|h\overrightarrow{a^*} + k\overrightarrow{b^*} + l\overrightarrow{c^*}\right|} = \frac{2\pi}{d^*} \quad -----(2.7)$$

From measuring the modulus of *q* of the diffraction patterns, the *d*-spacing in real space can be calculated.

2.2.3 Ewald Sphere[3, 6, 9]

Figure 2.4 shows that the scattered beam can be expressed by the corresponding vector $\vec{q}$ in the reciprocal space. Thus, measuring the intensity of the scattered X-rays can be seen as exploring the distribution of intensity in the reciprocal space at O' rather than at O, i.e. the real space. Nevertheless, not all of the reciprocal space is accessible to the experiments.

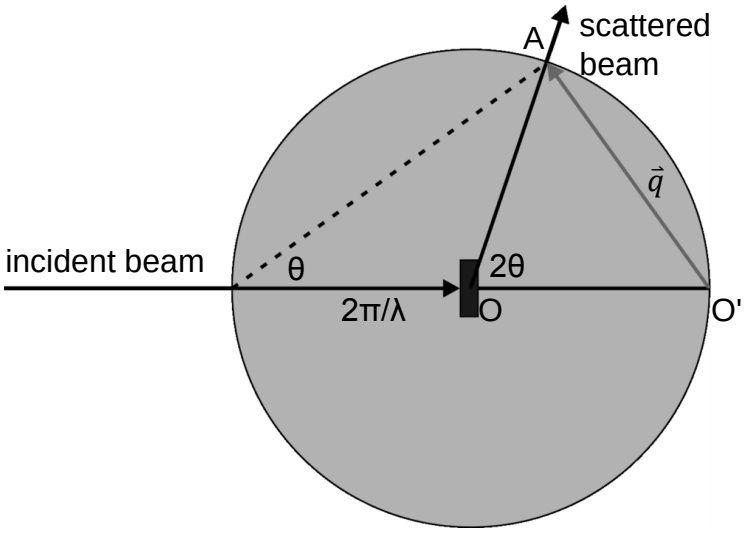

Figure 2.5 Ewald Sphere

Figure 2.5 displays X-rays incidents on a sample at the origin O. The origin of $\vec{q}$ is at O', which is the (000) reciprocal lattice point. If A is the (*hkl*) reciprocal lattice point, $\vec{q}$ is:

$$\overline{O'A} = \vec{q} = \frac{2\pi}{d_{hkl}}$$

When O' is 2 π /λ away from O along the incident beam direction,

$$\sin\theta = \frac{\frac{2\pi}{d_{hkl}}}{\frac{4\pi}{\lambda}}, \lambda = 2d_{hkl}\sin\theta$$

Thus, on the sphere whose radius is 2π/λ and the centre is at O, all points satisfy the Bragg's equation. This sphere is the so-called Ewald sphere. In the diffraction experiments, only the reciprocal lattice points that lie on the Ewald sphere will be recorded.

2.3 Scattering of X-rays[4, 6-8]

2.3.1 Scattered Wave as Fourier Transform

Figure 2.2 displays the condition of scattering of X-rays. The resultant intensity of the wave is equal to the square of its amplitude. Suppose the electron density at P is $\rho(\vec{r})$, the total number of electron in the volume unit is $\rho(\vec{r})\delta\vec{r}$. The amplitude of the scattered wave by the volume unit at P is:

$$\rho(\vec{r})\delta\vec{r}A_0p^{\frac{1}{2}}\frac{\mu_0}{4\pi}\frac{e^2}{mr}$$

, where A_o is the amplitude of the incident beam. As we know, not only the amplitude but the phase of the wave is scattered by the volume unit at P. The wave scattered by volume unit at P is thus given by:

$$\rho(\vec{r})\delta\vec{r}A_0p^{\frac{1}{2}}\frac{\mu_0}{4\pi}\frac{e^2}{mr}\exp(i\vec{r}\cdot\vec{q})$$

The scattered wave through angle φ in the whole body thus would be the integral result and is represented by:

$$F(\vec{q}) = A_0p^{\frac{1}{2}}\frac{\mu_0}{4\pi}\frac{e^2}{mr}\int\rho(\vec{r})\exp(i\vec{r}\cdot\vec{q})\,d\vec{r} \quad -----(2.8)$$

Since in X-ray diffraction, we consider only the relative intensity rather than the absolute value, the scattered wave can be simplified by

$$F(\vec{q}) = \int\rho(\vec{r})\exp(i\vec{r}\cdot\vec{q})\,d\vec{r} \quad -----(2.9)$$

The limit of the integration is the volume of the whole scattering sample. In X-ray scattering, the scattering sample is seen as the only source of the electron density. Thus, $F(\vec{q})$ is called the Fourier transform of the electron density.

2.3.2 Structure Factor

The crystals can be seen as the convolution of the motif and lattice. In a unit cell, it would contain more than one kind of atom, or group of atoms like molecules, or ions. In a diffraction experiment, not all of the electrons of an atom scatter X-rays in phase. Thus, the atomic scattering factor, f, is used to

define the correlation of all the scattering electrons in an atom. Suppose the electron density of an atom has spherical symmetry, the atomic scattering factor can be expressed as:

$$f(q) = \int_0^\infty 4\pi r^2 \rho(r) \frac{\sin qr}{qr} dr$$

The number of electrons with distance *r* from the centre of the atom is:

$$U(r) = 4\pi r^2 \rho(r)$$

The atomic scattering factor is given by:

$$f(q) = \int_0^\infty 4\pi r^2 \rho(r) \frac{\sin qr}{qr} dr = \int_0^\infty U(r) \frac{\sin qr}{qr} dr \quad ----- (2.10)$$

When $q = 0$,

$$f(0) = \int_0^\infty U(r) dr = Z$$

, where *Z* is the atomic number.

The Fourier transform of the crystal can be given by the transform of electron density of the content of the unit cell multiplied by the transform of translating lattice. Since the position of the lattice is fixed, we can only consider the transform of the electron density in a unit cell. The Fourier transform can be expressed as a summation which includes all atoms in a unit cell:

$$F(hkl) = \sum_j f_j \exp\left(i\vec{r_j} \cdot \vec{q}\right) = \sum_j f_j \exp[2\pi i\,(hu_j + kv_j + lw_j)]$$

$$= \sum_j f_j \cos\left[2\pi\left(hu_j + kv_j + lw_j\right)\right] + i \sum_j f_j \sin\left[2\pi\left(hu_j + kv_j + lw_j\right)\right] \quad - (2.11)$$

At a reciprocal lattice point, the value of the Fourier transform of the crystal is called structure factor. Depending on the characteristic of lattice type, the condition for extinction of reflection *(hkl)* can be calculated. The forbidden reflections in the specific space group are thus given. This is helpful in determining the space group of the material.

2.3.3 Determination of Electron Density

In X-ray diffraction experiment, X-rays are scattered by electrons and the scattered wave can be expressed as the Fourier transform of electron density (Equation 2.10). Based on the properties of the Fourier transform, the electron density can be given by the inverse Fourier transform of the scattered wave:

$$\rho(\vec{r}) = \int F(\vec{q}) \exp(-i\vec{r} \cdot \vec{q})\, d\vec{q} \quad ----- (2.12)$$

As we know, diffraction pattern is the map of intensity of the scattered waves. The scattered intensity, $I(\vec{q})$, can be expressed as:

$$I(\vec{q}) \propto F(\vec{q})F^*(\vec{q}) \quad ----- (2.13)$$

, where $F^*(\vec{q})$ is the complex conjugate of scattered wave $F(\vec{q})$. In a crystal, the intensity of a specific reciprocal lattice point, $I(hkl)$, is given by:

$$I(hkl) \propto F(hkl)F^*(hkl)$$

From Equation 2.12, $I(hkl)$ can be re-written as:

$$I(hkl) \propto \sum_j f_j \exp\left[2\pi i\left(hu_j + kv_j + lw_j\right)\right] \sum_j f_j \exp -\left[2\pi i\left(hu_j + kv_j + lw_j\right)\right]$$

$$= \left\{\sum_j f_j \cos\left[2\pi\left(hu_j + kv_j + lw_j\right)\right]\right\}^2 + \left\{\sum_j f_j \sin\left[2\pi\left(hu_j + kv_j + lw_j\right)\right]\right\}^2$$

$$= |F(hkl)|^2 \quad ----- \quad (2.14)$$

From measuring diffraction intensity, the modulus of the scattered wave can be obtained. However, the phase of the scattered wave is missing in the recorded diffraction pattern. That leads to difficulties in determining the electron density.

2.4 Small Angle Neutron Scattering

Neutron scattering technique is used to determine the position and the motion of atoms in condensed matter as well. While in X-ray scattering, X-rays are scattered by electrons, neutrons are scattered by atomic nuclei since the charge of neutrons is zero and the mass difference between electrons and neutrons is extremely large. The interaction between electrons and neutrons thus can be ignored.

The neutrons are produced by the nuclear fission chain reaction[10, 11]. When a neutron crashes into fissile isotope, the isotope would undergo nuclear fission and more neutrons are released during the reaction. Equation 2.16 gives an example of nuclear fission:

$$^{1}n + {}^{235}_{92}U \rightarrow {}^{236}_{92}U \rightarrow {}^{141}_{56}Ba + {}^{92}_{36}Kr + 3\,^{1}n + \gamma \quad ------ \ (2.15)$$

When a neutron is absorbed by uranium-235, which is a typical fissionable isotope, uranium-235 would turn into excited uranium-236. The excited uranium-236 would further split into two lighter elements, barium and krypton, and release three neutrons and gamma ray. The released neutrons would be absorbed by another uranium-235 and another fission occurs. The chain reaction proceeded continuously. This reaction is only terminated when fissionable isotope runs out or the released neutrons are absorbed by non-fissionable atoms.

According to their energy, neutrons can be sorted by two types: thermal and cold neutron. The energy of thermal neutrons is 5 ~ 100meV, and the wavelength is from 0.1 ~ 0.4 nm. The other one is cold neutron. Typically, the energy of cold neutron is around 0.1 ~ 10meV. The wavelength range would be from 0.4 to 3 nm. The wavelength of neutrons is comparable with the interatomic or intermolecular spacing so that neutron scattering is used to investigate the structure of materials as well. Furthermore, there are some advantages of the neutron scattering method.

Firstly, neutrons beams can penetrate the solid materials deeper than X-ray. Thus, bulky properties of materials can be investigated. Second, neutron can distinguish the isotopes since neutrons interact with nuclei instead of

electrons. Thirdly, X-rays are not very sensitive to the elements with smaller atomic number since these elements have fewer electrons. However, neutrons can still interact with the nuclei of the light elements. Moreover, a neutron has magnetic moment and its spin is equal to ½. The magnetic properties of materials can be revealed. Besides, the energy of neutrons has similar magnitude to atomic binding energy in solid state. The exchange of energy, such as molecular vibration, can be detected easily.

However, there are also some disadvantages in this technique. First, the signal is very weak since the source is very weak. Large amount of sample is required in this experiment and usually the exposure times are long. Some atoms have strong absorption of neutrons. Thus, this method cannot be applied on these elements. To investigate the structure at molecular level, both X-ray scattering and neutron scattering are employed. X-rays can first be used to resolve the structure of materials. And the details of the structure can be refined by applying neutron scattering since it can see light elements.

Reference

1. http://www.doitpoms.ac.uk/tlplib/xray-diffraction/index.php.

2. http://www-outreach.phy.cam.ac.uk/camphy/xraydiffraction/xraydiffraction_index.htm.

3. http://en.wikipedia.org/wiki/X-ray.

4. Klug, H. P.; Alexander, L. E., *X-ray diffraction procedures : for polycrystalline and amorphous materials*. Wiley: New York, 1954.

5. Henry, N. F. M.; Lipson, H.; Wooster, W. A., *The interpretation of X-ray diffraction photographs*. Macmillan & Co. LTD.: 1960.

6. Hammond, C., *The basics of crystallography and diffraction*. 3rd ed.; New York : Oxford University Press: 2009.

7. Hukins, D. W. L., *X-ray diffraction by disordered and ordered systems : covering X-ray diffraction by gases, liquids and solids and indicating how the theory of diffraction by these different states of matter is related and how it can be used to solve structural problems*. Pergamon: Oxford, 1981.

8. Roe, R. J., *Methods of X-ray and neutron scattering in polymer science* New York : Oxford University Press: 2000.

9. Ladd, M. F. C.; Palmer, R. A., *Structure determination by X-ray crystallography*. 2 ed.; Pleum Press: 1985.

10. http://en.wikipedia.org/wiki/Neutron_scattering.

11. http://www.ncnr.nist.gov/.

Chapter 3 Experimental Method and Analysis

3.1 Sample preparation

3.1.1 Alkali Metal 3,4,5-trialkyloxybenzoate Salts

Series of alkali metal 3,4,5-triakyloxybenzoate salts are synthesised by Dr. Liliana Cseh in the group of Professor G. H. Mehl at the University of Hull. The synthesis processes of these minidendrons are following the procedure in Figure 3.1.

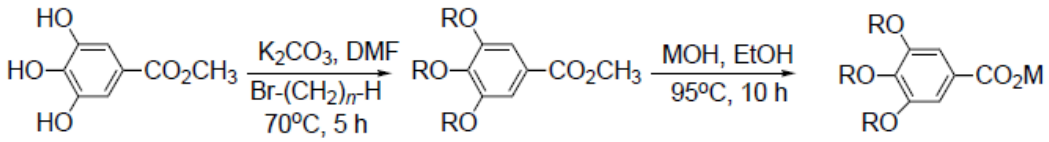

Figure 3.1 The synthesis of minidendrons, where M = Li, Na, Rb[1]

In this study, lithium 3,4,5-tri(dodecyloxy)benzoate salt (12-12-12Li), sodium 3,4,5-tri(dodecyloxy)benzoate salt (12-12-12Na), and rubidium 3,4,5-tri(dodecyloxy)benzoate salt (12-12-12Rb) are prepared for the experiments. In addition, different lengths of the alkyl tails are introduced into minidendrons. One tail in 12-12-12Li and 12-12-12Na is replaced by an octadecyl chain to obtain lithium 3,4-didodecyl-5-octadecyl-oxybenzoate salt (12-12-18Li) and sodium 3,4-didodecyl-5-octadecyl-oxybenzoate salt (12-12-18Na).

3.1.2 Minidendron-Alkane Blends

In our work, the main purpose is to distinguish the added n-alkane and the alkyl tails of the minidendrons. Thus deuterated long n-alkane, n-$C_{19}D_{40}$ (QMX Laboratories, 99% D), is used for the sample preparation.

In order to obtain homogeneous mixture, freeze-drying method is used rather than mixing the sample directly. Benzene is used as solvent to dissolve minidendrons and deuterated n-paraffin. The suitable amount of solvent and

solutes are put in a round-bottom flask. The ultrasonicator is used to help the solutes fully dissolve. Then, the solution is frozen in an ice bath. In order to prevent the inhomogeneous concentration in the solution during freeze, the as little solvent is used as possible. After the solution is entirely frozen, the flask is connected to the vacuum pump with cold trap and the pressure is pumped down to the triple point of benzene. The whole process is still in ice bath. Below the triple point, shown in Figure 3.2, the solid will sublime. Thus, the solvent can be extracted immediately from the solution and the concentration of the minidendron-alkane blends is uniform. After all of the solvent is extracted, the flask is refilled with nitrogen to avoid moisture uptake.

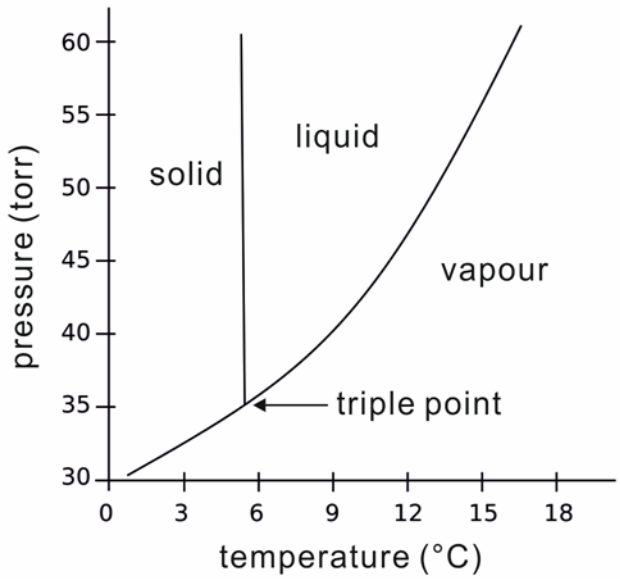

Figure 3.2 The phase diagram of benzene[2]

3.1.3 Fibre Preparation

In order to obtain samples with orientation, fibre specimens are prepared. The fibre sample is extruded from the powder. The powder sample is put in the metal mould with a pin hole. Then, temperature of the mould is adjusted to the desirable working condition. The working temperature must be as low as possible to prevent the fibre losing the orientation. The working temperatures will be stated in the following chapters.

3.2 X-ray Scattering

3.2.1 Powder Small Angle Scattering and Fibre Wide Angle Scattering[3-6]

The principle of small angle X-ray scattering and wide angle X-ray scattering is the same. The only difference is the detecting angle. Typically, scattered angle lower than 5˚ is small angle scattering. The scattered angle higher than 5˚ is wide angle scattering. However, the diffraction patterns are quite dissimilar resulted from powder and fibre sample. It is because the geometry of X-ray scattering is different.

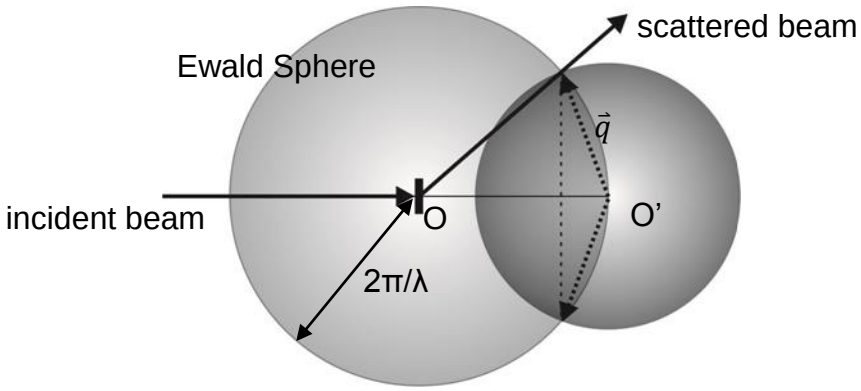

Figure 3.3 The geometry of powder X-ray scattering

Powder in X-ray scattering can be seen as polycrystal. There is no preferred orientation in the crystalline regions and the crystals are randomly oriented. Figure 3.3 shows the geometry of powder X-ray scattering. In a single crystal, the diffraction beam of specific plane is only along one direction. In the polycrystal, the orientation is random so the diffraction beam becomes spherical distribution and the radius is equal to *q*. The intersection area between the diffraction beams and Ewald sphere is a circle instead of a spot. Thus, the powder X-ray scattering pattern always shows concentric rings and it cannot distinguish the same family of planes or planes with the same *q* value.

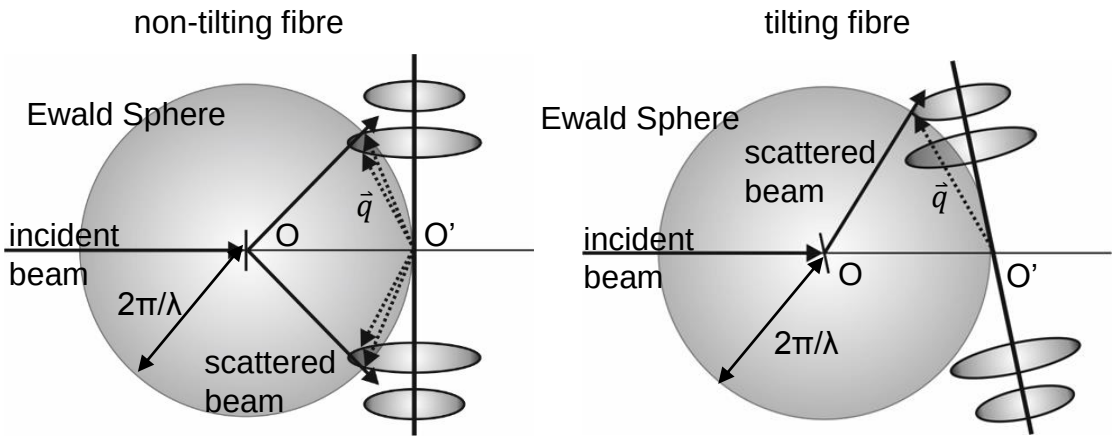

Figure 3.4 The geometry of fibre X-ray scattering

In fibre specimen, one crystallographic axis (e.g. *c*-axis) of all crystals would align along the axis of fibre. Figure 3.4 shows the geometry of fibre X-ray scattering. The scattered beam of a specific plane would form two symmetric circles, one on top and one at the bottom. The intersection of scattered beam and Ewald sphere shows four points when the *c*-axis is perpendicular with the incident beam. Normally, not all of the crystals are fully oriented and the reflection would look like an arc rather than a point. Furthermore, some diffractions intersect with Ewald sphere by changing the tilting angle of the fibre. In this way, may be only top or bottom circle would be recorded. In the fibre WAXS diffraction pattern, the reflections are grouped along layer lines, which come from the periodicity arrangement along fibre axis, i.e. *c* axis. The layer lines can be drawn and used to interpret the diffraction pattern.

3.2.2 X-ray Experimental Set-up

Powder SAXS experiments were done using the laboratory beamline. Beam delivery system was Xenocs GeniX which is using a FOX 3D CU_12-INF optic. The metal target is copper and the wavelength of Cu Kα X-ray is 1.5418 Å. Eurotherm temperature controller is installed and connected with the sample holder. The error of the temperature measurement can be controlled within ± 0.5ºC. The powder samples were put in 0.5mm glass capillaries for SAXS. Then, the opening of the capillary was sealed by torch. The prepared capillary

was put in sample holder which is then inserted in home-built temperature cell. Bruker Vantec 2000 microstrip 2-D detector is used to record the diffraction patterns.

Fibre WAXS experiments were performed using the X-ray facility at the Department of Molecular Biology and Biotechnology in the University of Sheffield[7]. The model of X-ray generator is Rigaku MicroMax 007 with copper rotating anode running at 40kV, 20mA. The beamline is equipped with the Osmic Varimax HighRes optics for the long unit cell crystal. The Oxford Cryosystems Cryostream nitrogen cooler is used as a temperature controller and the temperature range is from 100 ~ 400K. Fibre samples were packed into 0.5mm glass capillaries as well. The fibre axis can be tilted by changing the φ angle. Some diffraction patterns were recorded by tilting the fibre axis away from 90° to the beam by angle δ to allow meridional reciprocal point intersect the Ewald sphere (see Figure 3.4). The detector was Mar-research Mar345 image plate system.

3.3 Neutron Scattering

3.3.1 Experimental Facilities and Set-up[8]

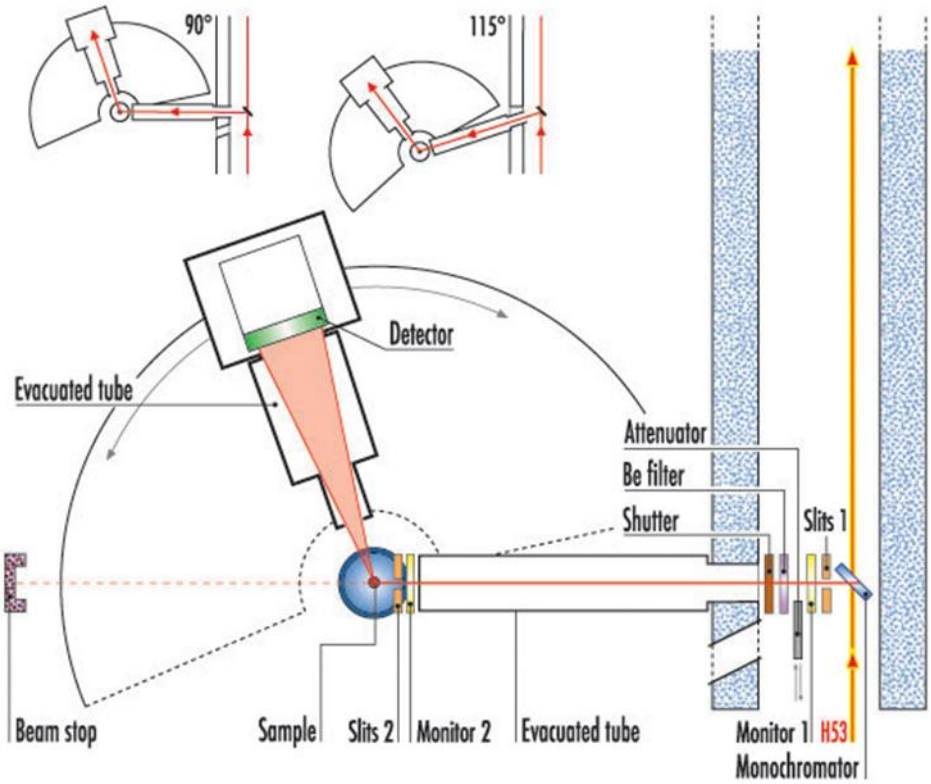

Figure 3.4 The layout of SANS instrument at Station D16[9]

Small angle neutron scattering (SANS) experiments were performed at Station D16 in Institut Laue-Langevin (ILL), France. The range of q can be from 0.01 – 2.5 $Å^{-1}$. Figure 3.4 shows the layout of the instrument. The primary beam is reflected by a focussing pyrolytic graphite monochromator. Two beam holes are at reflecting angle (take-off angle) of 90° and 115°. In this study, the take-off angle of 90° is chosen and the corresponding wavelength of the neutron beam is 4.7 Å. Eurothem temperature controller is installed and connected with the sample holder. The error of the temperature measurement can be controlled within ± 0.5°C. The powder samples are weighed and put in DSC pans for the experiments. The prepared DSC pan is put in the sample holder. A MILAND detector is used, which is a He gas-filled

proportional detector and the area is 320x320mm^2. Each pixel on the detector is equal to 1x1mm^2.

3.3.3 Reduction of Raw Data

The calibration data of D_2O for the instrument are firstly loaded before reduction of the raw data for the resolution and detector response. The detector was tilted at 13° for recording data and the detecting range is from 2.61° to 23.39°. Figure 3.5 shows the geometry of the set-up of the detector of neutron scattering.

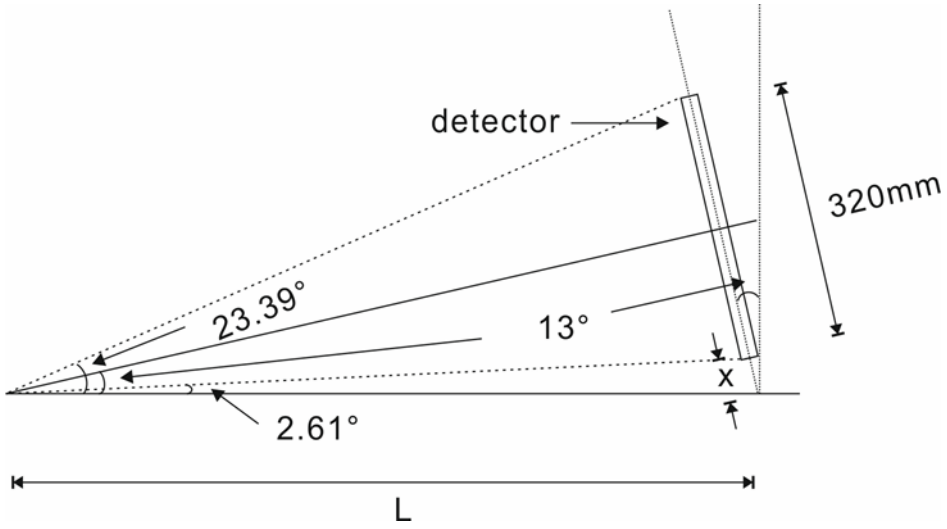

Figure 3.5 The geometry of the set-up of the detector of neutron scattering

The detector is shifting from the incident beam by *x*. Assuming the detector is a flat plate, the camera length can be calculated by:

$$\begin{cases} \tan 2.61° = \dfrac{x \cos 13° \,(1 + \tan 13° \tan 2.61°)}{L} \\ \tan 23.39° = \dfrac{(x + 320) \cos 13° \,(1 + \tan 13° \tan 23.39°)}{L} \end{cases} \quad -----(3.1)$$

The distance *x* is equal to 41.46 mm and the camera length, *L*, is equal to 895.55 mm. The corresponding tan2θ of each pixel (from *x* to *x*+320 mm) on the detector thus can be computed. Thus, the reciprocal space of the neutron

scattering can be determined. The *q* value of each reflection are measured and compared with the results of X-ray scattering.

3.4 Data Processing

3.4.1 Indexing of X-ray Patterns[4, 6, 10, 11]

The unit cell of the sample can be determined by indexing the diffraction patterns. Firstly, the recorded 2-D patterns are needed to transform into 1-D scans by FibreFix program. Then, the coordinates of the detector are needed to be converted to reciprocal coordinates by calibration. The sample we used for the calibration was n-tetracontane powder ($C_{40}H_{82}$), which is purchased from SIGMA chemical company (99% purity). The powder was packed into glass capillary. The $d_{(002)}$ of $C_{40}H_{82}$ is equal to 52.8 Å. The distance between sample and detector (camera length) can be calculated referring to Figure 3.6:

$$\begin{cases} \tan 2\theta = x/L \\ \lambda = 2d \sin\theta \end{cases} \rightarrow L = \frac{x}{\tan[\sin^{-1}(\lambda/2d)]} \quad ------ \quad (3.2)$$

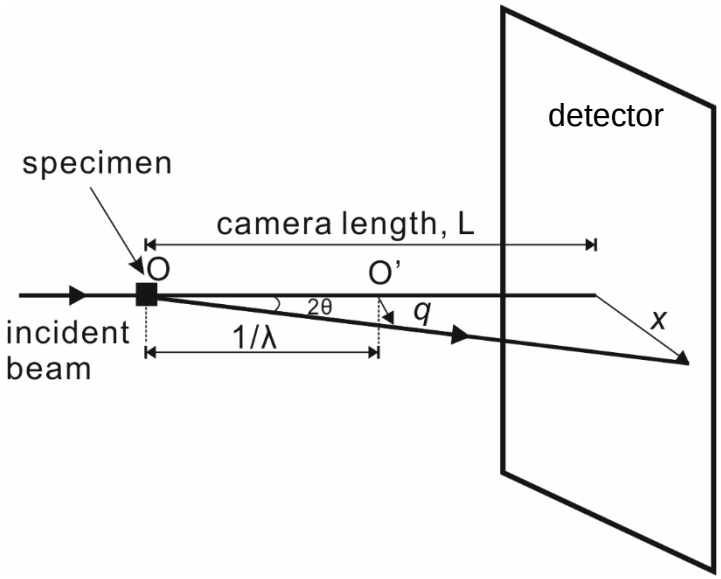

Figure 3.6 Geometry of X-ray scattering

From the distance from centre to the reflection divided by camera length, the scattering angle 2θ at any place on the pattern can be calculated. The corresponding q value can be computed by

$$q = \frac{4\pi \sin\theta}{\lambda}$$

The q value of individual peaks can be measured. As we know, q is equal to ($h\overrightarrow{a^*}$+$k\overrightarrow{b^*}$+$l\overrightarrow{c^*}$), the square of q is:

$$q_{(hkl)}^2 = \overrightarrow{q_{(hkl)}} \cdot \overrightarrow{q_{(hkl)}} = \left(h\overrightarrow{a^*} + k\overrightarrow{b^*} + l\overrightarrow{c^*}\right) \cdot \left(h\overrightarrow{a^*} + k\overrightarrow{b^*} + l\overrightarrow{c^*}\right)$$
$$= h^2a^{*2} + k^2b^{*2} + l^2c^{*2} + 2hka^*b^* \cos\gamma^* + 2klb^*c^* \cos\alpha^*$$
$$+ 2hla^*c^* \cos\beta^* \quad -----(3.3)$$

Considering the ratio of q of the first few peaks, the peaks can be indexed. The crystal system of the specimen thus is determined and the lattice parameters are obtained. The higher order peaks can further be indexed using the lattice parameters and q values.

3.4.2 Reconstruction of Density Maps[4, 6, 12-14]

Both electron density and neutron scattering length density maps can be reconstructed from the diffraction pattern. In 2.3.3, we mentioned that the electron density can be determined by inverse Fourier transformation of the scattered wave. However, there are two problem encountered during deduction of electron density. The modulus of the scattered wave can be obtained from the recorded intensity, however, the phase is missing (the "phase problem"). Another problem is that we cannot tell apart the moduli $F(\vec{q})$ and $F(-\vec{q})$.

Fortunately, in this study, all liquid crystal phases for which we have tried to reconstruct density maps are centrosymmetric. From Equation 2.10, the Fourier transform of the scattered wave can be re-written as:

$$F(\vec{q}) = \int_{-\infty}^{\infty} \rho(\vec{r}) \exp(i\vec{r} \cdot \vec{q})\, d\vec{r} = \int_{-\infty}^{0} \rho(\vec{r}) \exp(i\vec{r} \cdot \vec{q})\, d\vec{r} + \int_{0}^{\infty} \rho(\vec{r}) \exp(i\vec{r} \cdot \vec{q})\, d\vec{r}$$
$$= \int_{0}^{\infty} \rho(-\vec{r}) \exp(-i\vec{r} \cdot \vec{q})\, d\vec{r} + \int_{0}^{\infty} \rho(\vec{r}) \exp(i\vec{r} \cdot \vec{q})\, d\vec{r}$$

In a crystal with a centre of symmetry, suppose the centre of symmetry is set as the origin of the coordinates. The electron density at *(x,y,z)* should be identical with the electron density at *(-x,-y,-z)*, i.e. $\rho(\vec{r}) = \rho(-\vec{r})$. Furthermore, the modulus of $F(\vec{q})$ and of $F(-\vec{q})$ is hence identical. The intensity $I(\vec{q})$ is the

same as $I(-\vec{q})$. The Fourier transform of the scattered wave can be expressed as:

$$F(\vec{q}) = \int_0^\infty \rho(-\vec{r}) \exp(-i\vec{r} \cdot \vec{q})\, d\vec{r} + \int_0^\infty \rho(\vec{r}) \exp(i\vec{r} \cdot \vec{q})\, d\vec{r}$$

$$= \int_0^\infty \rho(\vec{r}) \exp(-i\vec{r} \cdot \vec{q})\, d\vec{r} + \int_0^\infty \rho(\vec{r}) \exp(i\vec{r} \cdot \vec{q})\, d\vec{r}$$

$$= 2\int_0^\infty \rho(\vec{r}) \cos(\vec{r} \cdot \vec{q})\, d\vec{r} \quad ----- \ (3.6)$$

The imaginary part of the scattered wave is zero and $F(\vec{q})$ must be real when $\rho(\vec{r})$ is centrosymmetric. When the value of $F(\vec{q})$ is positive, the phase is zero, when it is negative the phase is π.

From Equation 2.11 and 2.12, the electron density can be determined by:

$$\rho(uvw) = \int F(q) \exp(-i\vec{r} \cdot \vec{q})\, d\vec{q} = \frac{1}{V}\sum_j F(hkl) \exp\left(-i\vec{r_j} \cdot \vec{q}\right)$$

$$= \frac{1}{V}\sum_j F(hkl) \exp[-2\pi i\,(hu_j + kv_j + lw_j)]$$

Considering the distribution of electron in the molecules, the preferable phase combination can be decided. The density maps from the diffraction patterns can be reconstructed.

Neutron scattering length density map can be reconstructed by a similar method. The scattering length is determined by inverse Fourier transform of the scattered wave. In a centrosymmetric phase, only phases zero or π are allowed. The preferred phase combination is chosen based on the distribution of scattering length density of the molecules.

Reference:

1. Percec, V.; Holerca, M. N.; Uchida, S.; Cho, W. D.; Ungar, G.; Lee, Y. S.; Yeardley, D. J. P., Exploring and expanding the three-dimensional structural diversity of supramolecular dendrimers with the aid of libraries of alkali metals of their AB(3) minidendritic carboxylates. *Chem. Eur. J.* **2002,** 8, (5), 1106-1117.

2. http://en.wikipedia.org/wiki/Benzene.

3. Klug, H. P.; Alexander, L. E., *X-ray diffraction procedures : for polycrystalline and amorphous materials*. Wiley: New York, 1954.

4. Hukins, D. W. L., *X-ray diffraction by disordered and ordered systems : covering X-ray diffraction by gases, liquids and solids and indicating how the theory of diffraction by these different states of matter is related and how it can be used to solve structural problems*. Pergamon: Oxford, 1981.

5. Hammond, C., *The basics of crystallography and diffraction*. 3rd ed.; New York : Oxford University Press: 2009.

6. Ladd, M. F. C.; Palmer, R. A., *Structure determination by X-ray crystallography*. 2 ed.; Pleum Press: 1985.

7. https://www.shef.ac.uk/mbb/research/facilities/xtal/index.

8. http://www.ill.eu/.

9. http://www.ill.eu/instruments-support/instruments-groups/instruments/d16/description/instrument-layout/

10. Henry, N. F. M.; Lipson, H.; Wooster, W. A., *The interpretation of X-ray diffraction photographs*. Macmillan & Co. LTD.: 1960.

11. Mirkin, L. I., *Handbook of X-ray analysis of polycrystalline materials*. Consultants Bureau: New York, 1964.

12. http://plc.cwru.edu/tutorial/enhanced/files/textbook.htm.

13. http://www.doitpoms.ac.uk/tlplib/xray-diffraction/index.php.

14. http://www-outreach.phy.cam.ac.uk/camphy/xraydiffraction/xraydiffraction_index.htm.

Chapter 4 Hexagonal Columnar-Hexagonal Columnar Phase Transition

4.1 Introduction

A series of alkali metal 3,4,5-tri(alkyloxy)benzoate salts was investigated by Small Angle X-ray Scattering (SAXS). The lattice parameter decreases with rising temperature in most of these minidendrons, no matter whether in the 2-D columnar phase or in a 3-D cubic phase[1-3]. Nevertheless, in sodium and potassium salts, a peculiar behaviour was observed[3, 4].

E.g. in the first heating scan of sodium 3,4,5-tri(dodecyloxy)benzoate salt (12-12-12Na)[3], the lattice parameter of the hexagonal columnar phase (Colh-**1**), which follows a rectangular columnar phase, is independent of temperature until a first-order phase transition at which a jump occurs in the diameter of the columns. The minidendrons still form a columnar phase with the same *p*6*mm* symmetry. The high-temperature hexagonal columnar phase (Colh-**2**) is obtained. However, the lattice parameter drops abruptly at the phase transition temperature. Moreover, the lattice parameter continues to decrease as temperature increases further.

This hexagonal columnar to hexagonal columnar (Colh-Colh) phase transition was also observed in other sodium minidendrons. In sodium 3,4,5-tri(tetradecyloxy)benzoate salt (14-14-14Na)[3] and sodium 3,4-didodecyl-5-octadecyl-oxybemzoate salt (12-12-18Na)[4], there is also a downward jump in lattice parameter at the Colh–Colh phase transition. Before the phase transition, the diameter of the columns in the low temperature Colh phase is independent of temperature. In the high temperature Colh phase, the diameter of the columns continues to decrease with increasing temperature.

In the work reported by Shcherbina et al.[5], they found an order-disorder columnar phase transition in sodium, potassium, and caesium salts of 2,3,4-tridodecyloxybenzenesulfonic acid. The meridional reflection in the WAXS pattern was absent in the disordered columnar phase. The order-disorder

transition is accompanied by a drop between the diameters of the columns. The intensity ratio of reflections in these two phases is also different.

However, the reason behind the discontinuous Colh–Colh phase transition remains unclear. In this chapter, we attempt to find an explanation for the Colh–Colh phase transition. Two kinds of samples, sodium 3,4,5-tri(dodecyloxy)benzoate salt (12-12-12Na) and sodium 3,4-didodecyl-5-octadecyl-oxybenzoate salt (12-12-18Na) are investigated. The chemical structure of 12-12-12Na and 12-12-18Na is displayed in the Scheme 4.1.

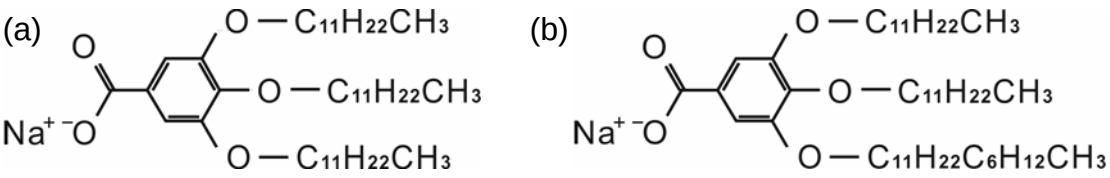

Scheme 4.1. The chemical structure of (a) 12-12-12Na and (b) 12-12-18Na

The size of the columns should be related to the packing of the molecules and the number of dendrons in the columnar cross-section. Oriented fibre WAXS experiments are applied in order to obtain that number. By fibre WAXS, it should be possible to obtain the missing information, i.e. the thickness of a single stratum in the columnar supramolecules. In addition, through interpreting the WAXS patterns, the packing mode of the minidendrons can be revealed[6-8]. That would be helpful to explain the Colh–Colh phase transition. Furthermore, molecular models of the two Colh phases are constructed using Materials Studio. The constructed models are examined by Cerius2 to simulate the fibre diffraction patterns. The simulation results are compared with the experimental ones to see how the packing of the molecules changed during the phase transition.

4.2 Experiments

Materials

The synthesis of 12-12-12Na and 12-12-18Na samples are described in Chapter 3.1.1.

The oriented fibres were prepared by extrusion following the procedure in Chapter 3.1.3. The extrusion temperature used for 12-12-12Na was 60 °C, The working temperature of preparing and that for 12-12-18 was 50 °C.

The powder samples and fibre samples were put in capillaries for both SAXS and WAXS experiments. The procedure of specimen preparation was described in Chapter 3.2.2.

Methods

The details of both the powder SAXS and fibre WAXS experiments are given in Chapter 3.2.2.

The details of data reduction of both SAXS and WAXS is following the method mentioned in Chapter 3.4.1.

The simulation is done in two parts. First, Materials Studio is used for building the molecules and the unit cell. The model is then built by putting the molecules in the unit cell.

4.3 Results and Discussion

The powder SAXS experiments on 12-12-12Na were performed by Yongsong Liu[3]. The results are displayed in Figure 4.1. There is an obvious jump in d-spacing between reflections $(10)_{Colh\text{-}1}$ and $(10)_{Colh\text{-}2}$. The lattice parameter in the two Colh phases are shown as a function of temperature in Figure 4.2. The change in lattice parameter indicates the change of the diameter of the columns. In Figure 4.2, we can see that the lattice parameter is independent of temperature in the Colh-**1** phase, i.e. the diameter of the columns is fixed in the low temperature Colh-**1** phase. However, the lattice parameter drops by around 8% (from 38.8 Å to 35.6 Å) when the phase changes into Colh-**2** phase. That implies the composition of the columns in the Colh-**1** and Colh-**2** is different. Interestingly, the lattice parameter continues to decrease as the temperature increases beyond the transition. However the slope of that decrease levels off. Such behaviour is typical of first order transitions with a pretransitional effect. Similar behaviour is exhibited e.g. by a real gas below but not far from the critical pressure, following the van der Waals equation. There the increase in volume can show both pretransitional and post-transitional accelerated increase on both sides of the first-order liquid-gas transition.

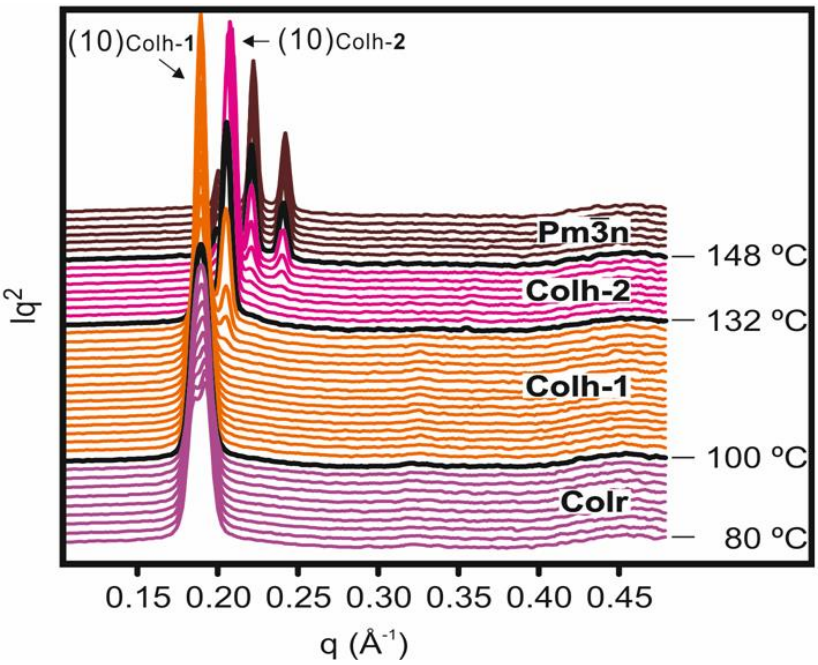

Figure 4.1 SAXS traces of 12-12-12Na in the first heating scan by Yongsong Liu[3]

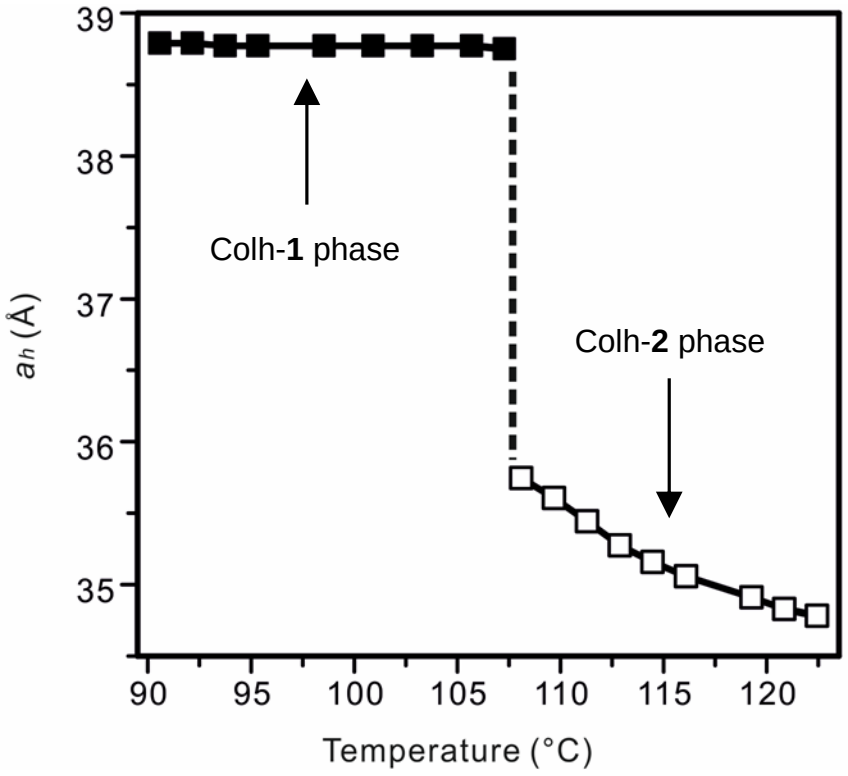

Figure 4.2 The lattice parameter of 12-12-12Na in the Colh phases at different temperatures (measured by Yongsong Liu)[3]

Since the LC columns consist of discrete minidendrons, we supposed that the size difference should be related to the number of molecules in each stratum of the columns. The number of molecules in a stratum in the hexagonal columnar phase can be computed by:

$$n = \frac{\sqrt{3}}{2} {a_h}^2 c \cdot \frac{\rho}{M} \cdot N_A \quad -----(4.1)$$

, where a_h is the lattice parameter in the Colh phase, *c* is the thickness of a single stratum, *ρ* is the density of the sample, *M* is the molecular weight, and N_A is the Avogadro's number.

However, the thickness of a single layer cannot be obtained from the powder SAXS patterns. Thus, oriented fibres were prepared for WAXS experiments. Figure 4.3 shows WAXS patterns of 12-12-12Na in the different phases put side-by-side for easy comparison. The reflections on the equator arise from lateral correlations between the columns in the 2-D columnar phase. The ratio

of the square of *q* value of the first three reflections is 1:3:4, which confirms that the phase has *p*6*mm* symmetry. On the meridian, the outer diffuse reflection results from the packing of the alkyl tails of the minidendrons. There is no clear spacing of the aliphatic periphery between two adjacent layers. The average spacing of the aliphatic tails is 4.5 Å. The outer sharp reflection near the meridian is caused by the correlation between aromatic cores of the minidendrons. The π-π stacking between the benzene rings makes a clear periodic spacing between two adjacent layers. The spacing of the aromatic cores is equal to 3.7 Å.

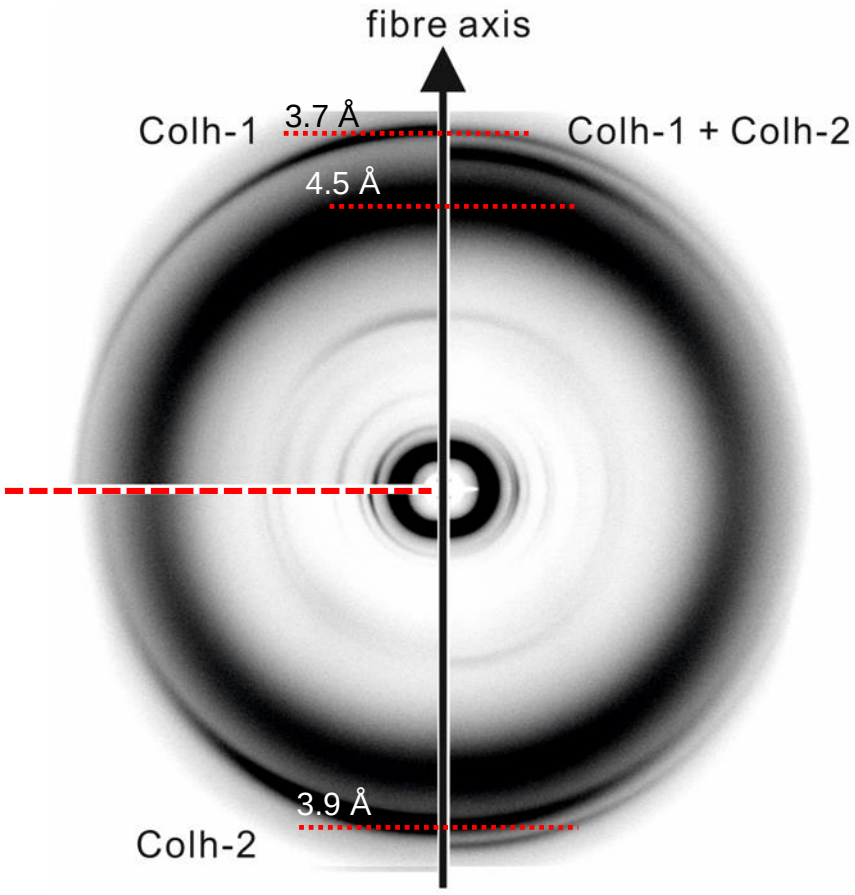

Figure 4.3 Fibre WAXS patterns of 12-12-12Na in the Colh-**1** phase at 70 °C, mixture of phases (Colh-**1** and Colh-**2**) at 80 °C, and the Colh-**2** phase at 90 °C.

In the mixture phase of Colh-**1** and Colh-**2** shown in Figure 4.3, an additional sharp reflection appears and the corresponding spacing is 3.9 Å. On the

equator, a series of new reflections is also observed. They appear at higher *q* than the reflections in the Colh-**1** phase and the ratio of the q^2 values of each reflection is also 1:3:4. When the phase transition is completed, referring to the diffraction pattern in Figure 4.3 (the Colh-**2** phase), only the new sharp reflection is left. The meridional intensity scans of the WAXS patterns show the difference between the meridional reflections between the two phases more clearly - see. Figure 4.4. The diffuse reflection at 4.5 Å appears not to change much upon the Colh-**1** - Colh-**2** transition. However, the sharp reflection shifts closer to the diffuse one in the Colh-**2**. The spacing is changed from 3.7 Å in the Colh-**1** to 3.9 Å in the colh-**2**.

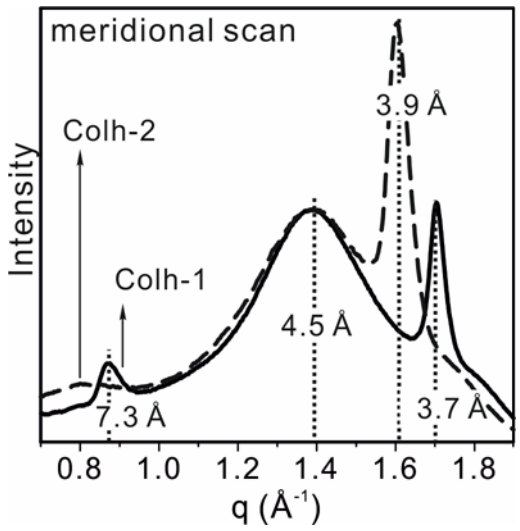

Figure 4.4 Meridional scan of the fibre WAXS results of 12-12-12Na

Since the meridional reflection represents the periodicity along the *c*-axis, the spacing between the aromatic cores of 12-12-12Na can be seen as the *c* parameter. The corresponding spacing of the sharp reflection results from π-π stacking, so that value was taken as the average thickness of a single stratum in the columnar supramolecule. That means that, at the Colh–Colh phase transition, the diameter of the columns is shrinking in a stepwise manner, accompanied by a small increase in the thickness of a single stratum. The change in volume of the unit cell of 12-12-12Na in the Colh phases is shown in

Figure 4.5 as a function of temperature. In the Colh-**1** phase, the volume remains almost independent of temperature. When the phase is changed into Colh-**2**, the volume drops by around 11% and it is continuously declined with temperature. Moreover, the number of molecules in a single stratum can be estimated by Equation 4.1.

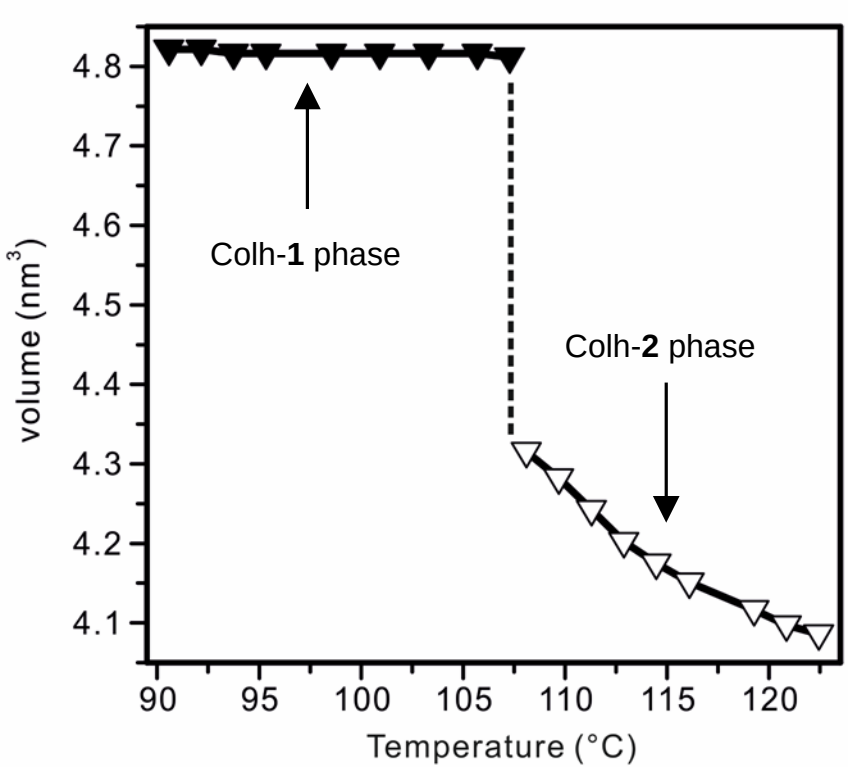

Figure 4.5 The volume of a stratum in the Colh phases of 12-12-12Na at different temperature

However, to calculate the number of 12-12-12Na in a stratum of the columns, the density of 12-12-12Na at different temperature is needed. At room temperature, the density of 12-12-12Na is equal to 1.01 g/ml[1]. We can assume the thermal expansion coefficient of 12-12-12Na to be the same as that of n-$C_{12}H_{26}$ since the majority of the molecular volume is contributed by the alkyl tail –$C_{12}H_{25}$. The molecular volume of 12-12-12Na at different temperatures can thus be computed using the published density vs temperature data for $C_{12}H_{26}$[9]. The number of 12-12-12Na molecules in a stratum is thus estimated and listed

in Table 4.1 and plotted vs temperature in Figure 4.6. In the Colh-**1** phase, there are four 12-12-12Na molecules per stratum. Immediately above the phase transition, however, in the Colh-**2** phase, the average number of 12-12-12Na molecules in a stratum drops to 3.5 and then continues to decline toward 3. However, that number is not actually reached, as the decline is interrupted by a further first-order transition to the micellar cubic P$m\bar{3}n$ phase, where the columns break up into spherical aggregates.

Table 4.1 Calculated number of molecules in a unit cell by cell volume

	Colh-**1** (c = 3.7 Å)			Colh-**2** (c=3.9 Å)		
T (°C)	90	100	105	110	115	120
a_h (Å)	38.8	38.8	38.8	35.6	35.1	34.8
V of cell (Å^3)	482.1	481.6	481.6	428.2	416.7	408.6
$V_{12\text{-}12\text{-}12Na}$ (Å^3)*	122.1	123.4	124.0	124.5	125.2	126.2
no. of molecules in a cell	3.95	3.90	3.88	3.44	3.33	3.24

*[9]Assumed the thermal expansion coefficient of 12-12-12Na is equal to that of $C_{12}H_{26}$.

Similar behaviour is also observed in 12-12-18Na[4]. Figure 4.7 shows the powder SAXS traces obtained by Jitrin Chaiprapa[4]. The lattice parameter, i.e. inter-column distance, of 12-12-18Na in the Colh phases is displayed in Figure 4.8. The lattice parameter in the Colh-**1** phase is almost independent of temperature until approaching the phase transition temperature. There is a jump of the lattice parameter observed when the phase turns into Colh-**2** phase. Furthermore, as with 12-12-12Na, the lattice parameter also declines continuously with temperature in the Colh-**2** phase.

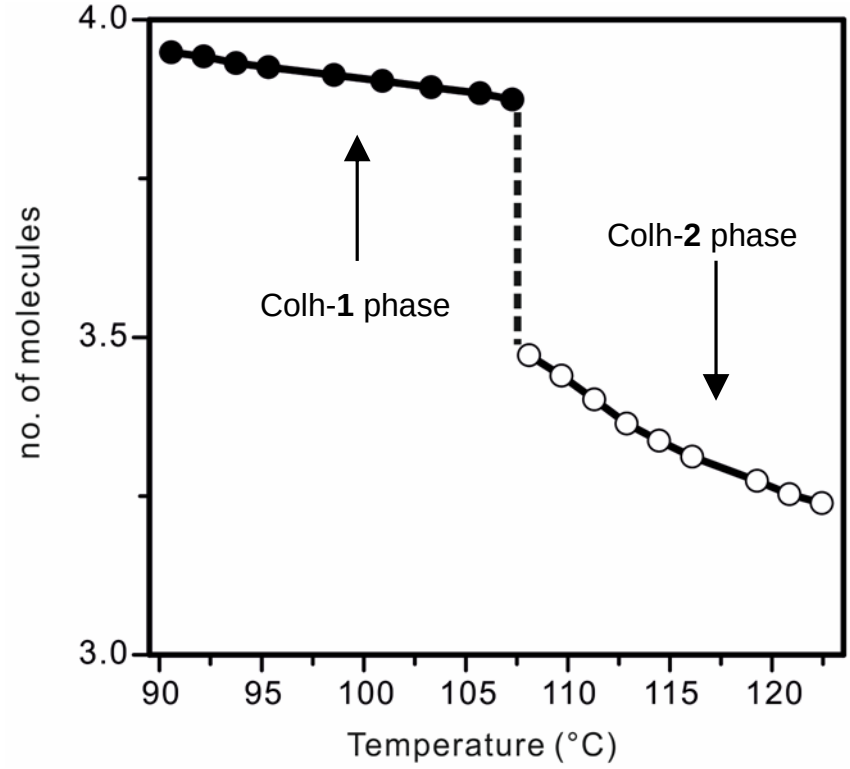

Figure 4.6 The number of 12-12-12Na molecules in a stratum of columns at different temperature

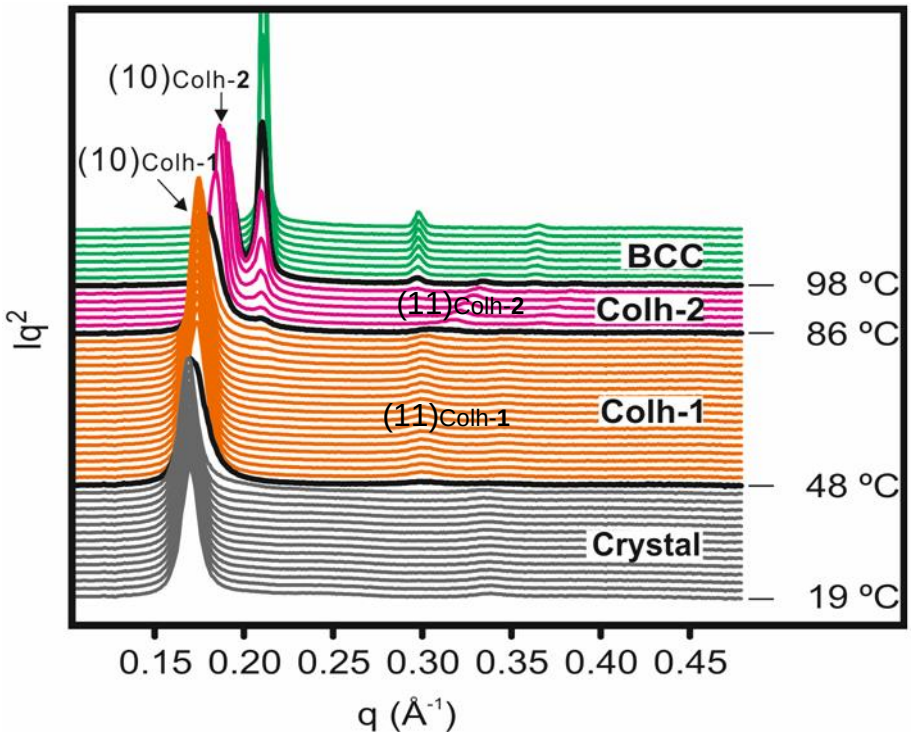

Figure 4.7 SAXS traces of 12-12-18Na in the heating scan by Jitrin Chaiprapa[4]

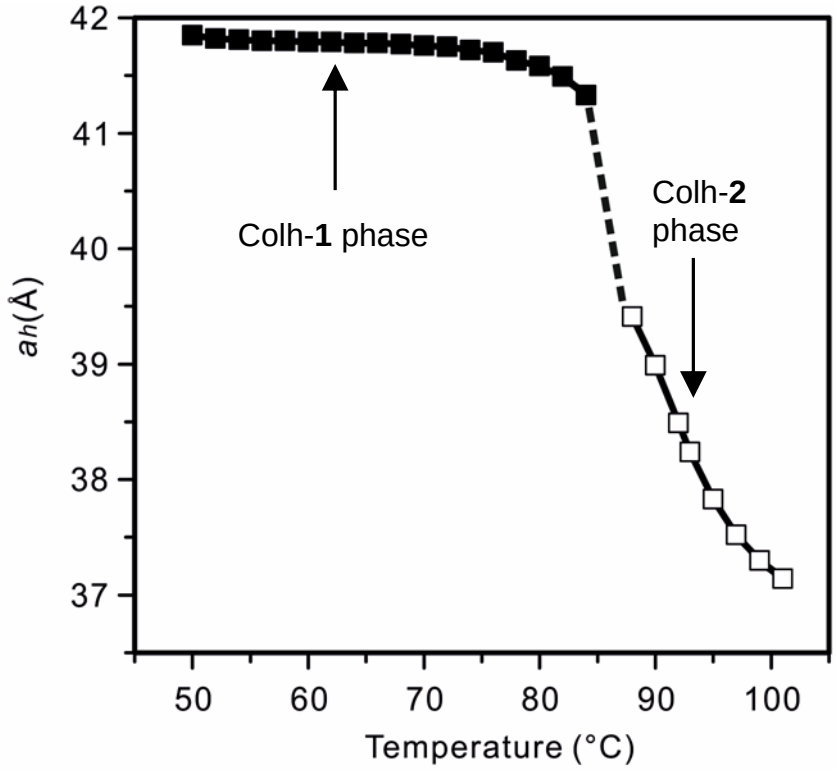

Figure 4.8 The lattice parameter of 12-12-18Na in the Colh phases at different temperature (measured by Jitrin Chaiprapa)[4]

In order to calculate the number of 12-12-18Na in a single stratum of the columns, WAXS experiments were performed on the oriented fibre sample. The fibre WAXS results in Colh-**1** and Colh-**2** phases are shown in Figure 4.9. The meridional scan of WAXS patterns in both phases are displayed in Figure 4.9 as well. The position of the diffuse reflection on the meridian is the same in both Colh-**1** and Colh-**2** phases. However, again, the sharp reflection on the meridian is moving inner in the Colh-**2** phase. That means the spacing of the π-π stacking resulted from the aromatic core of the minidendrons is increased. The spacing is enlarged from 3.7 Å to 3.9 Å. This consequence is the same as the Colh–Colh phase transition in 12-12-12Na. Assume the density of 12-12-18Na is 1.00 g/cm^3 at room temperature and the thermal expansion coefficient of 12-12-18Na is the same as n-$C_{12}H_{26}$. The number of 12-12-18Na molecules in a stratum of the columns thus can be estimated.

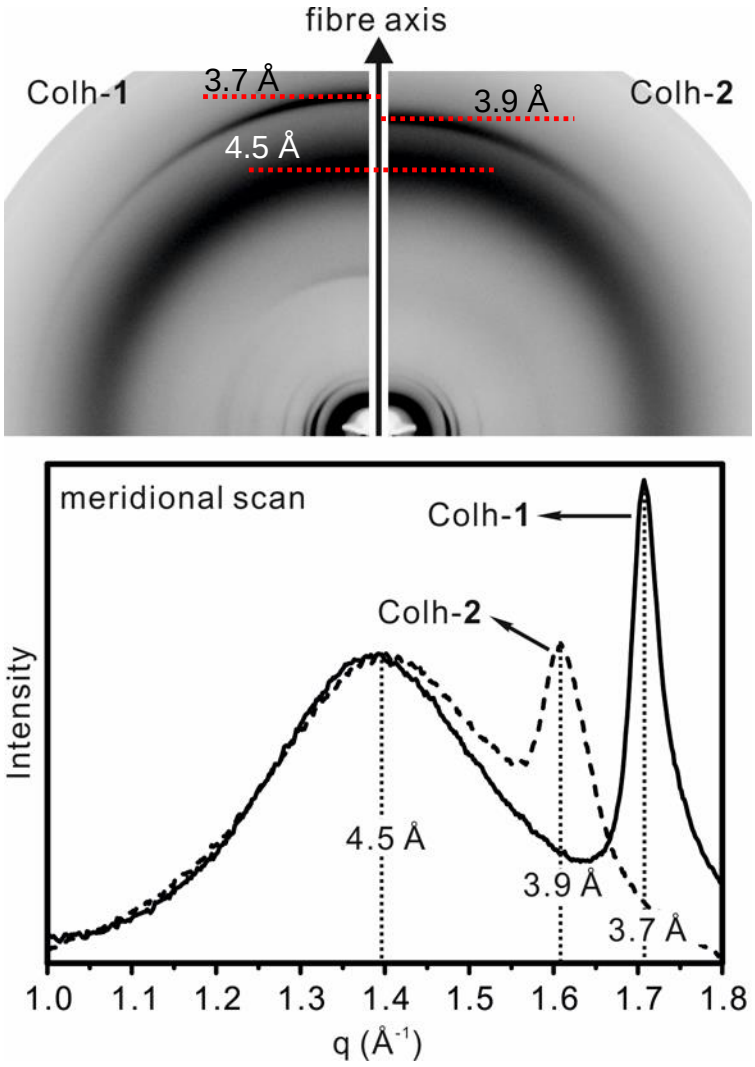

Figure 4.9 The fibre WAXS diffraction patterns of 12-12-18Na in the Colh-**1** and Colh-**2** phase. The bottom is the meridional scan of the WAXS patterns

Figure 4.10 shows the number of 12-12-18Na in a stratum in the Colh phase at different temperature. Similar to 12-12-12Na, there are four minidendrons in a Colh-1 stratum. The average number of 12-12-18Na in a unit cell still drops and approaches three in the Colh-**2** phase. Again, the Colh-Colh phase transition is related to the change of the number of molecules in a stratum. An excess molecule is expelled from the original disc when the phase changes from Colh-**1** to Colh-**2** phase. Nevertheless, the jump between the number of molecules in the Colh-1 and Colh-2 phase is smaller than that in 12-12-12Na. As we mentioned, Colh-Colh phase transition is observed in sodium and potassium

salts. But, when the length of the tails increases, such as hexadecyl and octadecyl tails, this phenomenon becomes obscure. The decrease of lattice parameter becomes continuous and the jump disappears. Thus, changing only one chain from dodecyl to octadecyl may make this first order transition go half-way and the jump smaller.

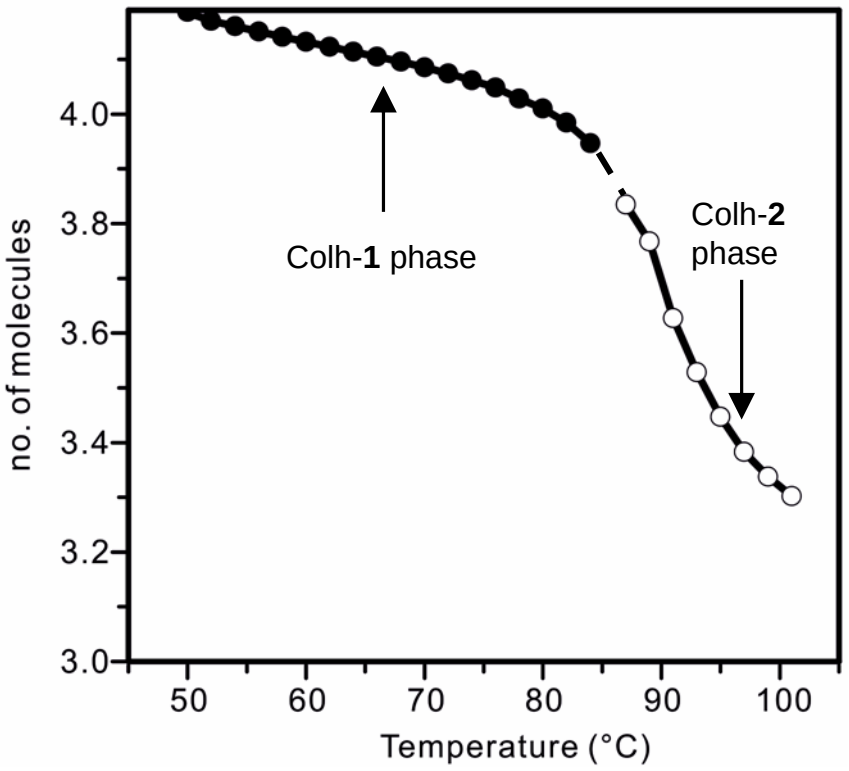

Figure 4.10 The number of 12-12-18Na molecules in a stratum of the columns in the Colh-**1** and Colh-**2** phase at different temperature

From the fibre WAXS patterns, we know the shape of the unit cell is changed when the phase transition occurs. The cross-section area is reduced but the height becomes increased after the phase transition while the columns are still arranged into the same symmetry. By the estimation of the number of molecules in a stratum, there are four molecules per stratum in the Colh-**1** columns but a stratum in the Colh-**2** columns has only three molecules. Due to one more molecules in a stratum, the cross-section area of the columns in the

Colh-**1** phase thus is larger than the columns with less molecules in the Colh-**2**.

However, it cannot explain why the thickness of a stratum, or spacing between two adjacent layers, is changed as well during the Colh-Colh phase transition. In the Colh-**1** the spacing between two adjacent layers is 3.7 Å and in the Colh-**2** it is expanded to 3.9 Å. The diameter of a stratum in the Colh-**1** is larger and the adjacent stratums are packing closer. That implies the core of the minidendrons in the Colh-**1** is closer to being perpendicular to the column axis, while in Colh-**2** they are more tilted. Moreover, from Figure 4.4, there is another inner reflection observed in the meridional scan. This sharp reflection is at the positon corresponding to a spacing of 7.2 Å. Moreover, it lies on the layer line *l* = 1 and the outer lies on layer line *l* = 2. That implies the molecules pack into 2_1 helix in the Colh-**1** columns

In order to find out how the molecules assemble in the columnar supramolecules, the azimuthal scan of the fibre WAXS patterns would be helpful. Figure 4.11 displays the azimuthal scan of the WAXS patterns of 12-12-12Na in the Colh-**1** phase and Colh-**2** phase respectively. The fibre is tilted to obtain the intensity maximum of meridional reflections. In Figure 4.11 (a), there are two narrow peaks and one broad peak on the meridian in the Colh-**1** phase. The *q* value of the outer narrow reflection arising from π-π stacking, q_{outer}, is 1.70 $Å^{-1}$. The *q* value of the inner narrow reflection, q_{inner} is 0.87 $Å^{-1}$. The q_{inner}^2 value is equal to $q_{(10)}^2 + (q_{outer}/2)^2$. The outer narrow reflection thus index as (002) and the inner one index as (101). Based on our calculation results, each stratum consists of four molecules. So, every eight molecules is repeatable by the following eight molecules. Moreover, the molecules in the Colh-**1** phase pack into helical structure in the columnar supramolecules. The 8_4 screw axis. i.e. the quadruple 2_1 helix, arrangement of the molecules round the axis of each column.

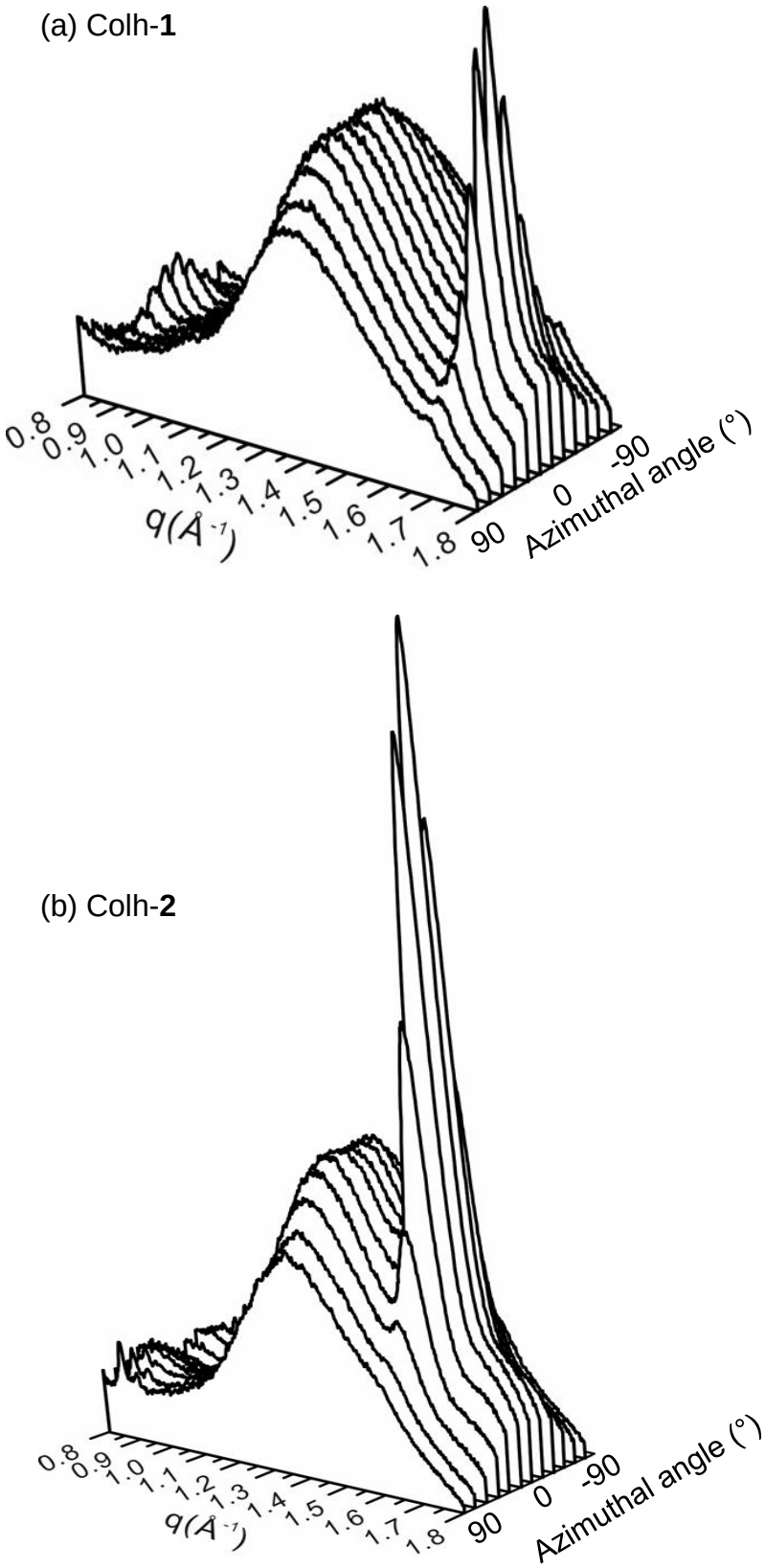

Figure 4.11 Series of radial traces of the WAXS pattern of oriented fibre of 12-12-12Na in the (a) Colh-**1** and (b) Colh-**2** phases. The curves are separated by an azimuthal increment of 15˚.

In the Colh-**2** phase, the azimuthal scan of the WAXS pattern (displayed in Figure 4.11 (b)) shows only one sharp and one broad peak on the meridian. The narrow reflection is located at q = 1.6 $Å^{-1}$ and lies on layer line *l* = 2. On layer line *l* = 1, instead of another meridional narrow peak, a pair of split humps is observed. That means the molecules in the Colh-**2** columns still pack into helical structure in the columns. Since only three molecules exist in a stratum, in every period the number of molecules is reduced to six. The molecules are thus arranged around a 6_3 screw axis coinciding with the columnar axis. Furthermore, the larger split of the reflections at q = 0.81 $Å^{-1}$ indicate that the helices are narrower in the Colh-**2** phase. Similar results are observed in the azimuthal scan of 12-12-18Na fibre WAXS patterns shown in Figure 4.12. One molecule is expelled from each stratum and the diameter of the columns decreases in the Colh-**2** phase.

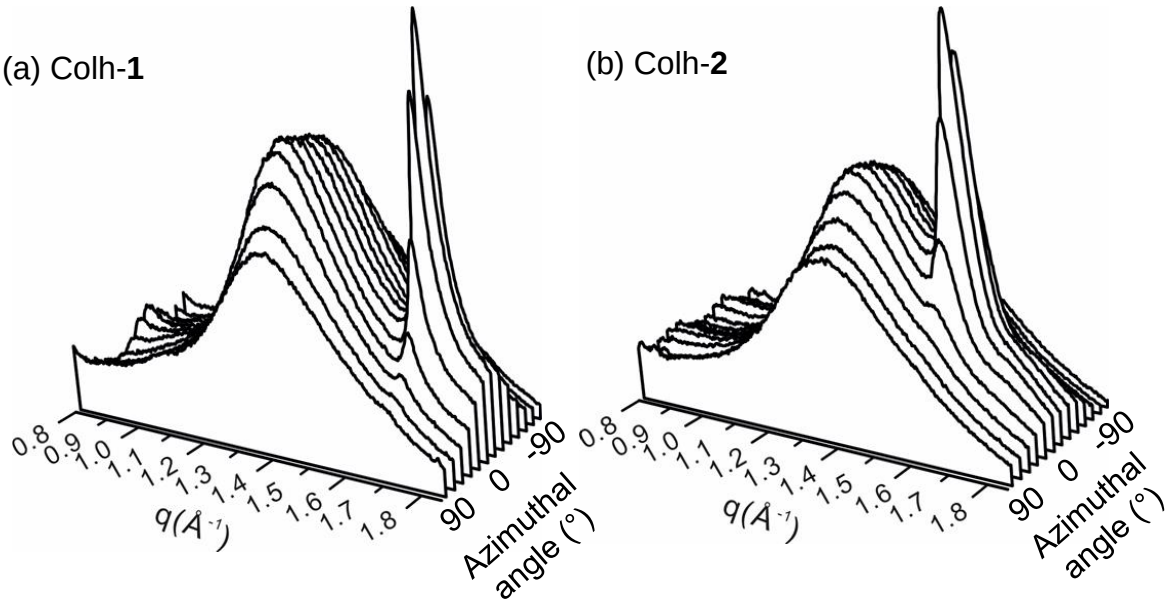

Figure 4.12 Series of radial traces of the WAXS pattern of oriented fibre of 12-12-18Na in the (a) Colh-**1** and (b) Colh-**2** phases. The curves are separated by an azimuthal increment of 15˚.

As we know, the ratio of *gauche*/*trans* conformation of the alkyl chains increases at higher temperature according to Boltzmann distribution. Thus, we believe that the excess molecules expelled from the stratum during the Colh-

Colh phase transition is related to the conformational disorder of the alkyl chains. When the alkyl bonds change from *trans* to *gauche* conformation, they expand laterally. In order to avoid the overlap of the molecules, the minidendrons may tilt slightly. That leads to an increase in spacing between the two adjacent layers.

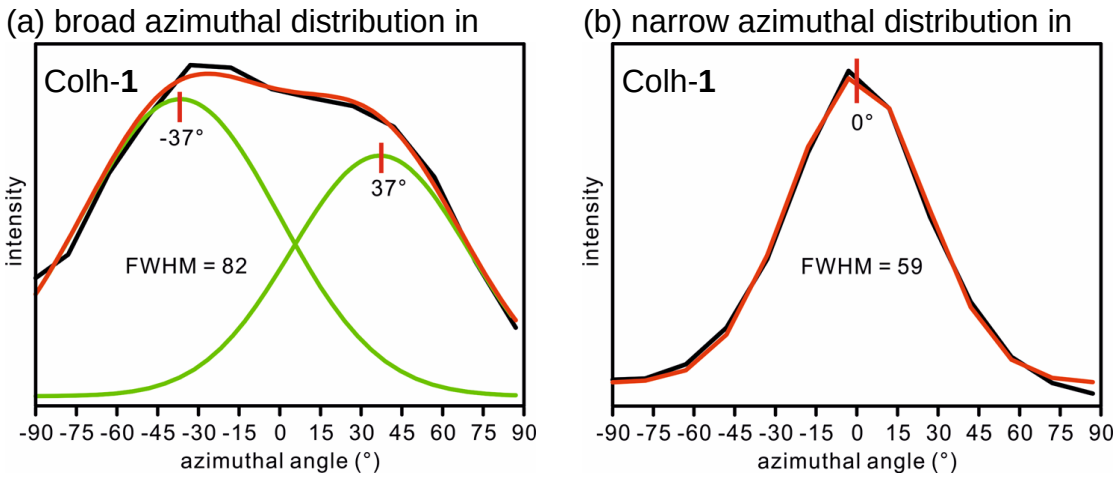

Figure 4.13. The azimuthal scan of (a) broad and (b) narrow azimuthal distribution in 12-12-12Na Colh-**1** phase. Green is the fitting curve of individual peak and red is the summation.

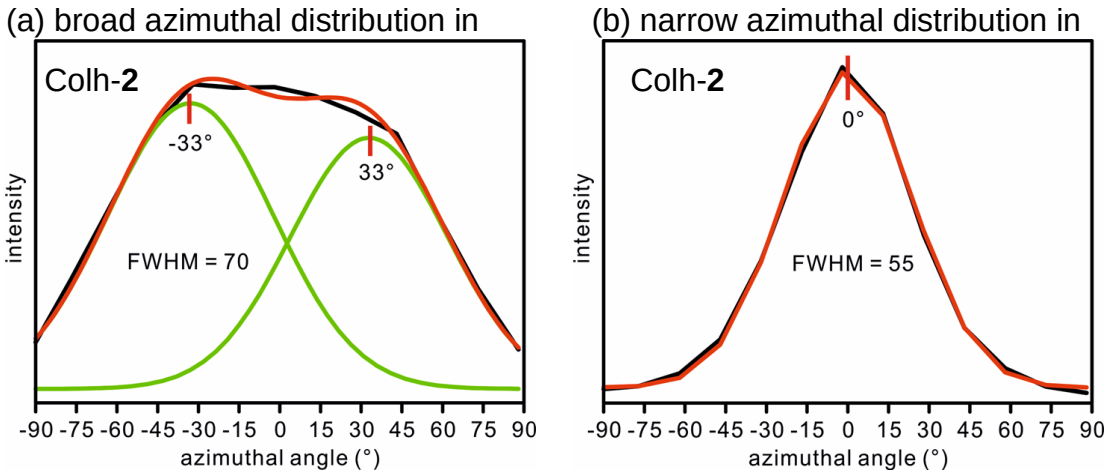

Figure 4.14. The azimuthal scan of (a) broad (b) narrow azimuthal distribution in 12-12-12Na Colh-**2** phase. Green is the fitting curve of individual peak and red is the summation.

Azimuthal scans of the WAXS patterns reveal more details of packing of molecules. Figure 4.13 shows the azimuthal scan of the broad and outer sharp reflections in the Colh-1 phase. In Figure 4.13 (a), the diffuse reflection is split. It inclines azimuthally at 37°. That means the alkyl tails of the minidendrons are tilted to the columnar axis[10]. The tilting angle of the alkyl chains can be correlated by Polanyi equation[11]:

$$\cos\rho = \cos\theta\cos\beta \quad -----(4.2),$$

where, where ρ is the angle between the fibre axis and the normal to the set of planes, θ is Bragg angle of the plane, and β is the inclining angle between the meridian and diffraction pattern. The tilting angle of the aliphatic tails is about 39° in the Colh-**1** phase. Meanwhile, the sharp reflection is non-split. That may imply the aromatic rings are roughly perpendicular to cylinder axis. In the Colh-**2** phase, shown in Figure 4.14, the diffuse reflection is still split but the inclining angle to meridian is reduced to 33°. Through the correlation by Polanyi equation, the tilting angle of the alkyl tails is about 34° and that means they are spreading more in-plane with the aromatic core in the Colh-**2** phase.. The sharp reflection is non-split and the packing of the benzene rings should still be perpendicular to the column axis.

(a)

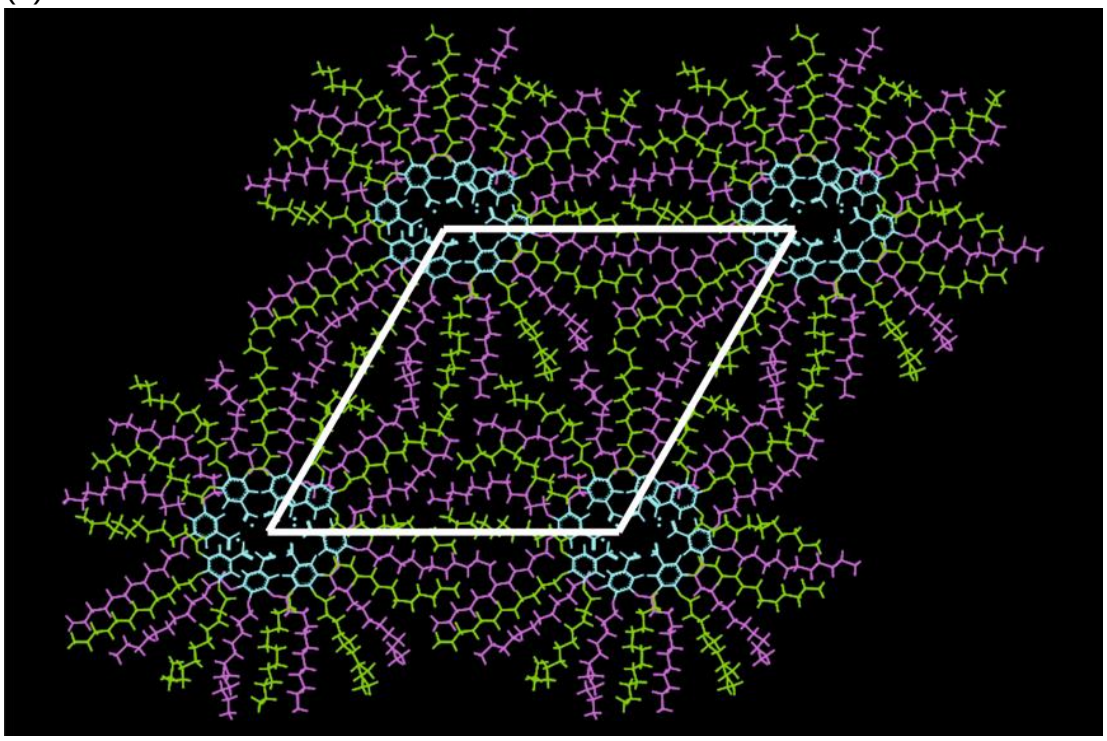

(b)

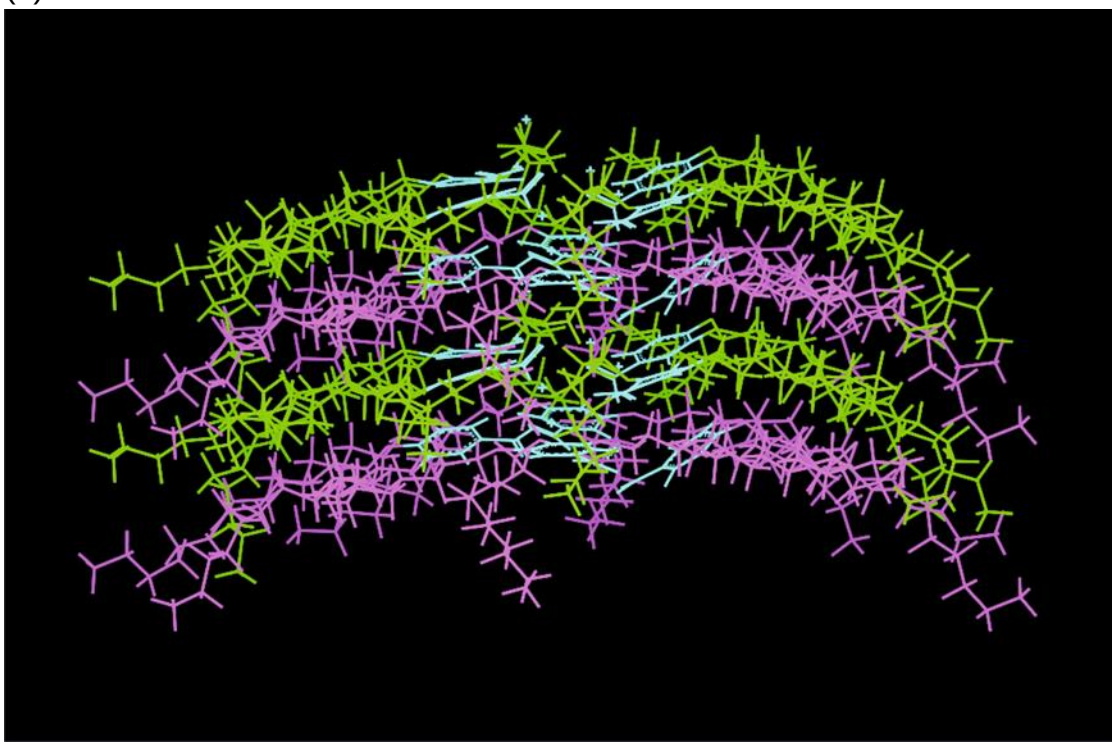

Figure 4.15. The model of 12-12-12Na in the Colh-**1** phase: (a) top view and (b) side view. The green molecules lie on the upper layer and the pink ones on the bottom layer; blue: benzoate group.

Based on this information, the molecular model of 12-12-12Na in the Colh-**1** and Colh-**2** phases are built. Figure 4.15 shows the model of 12-12-12Na in the Colh-**1** phase using Materials Studio. Two strata are put in the model. The *c* parameter is doubled. Most alkyl tails of the minidendrons are in *all-trans* conformation. The tilting angle of alkyl tails is 39°. The built model was minimized by the minimizer in ForcitePlus module. Then, five annealing molecular dynamics simulation cycles were performed between 300 and 700 °C by ForcitePlus module. In Figure 4.15 the alkyl tails are tilted relative to their aromatic cores. The aliphatic chains are also tilted to the columnar normal. The benzene rings are also slightly tilted to the cylinder axis. Furthermore, the adjacent layers are rotated by 45°. The molecules arrange into helical structure in the supramolecular columns and the columns thus exhibit 8_4 screw symmetry in the Colh-**1** phase.

The molecular model of 12-12-12Na in the Colh-**2** phase built by Materials Studio is displayed in Figure 4.16. The span angle of the minidendron is wider than the molecule in the Colh-**1** phase. The alkyl tails contain more *gauche*-bonds than in the Colh-1 phase. Two layers and the doubled *c* parameter are used for the model construction. In this model, each layer has only three molecules. The alkyl tails tilts 34° to the cylinder axis. The built model was minimized by the minimizer and experienced five annealing cycles between 300 to 700 °C by ForcitePlus module.

From the model in Figure 4.16, the aliphatic chains are expanded wider and distributed more randomly in the stratum. They tilt less with respect to the plane formed by the benzene rings. The aromatic cores of 12-12-12Na are more tilted to the columnar axis. That leads the alkyl tails are tilted to the columnar axis as well. Furthermore, the adjacent layers are rotated by 60°. Thus, the molecules display tree-like helical structure in the supramolecular columns and the columns thus exhibit 6_3 screw symmetry in the Colh-**2** phase.

(a)

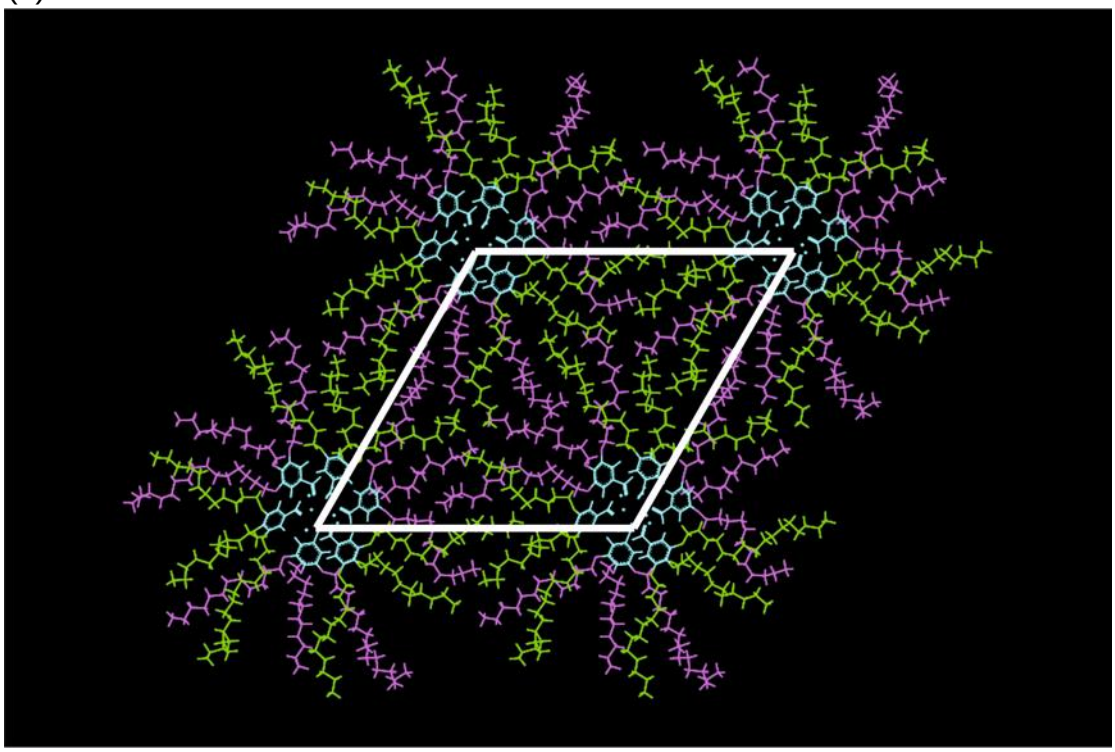

(b)

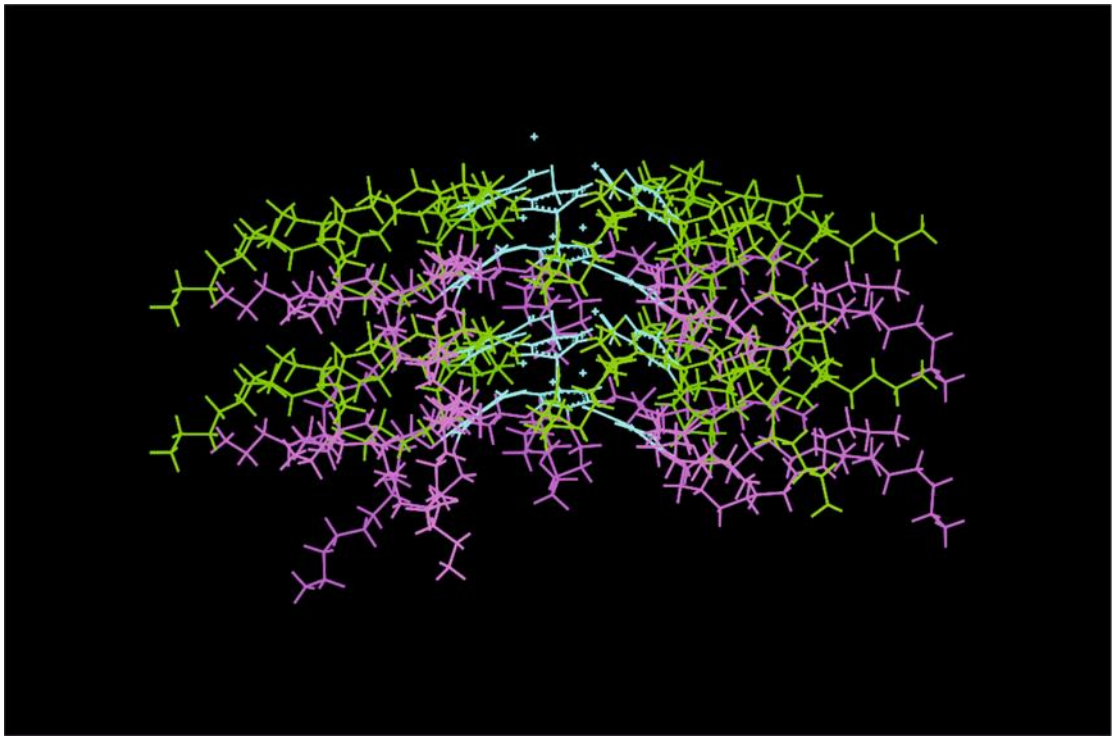

Figure 4.16 The model of 12-12-12Na in the Colh-**2** phase: (a) top view and (b) side view. The green molecules lay on upper layer and the pink ones are on the bottom layer; blue: benzoate group

4.4 Conclusion

The Colh-Colh phase transition is interpreted in this chapter. This interesting behaviour is found in sodium minidendrons, 12-12-12Na[3] and 12-12-18Na[4]. During the phase transition, the symmetry of the arrangement of the columnar supramolecules is the same. However, the lattice parameter is suddenly changed between these two phases. Furthermore, the lattice parameter is independent of temperature in the low temperature phase but continuously declines with temperature in the high temperature phase.

From WAXS experiments performed on the oriented fibres, during the phase transition, not only *a* parameter is changed but *c* parameter is differed as well. The thickness of a stratum in the Colh-**2** phase is expanded compared with the thickness in the Colh-**1** phase. The number of molecules in a unit cell can be computed by the assumed molecular density. It is estimated that there are four molecules in a Colh-**1** stratum while the number drops to three in the Colh-**2** phase.

Referring to the built model, in the Colh-**1** phase, the minidendrons assemble into an 8_4 helix. The aromatic cores of the minidendrons pack more planar and more perpendicular to the columnar axis. The aliphatic chain is more *trans* and straight. They are tilted downward and the tilting angle is 39°. That makes the packing of two adjacent layers denser. In the Colh-**2** phase, the minidendrons form a 6_3 helical structure. The aromatic cores are slightly tilted and thus the spacing of a stratum is expanded. The conformation of the alkyl tails display more *gauche* bonds and the coronas spread more widely. The tilting angle of the aliphatic chains reduces to 34° and disperse more randomly. Based on the models, the sketch of the molecules in the Colh-**1** and Colh-**2** are drawn and shown in Figure 4.19.

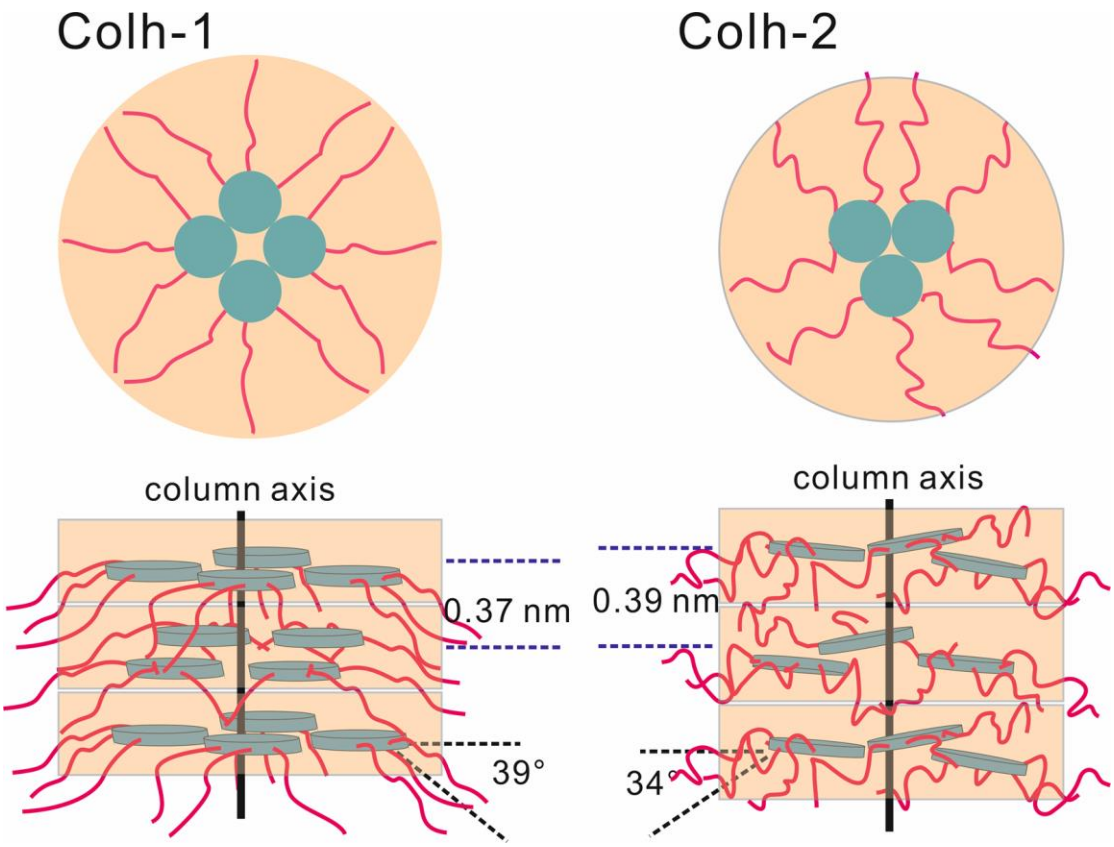

Figure 4.17 The sketch of the molecules in the Colh-**1** and Colh-**2** phase

Reference:

1. Ungar, G.; Percec, V.; Holerca, M. N.; Johansson, G.; Heck, J. A., Heat-shrinking spherical and columnar supramolecular dendrimers: Their interconversion and dependence of their shape on molecular taper angle. *Chem. Eur. J.* **2000,** 6, (7), 1258-1266.

2. Percec, V.; Holerca, M. N.; Uchida, S.; Cho, W. D.; Ungar, G.; Lee, Y. S.; Yeardley, D. J. P., Exploring and expanding the three-dimensional structural diversity of supramolecular dendrimers with the aid of libraries of alkali metals of their AB(3) minidendritic carboxylates. *Chem. Eur. J.* **2002,** 8, (5), 1106-1117.

3. Liu, Y. S. Two- and three-dimensional liquid crystalline structures in self-assembled supramolecular dendrimers. University of Sheffield, 2004.

4. Chaiprapa, J. New supramolecular liquid crystal structures in wedge-shaped molecules. Univ. of Sheffield, 2012.

5. Shcherbina, M. A.; Bakirov, A. V.; Yakunin, A. N.; Beginn, U.; Yan, L. L.; Moeller, M.; Chvalun, S. N., The effect of the shape of the mesogenic group on the structure and phase behavior of 2,3,4-tris(dodecyloxy)benzenesulfonates with alkaline cations. *Soft Matter* **2014,** 10, (11), 1746-1757.

6. Percec, V.; Imam, M. R.; Peterca, M.; Wilson, D. A.; Graf, R.; Spiess, H. W.; Balagurusamy, V. S. K.; Heiney, P. A., Self-assembly of dendronized triphenylenes into helical pyramidal columns and chiral spheres. *J. Am. Chem. Soc.* **2009,** 131, (22), 7662-7677.

7. Peterca, M.; Percec, V.; Imam, M. R.; Leowanawat, P.; Morimitsu, K.; Heiney, P. A., Molecular structure of helical supramolecular dendrimers. *J. Am. Chem. Soc.* **2008,** 130, (44), 14840–14852.

8. Shcherbina, M. A.; Zeng, X. B.; Tadjiev, T.; Ungar, G.; Eichhorn, S. H.; Phillips, K. E. S.; Katz, T. J., Hollow six-Stranded helical columns of a helicene. *Angew. Chem. Int. Ed.* **2009,** 48, (42), 7837-7840.

9. Orwoll, R. A.; Flory, P. J., Equation-of-state parameters for normal alkanes. Correlation with chain length *J. Am. Chem. Soc.* **1967,** 89, (26), 6814-6822.

10. Chvalun, S. N.; Blackwell, J.; Cho, J. D.; Kwon, Y. K.; Percec, V.; Heck, J. A., X-ray analysis of the internal rearrangement of the self-assembling columnar structure formed by a highly tapered molecule. *Polymer* **1998,** 39, (19), 4515-4522.

11. Klug, H. P.; Alexander, L. E., *X-ray diffraction procedures : for polycrystalline and amorphous materials*. Wiley: New York, 1954.

Chapter 5 Close Packed Thermotropic Liquid Crystal Structure

5.1 Introduction

Close packed arrays are is the densest packing of hard spheres with long range ordered. They are found in many crystals formed by atoms or ions. In liquid crystals, the close packed structure was also found in some lyotropic liquid crystalline systems. However, although thermotropic liquid crystals can form spherical aggregates that can self-arrange into 3-D cubic phases, until now, no close packed structure has been observed in these materials[1-5].

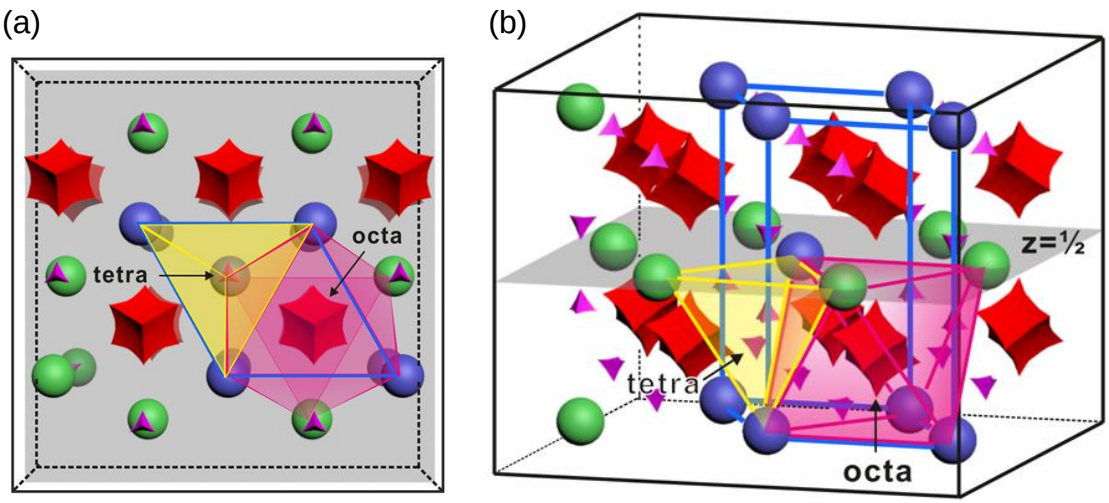

Figure 5.1. HCP structure and the octahedral and tetrahedral interstices in it; (a) top view and (b) side view.

For other 3-D phases, such as BCC or P$m\bar{3}n$, there are only tetrahedral interstices. However, in the close packed structure, octahedral interstices exist as well[1, 6]. Figure 5.1 shows the interstices in hexagonal close packed (HCP) phase. According to our experimental results in Table 5.3, e.g. when the lattice parameter is 40 Å, the distance from the apex to the centre of tetrahedron is 24.5 Å. The distance between apex to centre of octahedron increases to 28 Å. Suppose the cation is in plane with benzoate group and all alkyl tails are

stretched. The distance from ion to end of the stretched alkyl tails of 12-12-12Rb is 24 Å. The distance from the apex to the centre of octahedron is much larger than the distance between the apex and the centre of tetrahedron and the tails is hard to reach. Moreover, the size of the octahedral interstices is much larger than the tetrahedral ones. Thus, in the thermotropic liquid crystals, inaccessibility of the octahedral interstices leads to the absence of close packed structures.

Alkali metal 3,4,5-tri(alkyloxy)benzoate salts were shown to form micelle-like spherical aggregates ("supramolecules") that self-organise into 3-D mesophases with tetrahedral interstices. In order to obtain the close packed structure, no matter HCP or FCC (face-centred cubic), the octahedral interstices must be eliminated. Thus, small amount of n-alkane was added into the minidendrons. The added alkanes are helpful to fill the vacancies and make the close packed structure stabilised. A pure HCP phase in mixtures of sodium 3,4,5-tri(dodecyloxy)benzoate salt (12-12-12Na) and nonadecane is observed[7]. Pure HCP phase was also found in the minidendron-alkane blends of rubidium 3,4,5-tri(dodecyloxy)benzoate salt (12-12-12Rb)[7]. That means the close packed structure is possible with the aid of the additional alkyl chains[7].

However, which role the added n-alkane plays in the close packed structure is still unclear. In this chapter, we attempt to explain how the HCP is stabilised in the minidendrons. Deuterated n-alkane is used to replace the non-deuterated one in the blends. In the neutron scattering experiment, deuterated alkane can be distinguished from hydrogen alkane because the coherent neutron scattering length of $-CH_2-$ is -0.83 fm and $-CD_2-$ is 19.99 fm[8]. Thus, the deuterated alkane can be discriminated. From the reconstructed density maps, the details of the close packed structure in the minidendrons could be interpreted.

5.2 Experiments

Materials

In this chapter, two different kinds of minidendrons, sodium 3,4,5-tri(dodecyloxy)benzoate salt (12-12-12Na) and rubidium 3,4,5-tri(dodecyloxy)benzoate salt (12-12-12Rb), are used. Both of them have three long alkyl tails of the same length. Scheme 1 shows the chemical structure of these monodendrons. The synthesis of 12-12-12Na and 12-12-12Rb samples were described in Chapter 3.1.1.

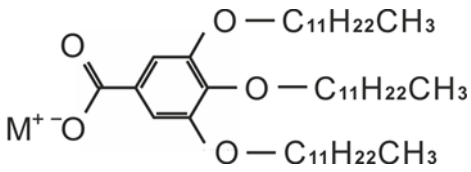

Scheme 1 Chemical structure of 12-12-12Na (M=Na) and 12-12-12Rb (M=Rb)

The compositions of 12-12-12Na-d-alkane and 12-12-12Rb-d-alkane blends are listed in Table 5.1. The preparation of the minidendron-alkane blends follows the procedure described in Chapter 3.1.2.

Table 5.1 The composition of 12-12-12Na + $C_{19}D_{40}$ and 12-12-12Rb + $C_{19}D_{40}$ blends in weight percent

	12-12-12Na+ 12.5wt% $C_{19}D_{40}$	12-12-12Na+ 15wt% $C_{19}D_{40}$	12-12-12Na+ 17.5wt% $C_{19}D_{40}$
$C_{19}D_{40}$ (%)	12.5	15	17.5
12-12-12Na (%)	87.5	85	82.5
	12-12-12Rb+ 12.5wt% $C_{19}D_{40}$	12-12-12Rb+ 15wt% $C_{19}D_{40}$	12-12-12Rb+ 17.5wt% $C_{19}D_{40}$
$C_{19}D_{40}$ (%)	12.5	15	17.5
12-12-12Rb (%)	87.5	85	82.5

The powder samples were put in capillaries for SAXS. The procedure of specimen preparation is described in Chapter 3.2.2. The preparation of the powder samples for neutron scattering experiments was mentioned in Chapter 3.3.2.

Methods

The details of powder SAXS experiments were described in Chapter 3.2.2. The procedure of SAXS data reduction is described in Chapter 3.4.1.

The details of SANS experiments were mentioned in Chapter 3.3.2. The procedure of neutron data reduction was described in Chapter 3.3.3.

The reconstruction of density maps is explained in Chapter 3.4.2.

5.3 Results and Discussion

In our previous work, the powder SAXS experiments on series 12-12-12Na + n-$C_{19}H_{40}$ and 12-12-12Rb + n-$C_{19}H_{40}$ blends are performed by Jitrin Chaiprapa[7]. In the mixture of 12-12-12Na + 15wt% n-$C_{19}H_{40}$ and 12-12-12Rb + 15wt% n-$C_{19}H_{40}$, pure HCP phase is observed. Figure 5.2 shows the SAXS curves for 12-12-12Na + 15wt% n-$C_{19}H_{40}$ and 12-12-12Rb + 15wt% n-$C_{19}H_{40}$ blends respectively in the heating scan.

In SAXS patterns of 12-12-12Na + 15wt% $C_{19}H_{40}$ shown in Figure 5.2 (a), HCP phase follows the 2-D Colh mesogenic phase in the heating scan. BCC phase is observed at the end of the temperature range of HCP phase. In 12-12-12Rb + 15wt% $C_{19}H_{40}$, HCP phase is the first and only liquid crystal phase observed in the heating scan. The blend becomes isotropic liquid after the HCP phase. Since with the aid of the added alkane, the close packed structure is obtained, the added alkane must play an important role in stabilising the phase. In order to understand how it helps, neutron scattering experiment is performed. Because deuterium can be distinguished from hydrogen in neutron scattering, the deuterated alkane (d-alkane) is used to replace the normal one. Thus, we can tell apart the deuterated alkane and the alkyl tails of the minidendrons.

In this work, deuterated nonadecane, $C_{19}D_{40}$, is used to replace the non-deuterated one. Two kinds of minidendrons, 12-12-12Na and 12-12-12Rb are used in preparing minidendron-d-alkane blends. The concentrations of $C_{19}D_{40}$ are listed in Table 5.1. The final products are examined by SAXS experiments to see the mesophase at different temperature. Figure 5.3 shows SAXS results for 12-12-12-Na + 12.5wt%, 15wt%, and 17.5wt% $C_{19}D_{40}$ respectively. The HCP phase is observed in all of the 12-12-12Na + $C_{19}D_{40}$ mixtures. In the blend of 12-12-12Na + 12.5wt% $C_{19}D_{40}$ (Figure 5.3 (a)), the Colh phase is shown firstly in the heating scan. Then, HCP phase is obtained following the Colh phase at higher temperatures. The blend displays BCC phase in the end of the temperature range of HCP phase. The same phase sequence is also observed in the blend of 12-12-12Na +15wt% $C_{19}D_{40}$ (Figure 5.3 (b)) and 12-12-12Na + 17.5wt% $C_{19}D_{40}$ (Figure 5.3 (c)) during the heating scan. The Colh phase is observed first, followed by HCP phase. The BCC phase is then obtained at

higher temperatures. The measured calculated spacing of 12-12-12Na + $C_{19}D_{40}$ in the different phases are listed in Table 5.2.

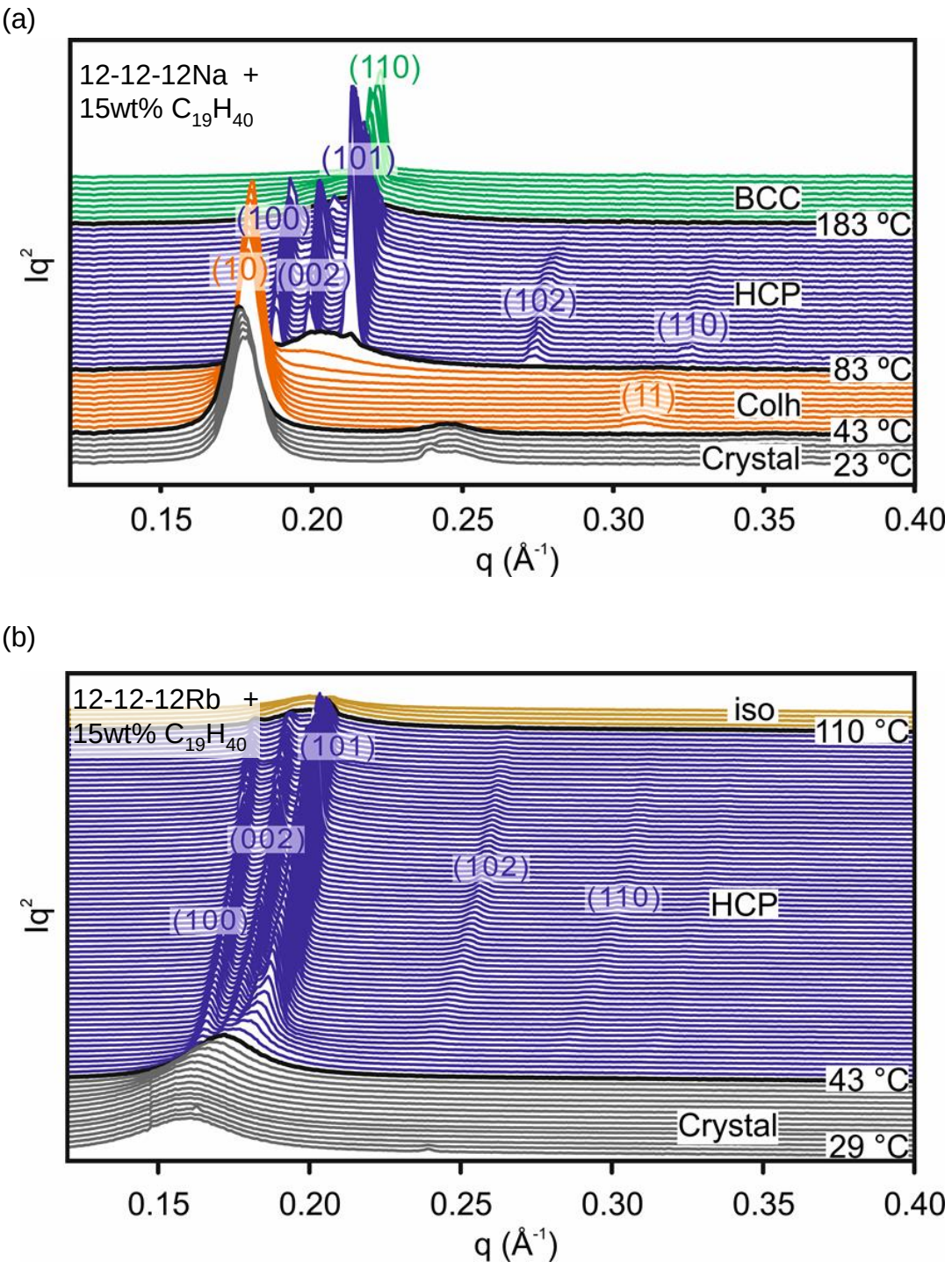

Figure 5.2. SAXS traces of (a) 12-12-12Na +15wt% $C_{19}H_{40}$ and (b) 12-12-12Rb +15wt% $C_{19}H_{40}$ in the first heating scan by Jitrin Chaiprapa[7].

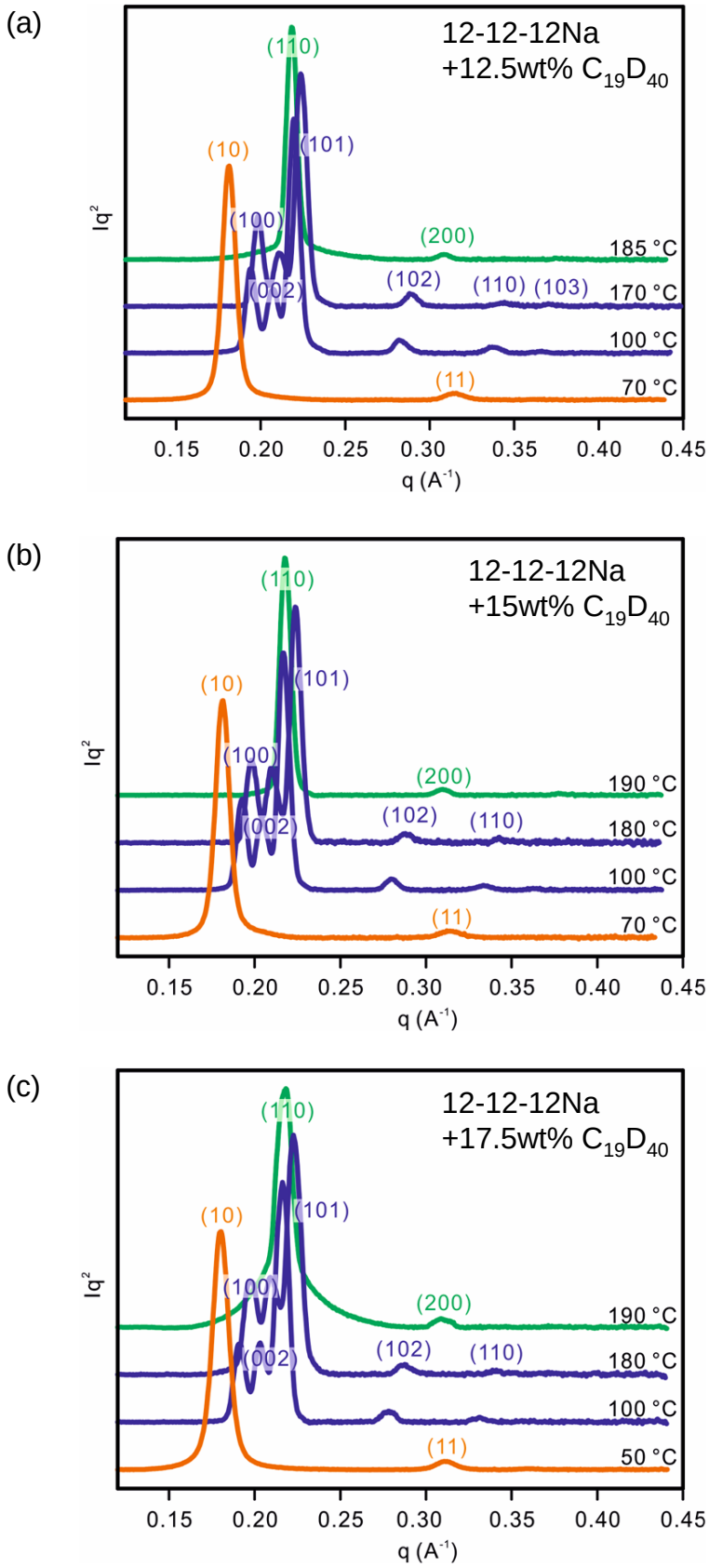

Figure 5.3. The SAXS curves of 12-12-12Na + (a) 12.5wt% $C_{19}D_{40}$, (b) 15wt% $C_{19}D_{40}$, and (c) 17.5wt% $C_{19}D_{40}$ in the heating scan.

Table 5.2 Measured and calculated spacing of 12-12-12Na + $C_{19}D_{40}$ in different phases

blends	T (°C)	phase	(hkl)	d_{exp} (Å)	d_{cal} (Å)	lattice parameter (Å)	no. of molecules in cell
12-12-12Na + 12.5wt% $C_{19}D_{40}$	100	HCP	(100)	32.3	32.3	a=37.3 c=60.8	54 12-12-12Na 18 $C_{19}D_{40}$
			(002)	30.4	30.4		
			(101)	28.6	28.5		
			(102)	22.2	22.2		
			(110)	18.6	18.6		
			(103)	17.2	17.2		
	185	BCC	(110)	28.8	28.8	a=40.7	50 12-12-12Na 16 $C_{19}D_{40}$
			(002)	20.4	20.4		
blends	T (°C)	phase	(hkl)	d_{exp} (Å)	d_{cal} (Å)	lattice parameter (Å)	no. of molecules in cell
12-12-12Na + 17.5wt% $C_{19}D_{40}$	110	HCP	(100)	32.5	32.5	a=37.5 c=61.2	52 12-12-12Na 25 $C_{19}D_{40}$
			(002)	30.6	30.6		
			(101)	28.8	28.7		
			(102)	22.3	22.3		
			(110)	18.8	18.8		
			(103)	17.3	17.3		
	190	BCC	(110)	28.9	28.9	a=40.9	48 12-12-12Na 23 $C_{19}D_{40}$
			(200)	20.3	20.4		

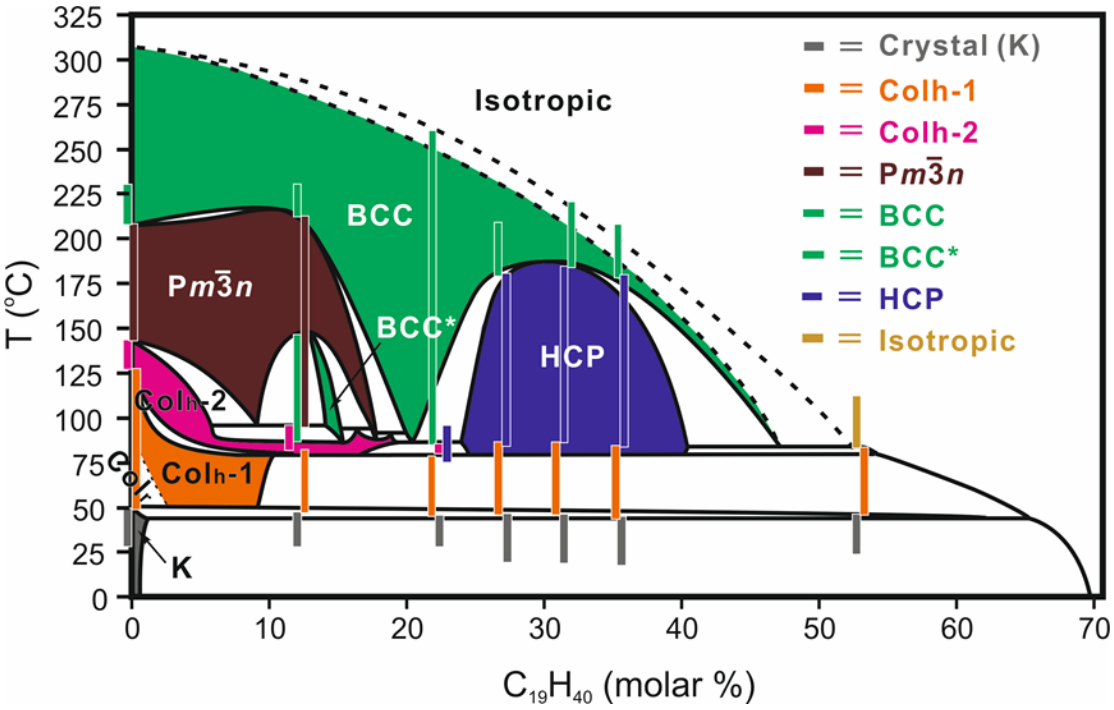

Figure 5.4. Binary phase diagram of 12-12-12Na and $C_{19}H_{40}$

Besides, the binary phase diagram of the minidendron-alkane blends are constructed based on experimental results. Figure 5.4 displays the binary phase diagram of 12-12-12Na and nonadecane. The pure phases are labelled by solid colours. The vertical lines are the experimental data. The exact shape of solidus and liquidus lines is uncertain in this phase diagram, but the overall appearance is no question. At lower concentrations of alkane, the behaviour of the blends is similar to the pure compound. Following the hexagonal columnar phase, P*m*$\bar{3}$*n* cubic and BCC phases are observed at higher temperatures in sequence. When around 15wt% nonadecane are mixed with 12-12-12Na, pure HCP phase is observed following the Colh phase. Note that the Colh-Colh phase transition disappears at a higher concentration of $C_{19}H_{40}$. The BCC phase is observed above HCP at higher temperatures. However, when more $C_{19}H_{40}$ is added, the blends turn into isotropic liquid directly following the Colh phase at high temperatures.

SAXS results of 12-12-12Rb + $C_{19}D_{40}$ blends are displayed in Figure 5.5. In the blends of 12-12-12Rb + 12.5wt% $C_{19}D_{40}$, shown in Figure 5.5 (a), only a mixture of Colh and HCP phases is observed at lower temperatures. This turns into a

pure P$m\bar{3}n$ phase with rising temperature. The BCC phase follows P$m\bar{3}n$ phase at higher temperatures in the heating scan. In 12-12-12Rb + 17.5wt% $C_{19}D_{40}$ (see Figure 5.5 (b)), a mixture of Colh and HCP phases is observed first. Then, pure HCP is obtained at higher temperatures. This transforms into isotropic liquid at higher temperatures. Table 5.3 lists the measured and calculating spacing of 12-12-12Rb + $C_{19}D_{40}$ blends.

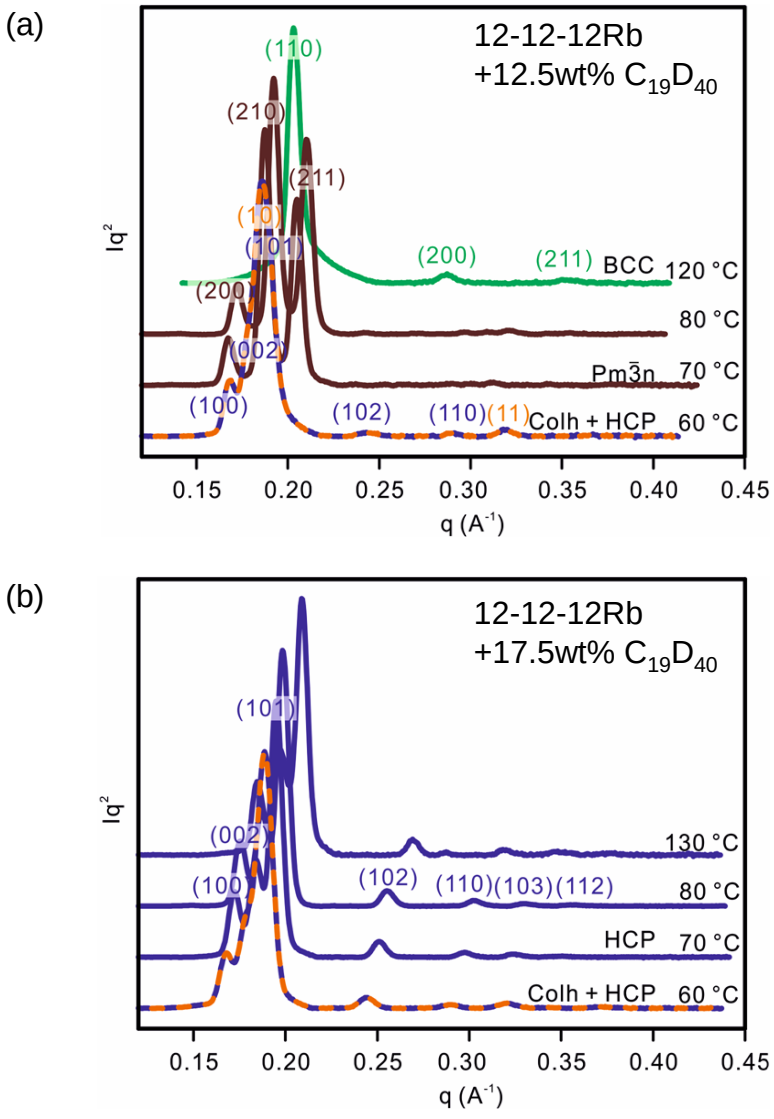

Figure 5.5. The SAXS curves of 12-12-12Na + (a) 12.5wt% $C_{19}D_{40}$, (b) 17.5wt% $C_{19}D_{40}$ in the heating scan.

Table 5.3 Measured and calculated spacing of 12-12-12Rb + $C_{19}D_{40}$ in different phases

blends	T (°C)	phase	(hkl)	d_{exp} (Å)	d_{cal} (Å)	lattice parameter (Å)	no. of molecules in cell
12-12-12Rb + 12.5wt% $C_{19}D_{40}$	80	Pm3n	(200)	36.5	36.5	a=73.0	269 12-12-12Rb 140 C19D40
			(210)	32.7	32.6		
			(211)	29.9	29.8		
			(220)	25.9	25.8		
			(310)	23.2	23.1		
			(222)	21.2	21.1		
	120	BCC	(110)	30.9	30.9	a=43.7	58 12-12-12Rb 30 $C_{19}D_{40}$
			(200)	21.9	21.8		
			(211)	17.8	17.8		
blends	T (°C)	phase	(hkl)	d_{exp} (Å)	d_{cal} (Å)	lattice parameter (Å)	no. of molecules in cell
12-12-12Rb + 17.5wt% $C_{19}D_{40}$	70	HCP	(100)	36.4	36.4	a=42.0 c=68.4	68 12-12-12Rb 35 $C_{19}D_{40}$
			(002)	34.2	34.3		
			(101)	32.3	32.1		
			(102)	25.0	25.0		
			(110)	21.1	20.7		
			(103)	19.4	19.4		
			(112)	18.0	17.9		
	130	HCP	(100)	34.0	34.0	a=39.2 c=63.6	56 12-12-12Rb 29 $C_{19}D_{40}$
			(002)	31.8	32.0		
			(101)	30.0	30.0		
			(102)	23.3	23.3		
			(110)	19.7	19.6		
			(103)	18.0	18.1		
			(112)	16.7	16.7		

The binary phase diagram of 12-12-12Rb + nonadecane is displayed in Figure 5.6. The vertical bars are based on experiments and the solid colour represents pure phase region. There is uncertainty in the shape of the solidus and liquidus lines but there is no doubt in overall appearance of the phase diagram. Similar with the blends of 12-12-12Na, at low concentration the mixtures show the P$m\bar{3}n$ phase following the 2-D Colh phase in the heating scan. Then, BCC appears at higher temperatures. When temperature goes higher, it would turn

into isotropic liquid. At around 15wt% $C_{19}H_{40}$, pure HCP phase is obtained. However, unlike 12-12-12Na blends, there is no 2-D liquid crystalline phase observed in the heating scan. The crystals melt directly into the HCP liquid crystals. On further heating HCP phase melts directly to isotropic liquid. No liquid crystal phase is observed as more n-alkane is added to 12-12-12Rb.

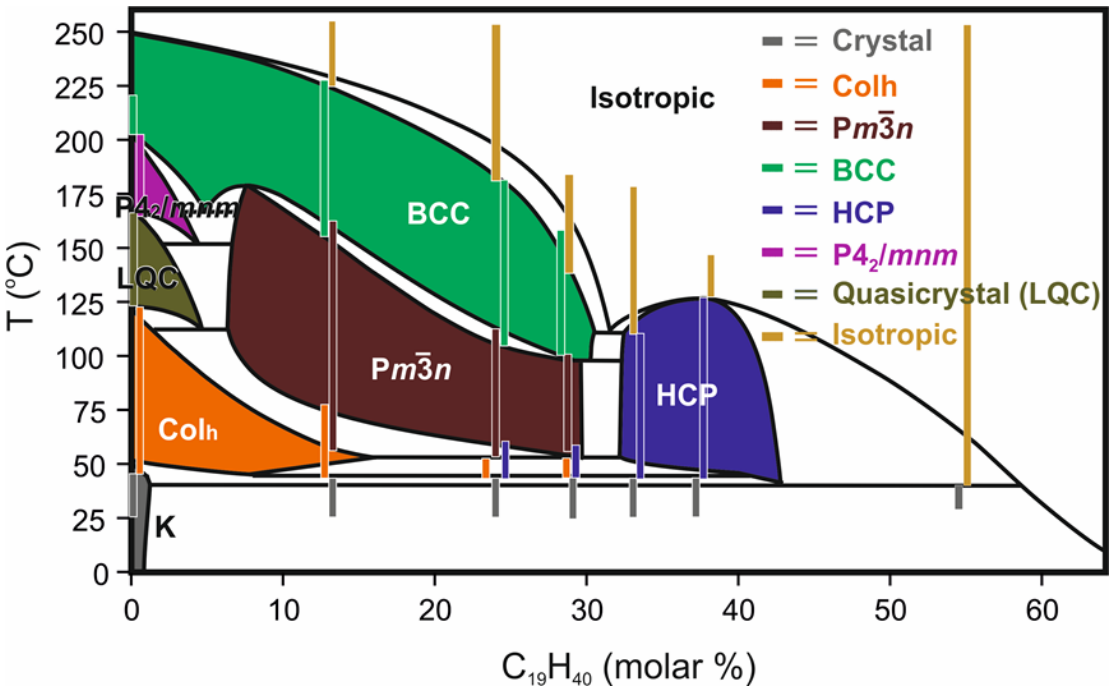

Figure 5.6. Binary phase diagram of 12-12-12Rb and $C_{19}H_{40}$

The electron density map (ED map) can be reconstructed from the SAXS pattern. In this case, the blend of 12-12-12Rb +17.5wt% $C_{19}D_{40}$ is chosen to reconstruct the ED map as there is no other 3-D phase involved and it shows more HCP reflections. Before that, in order to interpret the ED map, the electron density of the different parts of the mixture are computed. The minidendrons are separated into two different parts, aromatic core (including benzoate group, ether oxygen spacer and alkali ion) and alkyl tails, when calculating electron density. The minidendrons are treated as being in the crystal state. The molecular volume of the aromatic core and alkyl tails of 12-12-12Rb are estimated by using unitary crystal volumes[9]. It is assumed that the ratio of molecular volume/actual volume in crystal is constant. The calculated crystal

volume is obtained by summation of unit volume multiply multiplicities. Comparing with the experimental value, increment for elements and ions is evaluated. The molecular volume of d-nonadecane is calculated by the density at room temperature, which is 0.904 g/cm^3. [10] At room temperature, $C_{19}H_{40}$ is in rotator phase[11]. Note that the minidendrons and $C_{19}D_{40}$ in this case are in liquid crystal phase. The volume of the individual parts may be overrated. The results of the computed electron density are listed in Table 5.4.

Table 5.4 The electron density of different parts of 12-12-12Rb and $C_{19}D_{40}$

12-12-12Rb	Volume/molecule (nm^3)	no. of electrons	electron density (/nm^3)
aromatic parts* (+ oxygen spacer)	0.19	95	506.40
alkyl tails*	0.91	291	318.56
$C_{19}D_{40}$	0.57	154	271.56

* The volume is estimated by unitary crystal volumes[9]

Referring to Table 5.4, the aromatic core of the minidendrons has the highest electron density. The electron density of the alkyl tails and of $C_{19}D_{40}$ are similar and are seen as background. Figure 5.7 displays the reconstructed ED map of 12-12-12Rb +17.5wt% $C_{19}D_{40}$ in HCP phase. The preferred phase combination and the related intensity of the individual peaks are listed beside. The intensity of the reflections are Lorentz corrected[12]. The sites of the highest electron density are contributed by the aromatic cores of 1212-12Rb. As we known, the spherical supramolecules are assembled by the segregation of the aromatic group, while the aliphatic tails are relegated to the periphery[13]. Therefore, in Figure 5.7, the spheres of high electron density should represent the assembly of the benzoate groups of the minidendrons.

(a)

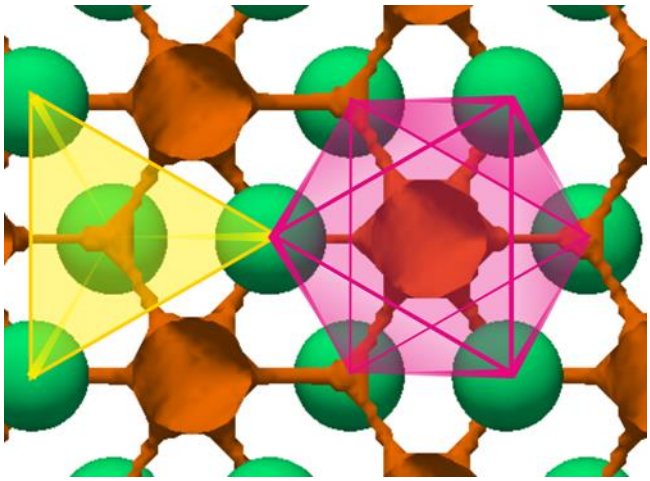

plane	intensity	phase
(100)	24.04	π
(002)	29.03	π
(101)	100.00	0
(102)	5.50	0
(110)	2.46	0
(103)	1.22	π
(112)	1.28	π

(b)

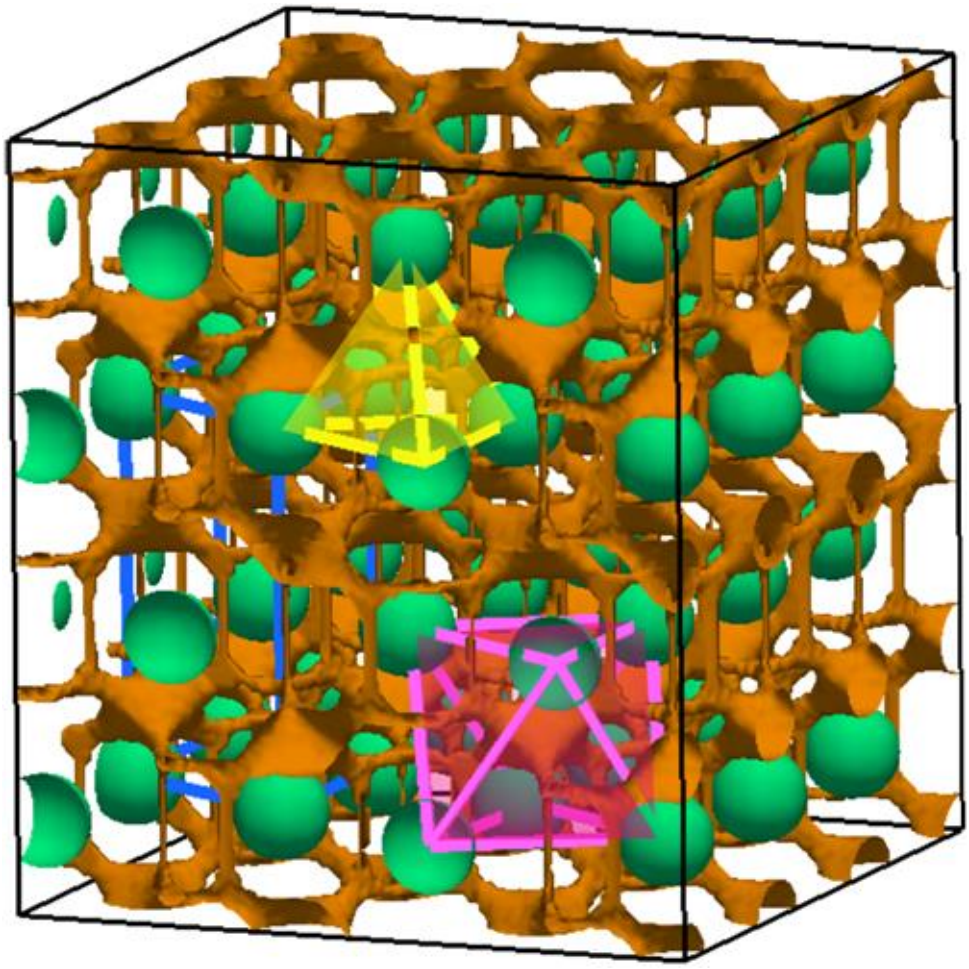

Figure 5.7. The contour maps of electron density of 12-12-12Rb + 17.5wt% $C_{19}D_{40}$ in the HCP phase: (a) top view and (b) side view. (Green: high ED; Orange: low ED; yellow: tetrahedron; pink: octahedron)

Moreover, the distribution of the low electron density positions shows interesting coincidence. In Figure 5.7, the tetrahedron composed of supramolecules is drawn and coloured yellow and the octahedron is coloured pink. In the centre of the tetrahedron, there is a small domain of the lowest electron density. That indicates the position of tetrahedral interstices in the HCP phase. Meanwhile, in the centre of the octahedron, there is another low electron density area, which is much larger than the tetrahedral one.

This result is consistent with our suggestion of pursuing close packed structure. The large octahedral interstices must be filled to make the close packed structure stable. Since the close packed structure only exists in minidendron-alkane blends, with the aid of added alkane the octahedral interstices become accessible. We believe that the added d-alkane should fill the octahedral gaps. However, SAXS cannot discriminate d-alkane from alkyl tails of minidendrons. Fortunately, the neutron scattering method would help us to resolve this problem.

The neutron scattering experiment is thus performed on the mixture of 12-12-12Rb +17.5wt% $C_{19}D_{40}$. Figure 5.8 shows the SANS result of 12-12-12Rb +17.5wt% $C_{19}D_{40}$ in the HCP phase accompanied by the SAXS result. In Figure 5.6, we can see that the diffraction pattern of SANS is quite different from the SAXS one. Only (100), (102), and (110) reflections are observed in the SANS curve. The strongest peak in SAXS, (101), is absent in neutron scattering and (100) becomes the strongest neutron scattering reflection. This difference implies the positon with high neutron scattering length density is not the same as the sites with high ED. The reconstruction of neutron scattering length density (NSLD) map from the SANS patterns hence becomes necessary. Theoretical NSLD of different parts of the blend are also computed before the construction of density map. The volume of the different parts of the minidendrons is also estimated by unitary crystal volumes. The molecular volume of $C_{19}D_{40}$ is taken as the volume at room temperature. The results of theoretical NSLD calculation of different molecular domains are listed in Table 5.5.

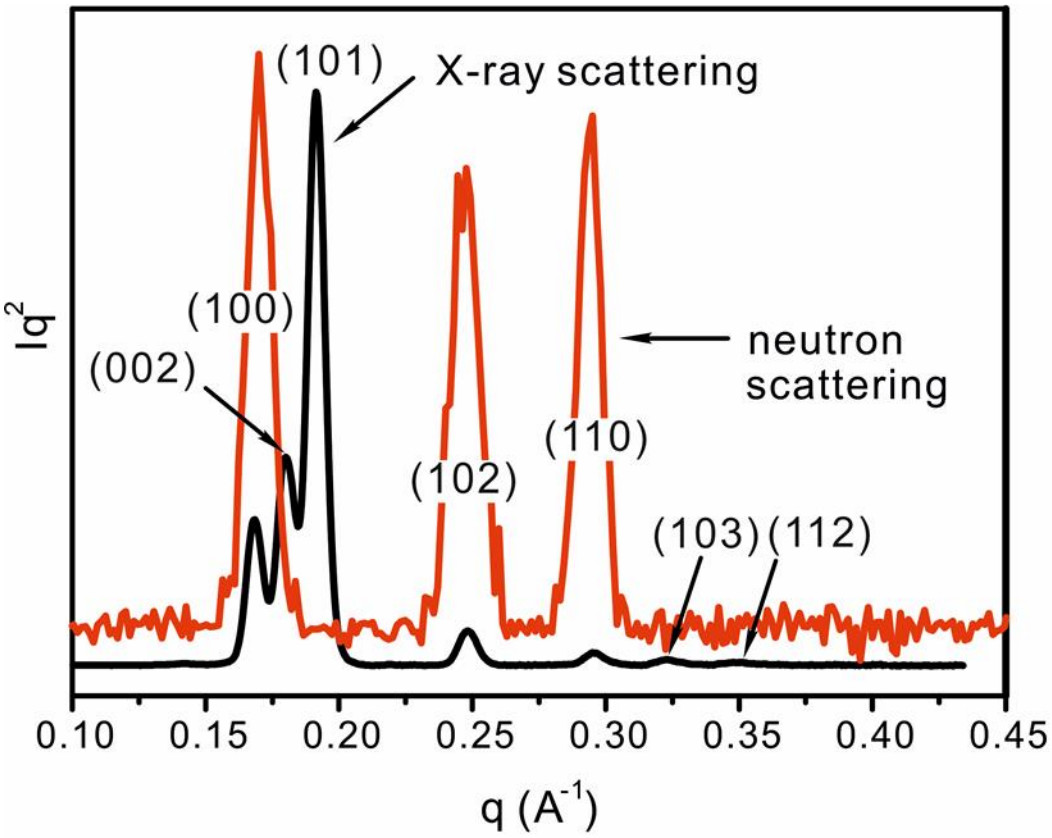

Figure 5.8. SANS results of 12-12-12Rb + 17.5wt% $C_{19}D_{40}$ in HCP phase compared with the SAXS results

Table 5.5 Neutron scattering length densities of different parts of 12-12-12Rb and $C_{19}D_{40}$

12-12-12Rb	molecular volume (nm^3)	coherent neutron scattering length (fm)[8]	neutron scattering length density ($10^{-6}/Å^2$)
aromatic parts* (+ oxygen spacer)	0.19	71.72	3.82
alkyl tails*	0.91	-41.10	-0.45
$C_{19}D_{40}$	0.57	393.19	6.93

* The volume is estimated by unitary crystal volumes[9]

(a)

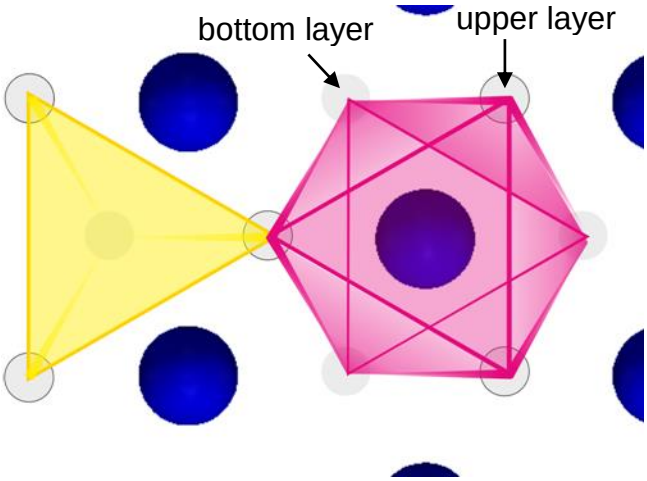

plane	intensity	Phase
(100)	100.00	0
(102)	95.23	0
(110)	91.61	0

(b)

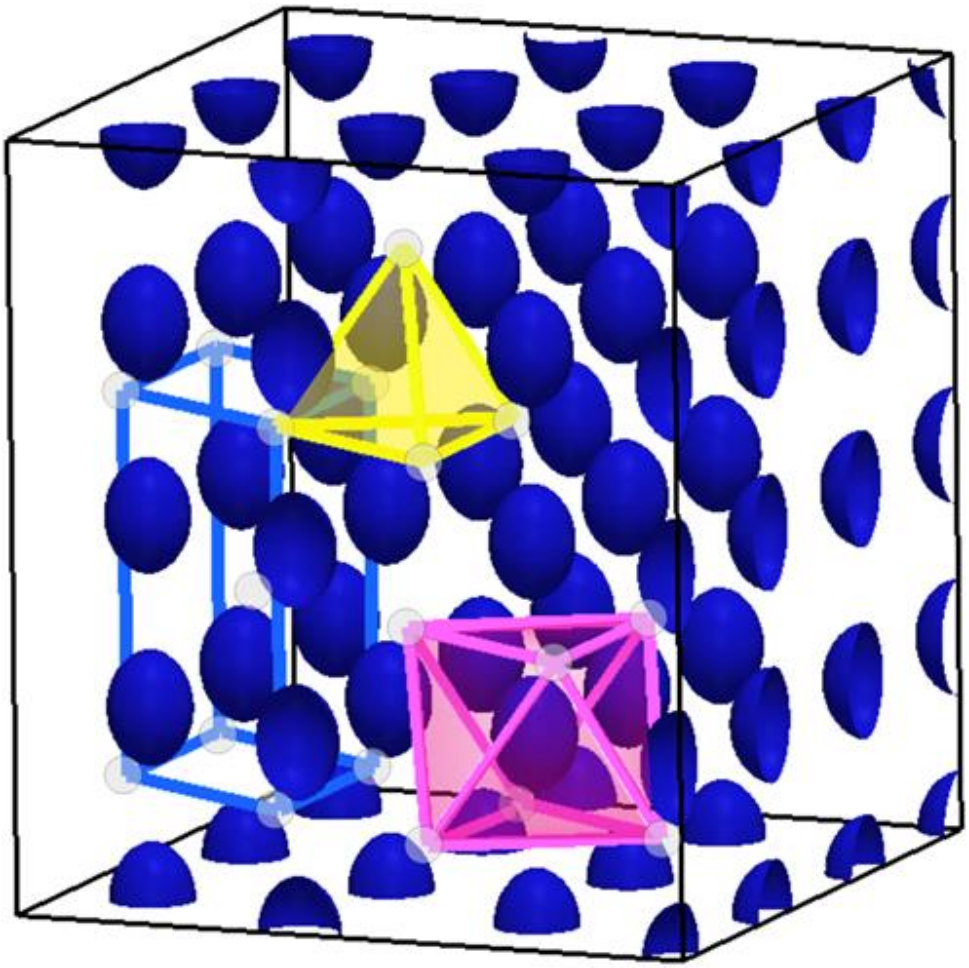

Figure 5.9. Neutron scattering length density contour map of 12-12-12Rb + 17.5wt% $C_{19}D_{40}$ in the HCP phase: (a) top view and (b) side view. (Blue: high NSLD density; gray sphere: supramolecule,; yellow: tetrahedron; pink: octahedron)

Referring to Table 5.5, the d-nonadecane has the highest NSLD. The NSLD of the aromatic cores of 12-12-12Rb is around half that of $C_{19}D_{40}$. The value of the alkyl tails of the minidendrons is weakly negative and it can be seen as background. Since the highest NSLD is contributed by $C_{19}D_{40}$, that explains why the SANS patterns is so different from SAXS pattern in HCP phase. The reconstructed NSLD map is displayed in Figure 5.9. The preferred phase combination and the relative intensities are listed beside. The intensities of the reflections are Lorentz corrected. Only the highest NSLD sites are shown in Figure 5.9. Compared with the positions of the tetrahedron and the octahedron shown in the ED map in Figure 5.9, we can see that the places with high NSLD are situated just inside the octahedron formed by micellar supramolecules. However, in the tetrahedron, there is no position showing high NSLD. This would imply that the tetrahedral interstices are filled with both alkyl tails of 12-12-12Rb and added d-alkane, or, without the aid of the additional alkane. Because the tetrahedral vacancies can be reached by the minidendrons themselves, the pure compounds can only form 3-D phases with only tetrahedral interstices. This is the reason why we can only observe tetrahedrally close packed phases in the soft spherical aggregates.

Furthermore, the high NSLD sites that located inside the octahedron would represent the octahedral interstices can be filled with the aid of the additional alkane. In order to interpret the NSLD map, it is important to match it with the ED map. We therefore superimpose these two density maps. Figure 5.10 shows the contour ED map overlapping the NSLD map in a HCP unit cell. In Figure 5.10, we can clearly see that the positions of lowest ED just coincide with the highest NSLD regions that is at the centres of the octahedral vacancies. Based on the computed NSLDs in the different parts of the molecules, the highest NSLD is contributed by d-alkane. Thus, we can confirm that the octahedral centres in the close packed structure are filled with the added alkane.

(a)

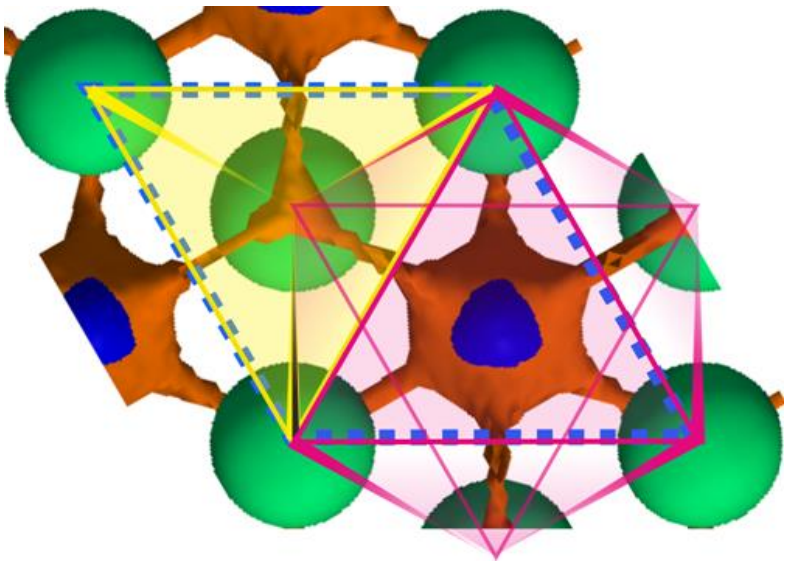

(b)

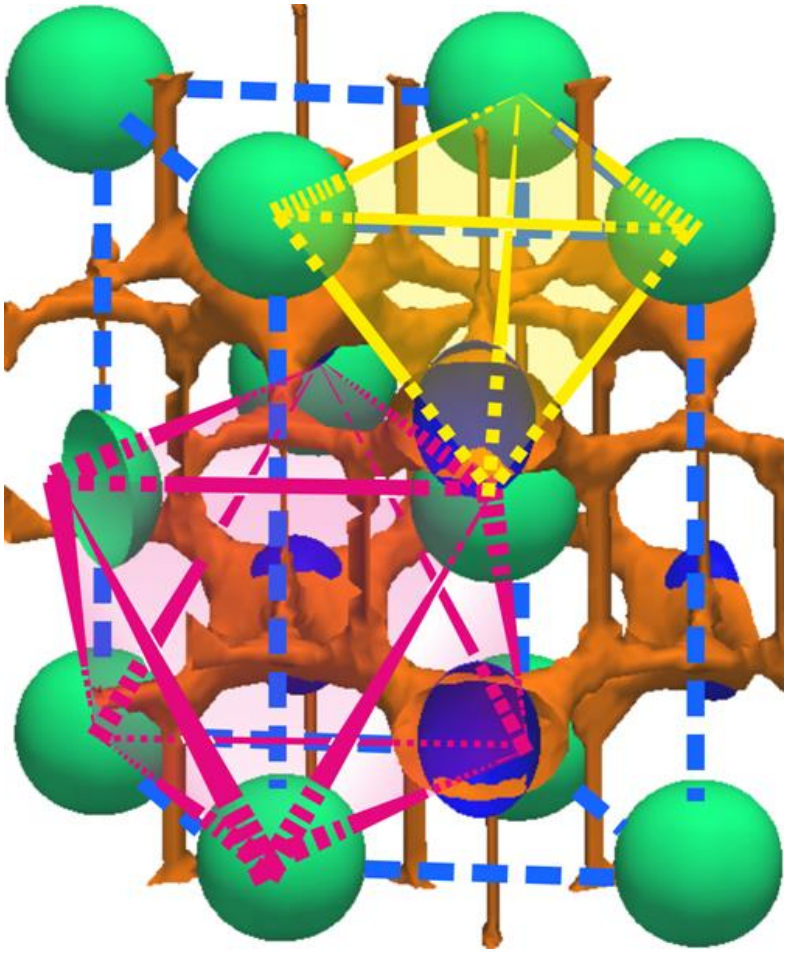

Figure 5.10. HCP unit cell: the contour of reconstructed electron density and neutron scattering length density maps of 12-12-12Rb + 17.5% $C_{19}D_{40}$ (a) top view and (b) side view. (Green: high electron density; Orange: low electron density; Blue: high neutron scattering length density; dashed blue line: unit cell, yellow line: tetrahedron; purple line: octahedron)

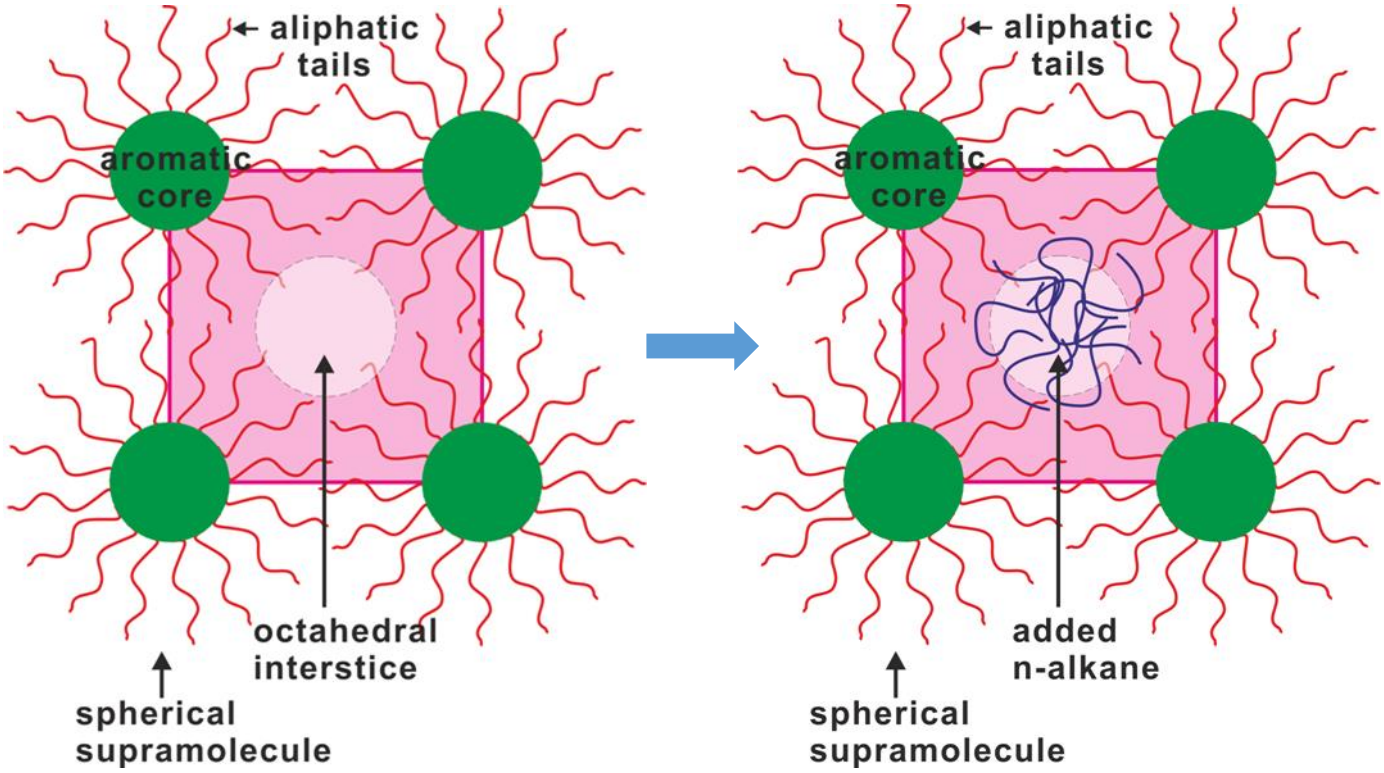

Figure 5.11. Schematic of the octahedral vacancy in the HCP phase filled by the added alkane

Figure 5.11 shows the schematic of the octahedral vacancy in the HCP phase filled by the added alkane. The limitation of the length of the alkyl tails of the minidendrons results in the centre of the octahedron is unreachable. In order to fill the vacancies, the lattice would distort and the distortion causes lattices strains. The close packed structure thus becomes unstable and absent in the dendron-based mesogens or other thermotropic liquid crystals. With the help of the additive, n-alkane in this case, the interstices are eliminated. The added alkane would segregate in the interstices and the vacancies are therefore annihilated. Moreover, the close packed structure is stabilised. This work thus explains the packing mechanism of the HCP phase in minidendrons.

5.4 Conclusion

In this project, the close packed structure is firstly found and investigated in tapered mesogens, or, thermotropic liquid crystals. Although wedge-shaped minidendrons self-assemble into spherical micelles and organise into 3-D cubic phases, the close packed structure was never observed before. The absence of close packed structures in the soft spherical supramolecules is due to the inaccessibility of the octahedral interstices. In other 3-D structures, only tetrahedral interstices exist.

The close packed structure should be obtained once the octahedral interstices are filled. Thus, small amounts of additive are mixed with the minidendron. Pure HCP phase is observed in 12-12-12Na + nonadecane and 12-12-12Rb + nonadecane blends. That means with the aid of additive, the octahedral interstices in HCP are filled. The close packed structure is thus stabilised. However, from the ED map, we can only tell the difference between the aromatic and aliphatic groups, and cannot tell apart the bound alkyl tails from the added free alkane.

To examine the alkane distribution in the HCP phase, deuterated alkane, $C_{19}D_{40}$, was used to replace nonadecane in the minidendron-alkane blends. Neutron scattering experiment are performed on the minidendron-d-alkane blends. Since deuterium can be distinguished from hydrogen in neutron scattering, the d-alkane can be discriminated from the undeuterated alkyl chains. Interestingly, through superposition of the ED map on the NSLD map, the high NSLD positions are seen to overlap with the low ED sites at the octahedral interstices. That indicates that the added alkane aggregates in the octahedral vacancies. The HCP phase is observed in the blends. Furthermore, the packing in the close structure is interpreted by the density maps.

Binary phase diagrams of 12-12-12Na-nonadecane and 12-12-12Rb-nonadecane are drawn from experimental data. From the binary phase diagram, we can also find that the concentration of the added alkane is also an important factor to control the wanted phases. At low concentration of additive, the minidendron-alkane blends show only 3-D mesophases with tetrahedral interstices. The behaviour is similar to that of the pure tapered mesogenic

dendron. Furthermore, when too much additive is mixed in with the minidendrons, the crystalline blends melt directly into isotropic liquid.

Reference

1. Ungar, G.; Zeng, X. B., Frank-Kasper, quasicrystalline and related phases in liquid crystals. *Soft Matter* **2005,** 1, (2), 95-106.

2. Ungar, G.; Percec, V.; Holerca, M. N.; Johansson, G.; Heck, J. A., Heat-shrinking spherical and columnar supramolecular dendrimers: Their interconversion and dependence of their shape on molecular taper angle. *Chem. Eur. J.* **2000,** 6, (7), 1258-1266.

3. Percec, V.; Holerca, M. N.; Uchida, S.; Cho, W. D.; Ungar, G.; Lee, Y. S.; Yeardley, D. J. P., Exploring and expanding the three-dimensional structural diversity of supramolecular dendrimers with the aid of libraries of alkali metals of their AB(3) minidendritic carboxylates. *Chem. Eur. J.* **2002,** 8, (5), 1106-1117.

4. Ungar, G.; Liu, Y. S.; Zeng, X. B.; Percec, V.; Cho, W. D., Giant supramolecular liquid crystal lattice. *Science* **2003,** 299, (5610), 1208-1211.

5. Balagurusamy, V. S. K.; Ungar, G.; Percec, V.; Johansson, G., Rational design of the first spherical supramolecular dendrimers self-organized in a novel thermotropic cubic liquid-crystalline phase and the determination of their shape by X-ray analysis. *J. Am. Chem. Soc.* **1997,** 119, (7), 1539-1555.

6. Li, Y. Y.; Lin, S. T.; Goddard, W. A., Efficiency of various lattices from hard ball to soft ball: Theoretical study of thermodynamic properties of dendrimer liquid crystal from atomistic simulation. *J. Am. Chem. Soc.* **2004,** 126, (6), 1872-1885.

7. Chaiprapa, J. New supramolecular liquid crystal structures in wedge-shaped molecules. Univ. of Sheffield, 2012.

8. http://www.ncnr.nist.gov/resources/n-lengths/.

9. Immirzi, A.; Perini, B., Prediction of density in organic crystals. *Acta Cryst.* **1977,** A33, 216-218.

10. http://www.chemicalbook.com/ChemicalProductProperty_EN_CB0269216.htm.

11. Ungar, G., Structure of rotator phases in n-alkanes. *J. Phys. Chem.* **1983,** 87, (4), 689-695.

12. Klug, H. P.; Alexander, L. E., *X-ray diffraction procedures : for polycrystalline and amorphous materials*. Wiley: New York, 1954.

13. Crane, A. J.; Mueller, E. A., Global phase behaviour of polyphilic tapered dendrons. *Soft Matter* **2011,** 7, (16), 7465-7476.

Chapter 6 Superlattice in Minidendron-Alkane Blends

6.1 Introduction

Tapered mesogens with flexible pendant chains often assemble in thermotropic columnar or cubic phases. For wedge-shaped alkali metal 3,4,5–tri(alkyloxy)benzoate salts (“minidendrons”) columns and spherical “micelles” in the cubic phases were found to shrink in diameter dramatically with increasing temperature[1-3]. This was explained by the wedge widening as the alkyl chains expand laterally due to increased conformational disorder. In turn this leads to exclusion of excess dendrons from a column or micelle and their subsequent reassembly in new columns/micelles. The exceptions are the salts of lithium, where the columnar diameter stays constant with increasing temperature, in fact increases slightly[2].

In our previous study, a series of mixtures of lithium 3,4-didodecyl-5-octadeceyloxybenzoate salt (12-12-18Li) with n-alkanes were prepared and the formation of a hexagonal columnar superlattice phase (Col**s**) at higher temperature range than the Colh phase was observed in these blends[4]. The superlattice is a structure formed by two or more than two kinds of components. The components in a cell is slightly different from each other and bigger supercell is drawn as repeat unit. Each of the components occupies specific geometrical sites and appears in periodical arrangement. Interestingly, when approaching the phase transition temperature, the diameter of the columns starts to shrink. Unlike the Colh-Colh phase transition in sodium minidendron, this shrinkage between the Colh and Col**s** phases is continuous. The diameter of the columns declines steadily in the superlattice phase with rising temperature. This phenomenon is only observed in lithium minidendron-alkane blends. That means the packing of lithium minidendrons is influenced by the additive.

A columnar superlattice phase has also found in nanoparticles (NPs) with liquid crystalline ligands[5] and discotic mesogens[6]. The packing density of columns of NPs is not all the same. Every two densely packed columns accompanied one dilute packed column. These two kinds of columns arrange into superlattice phase. Yeh and co-workers reported the superlattice phase observed in

dibenzo(a,c)phenazine derivatives shown in Scheme 1. The columns assemble triangularly, with the EG side chain in the centre. The localized EG side chains are seen as cylinder architectures and thus the superlattice is composed of three different kinds of columns.

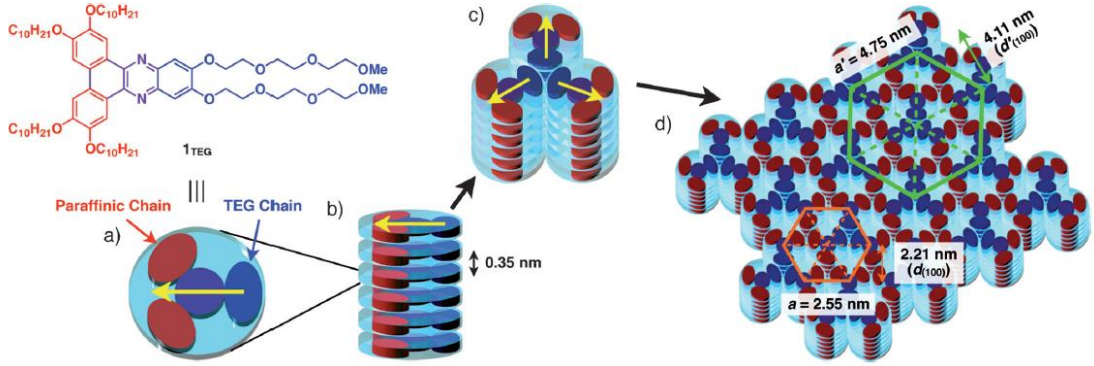

Scheme 1 Sketch of superlattice phase in dibenzo(a,c)phenazine derivatives[6].

In this chapter, we attempt to interpret the packing mode of molecules in the superlattice and understand the role of the added alkane. To locate the added alkanes, similar with the method mentioned in chapter 5, n-alkane is replaced by deuterated one when preparing the mixtures. The neutron scattering experiment can help to discriminate the deuterated alkane (d-alkane) from other alkyl chains.

Second, the decrease of the averaged diameter of columns indicates that the number of minidendrons in a stratum decreases. As we mentioned, in the superlattice there are two different sizes of columns in a unit cell. The number of molecules in the cross-section of a wide column must be higher than the narrow ones. From the powder SAXS, the information about the thickness of a single layer, or stratum, in the Colh phase and superlattice is missing. Thus, in this work, oriented fibre WAXS experiments are performed on the minidendron-alkane blends. By obtaining the thickness of single stratum, the average number of molecules in a Colh and Col**s** unit cell can be estimated. The molecular model thus can be built.

6.2 Experiments

Materials

In this chapter, two different kinds of minidendrons are used to prepare the blends. One is lithium 3,4,5-tridodecyloxybenzoate salt (12-12-12Li), which has three tails with the same length. The other one is lithium 3,4-didodecyloxy-5-octadecyloxybenzoate salt (12-12-18Li), which also has three tails but one is longer than the other two. Scheme 1 shows the chemical structure of the monodendrons. The synthesis of 12-12-12Li and 12-12-18Li samples are described in Chapter 3.1.1.

(a) 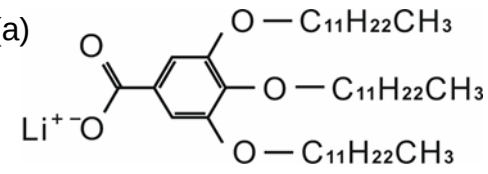

(b) 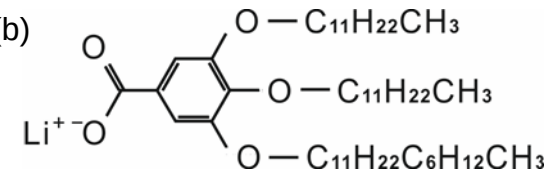

Scheme 2 Chemical structure of (a) 12-12-12Li and (b) 12-12-18Li

The composition of 12-12-12Li-d-alkane and 12-12-18Li-d-alkane blends are listed in Table 6.1. The preparation of the minidendron-alkane blends followed the procedure mentioned in Chapter 3.1.2.

Table 6.1. The composition of 12-12-12Li + $C_{19}D_{40}$ and 12-12-18Li + $C_{19}D_{40}$ in weight percent

	12-12-12Li+ 20wt% $C_{19}D_{40}$	12-12-12Li+ 25wt% $C_{19}D_{40}$	12-12-12Li+ 30wt% $C_{19}D_{40}$
$C_{19}D_{40}$ (%)	20	25	30
12-12-12Li (%)	80	75	70
	12-12-18Li+ 20wt% $C_{19}D_{40}$	12-12-18Li+ 25wt% $C_{19}D_{40}$	12-12-18Li+ 30wt% $C_{19}D_{40}$
$C_{19}D_{40}$ (%)	20	25	30
12-12-18Li (%)	80	75	70

The samples are put in capillaries for powder SAXS and fibre WAXS. The procedure of specimen preparation is described in Chapter 3.2.2.

The oriented fibres are prepared following the procedure in Chapter 3.1.3. The extrusion temperature of all 12-12-12Li blends and 12-12-18Li blends was room temperature.

The preparation of the powder samples for neutron scattering experiments is described in Chapter 3.3.2.

Methods

The details of both powder SAXS and fibre WAXS experiments are mentioned in Chapter 3.2.2. The procedure of data reduction of both SAXS and WAXS is following the method mentioned in Chapter 3.4.1.

The details of SANS experiments are mentioned in Chapter 3.3.2. The procedure of neutron data reduction are mentioned in Chapter 3.3.3. The reconstruction of density map is following the method mentioned in Chapter 3.4.2.

6.3 Results and Discussion

The SAXS experiments on the series of 12-12-18Li + n-alkane were performed by Jitrin Chaiprapa[4]. Figure 6.1 displays the SAXS traces of 12-12-18Li + 30wt% $C_{17}H_{36}$ in the heating scan. The blend shows the Colh phase at lower temperatures. Then, the Col**s** phase is observed above the temperature range of the Colh phase. With rising temperature, it turns into isotropic liquid without showing any 3-D liquid crystalline phase.

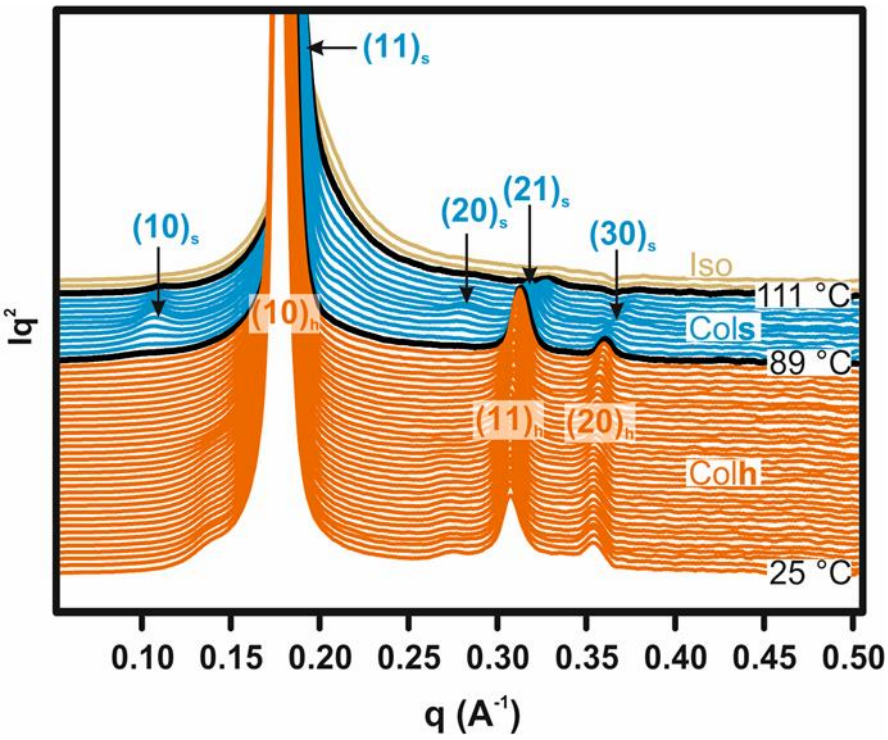

Figure 6.1. SAXS traces of 12-12-18Li + 30wt% $C_{17}H_{36}$ in the first heating scan by Jitrin Chaiprapa[4].

However, in order to see where the added alkanes aggregate, $C_{19}D_{40}$, in this project, replaces hydrogenous n-alkane to prepare the blends. Furthermore, since the superlattice is shown in 12-12-18Li blends, we believe it should exist in 12-12-12Li blends as well. Thus, two different series of mixtures are prepared. Figure 6.2 displays the SAXS patterns of 12-12-18Li + 20wt%, 25wt%, and 30wt% $C_{19}D_{40}$.

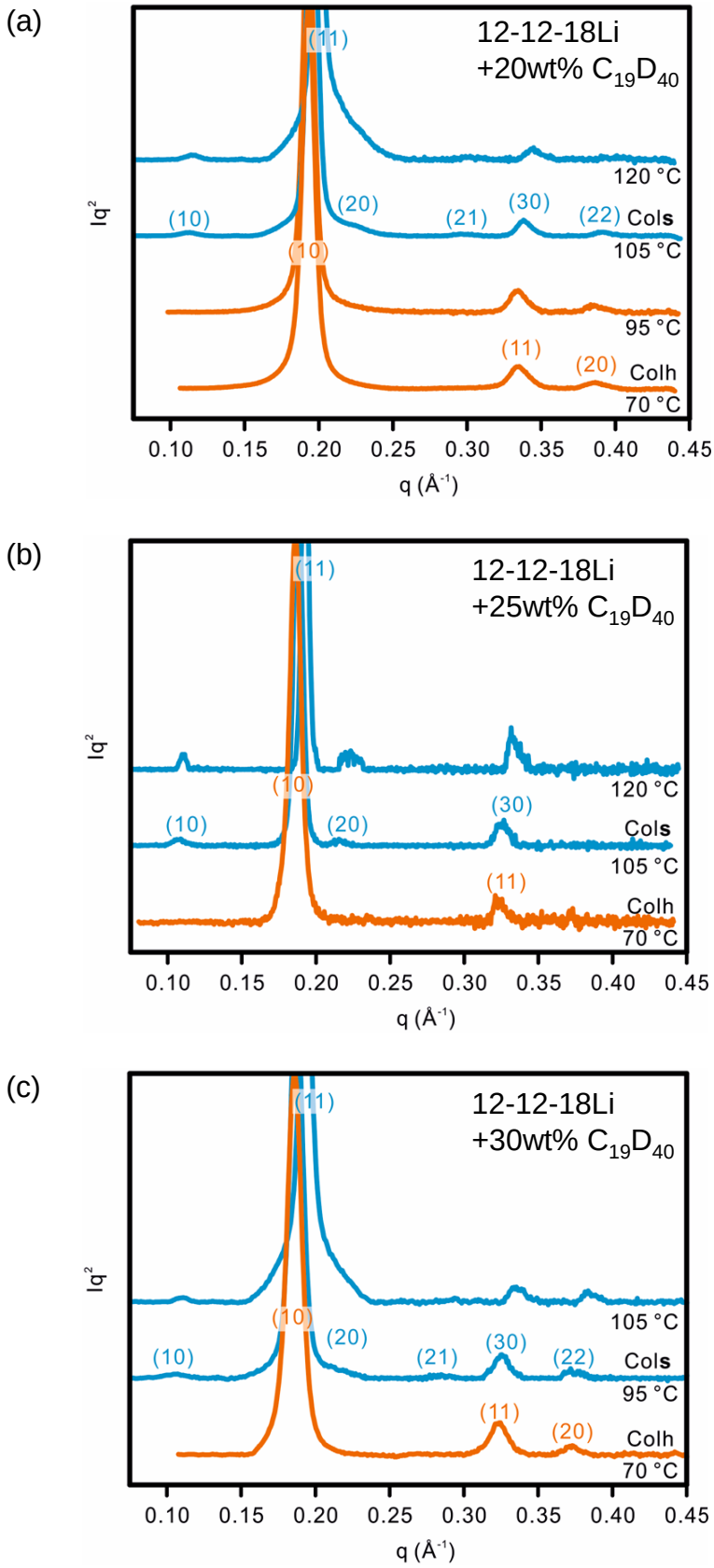

Figure 6.2. The SAXS curves of 12-12-18Li + (a) 20wt% $C_{19}D_{40}$, (b) 25wt% $C_{19}D_{40}$, and (c) 30wt% $C_{19}D_{40}$ in the heating scan.

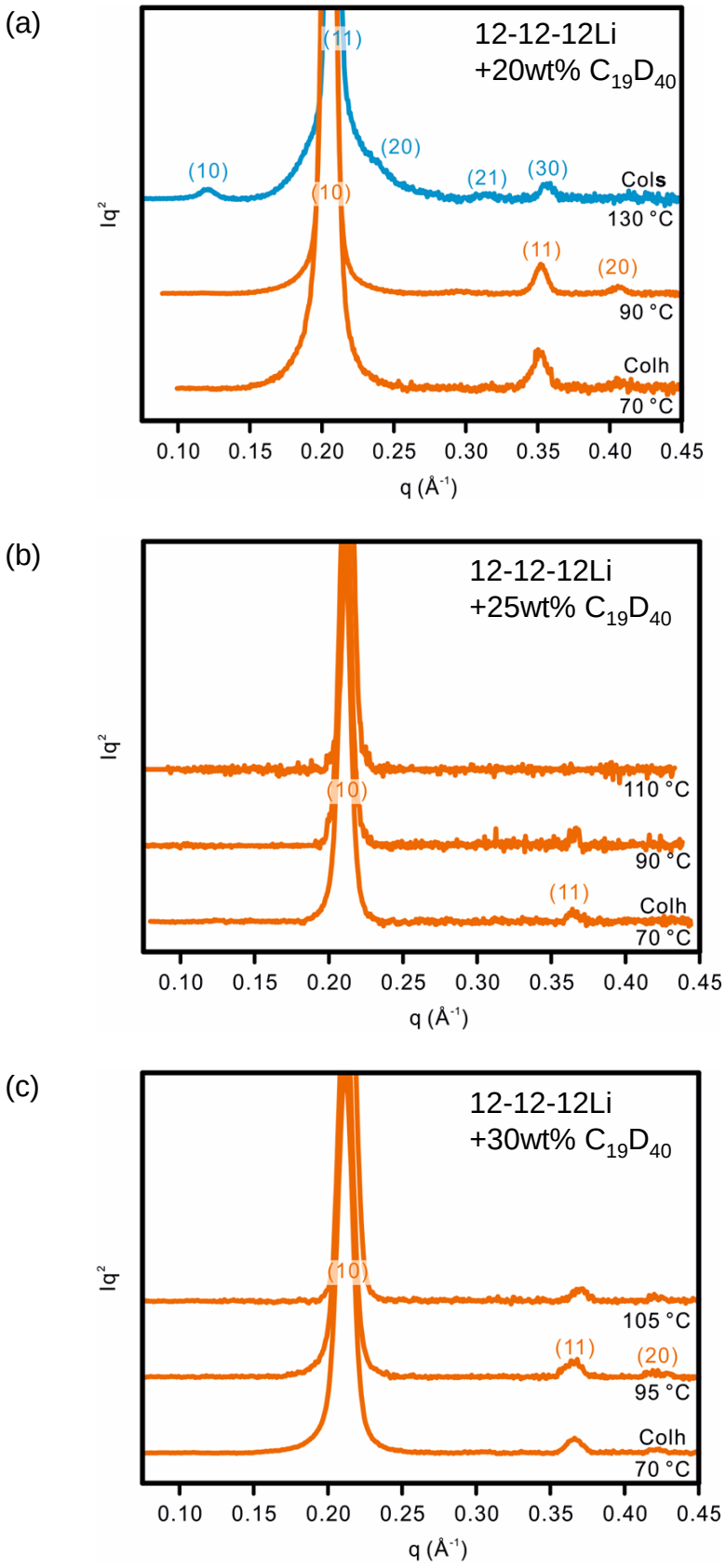

Figure 6.3. The SAXS curves of 12-12-12Li + (a) 20wt% $C_{19}D_{40}$, (b) 25wt% $C_{19}D_{40}$, and (c) 30wt% $C_{19}D_{40}$ in the heating scan.

From Figure 6.2, superlattice phase is observed in all of the prepared 12-12-18Li + $C_{19}D_{40}$ blends at higher temperature range than the Colh phase. In the superlattice phase, the SAXS patterns show the peaks in the Colh phase with additional $(10)_{Cols}$, $(20)_{Cols}$, and $(21)_{Cols}$ reflections. The q^2 ratio of $(10)_{Cols}$ to $(11)_{Cols}$ is 1:3. The samples become isotropic liquid at higher temperatures. However, in 12-12-12Li + d-alkane blends, the superlattice only exists in the mixture of 12-12-12Li + 20wt% $C_{19}D_{40}$. The SAXS curves of 12-12-12Li + 20wt%, 25wt%, and 30wt% $C_{19}D_{40}$ blends are displayed in Figure 6.3. In other mixtures with higher alkane concentration, they show only Colh liquid crystalline phase and then turn into isotropic liquid at higher temperature directly.

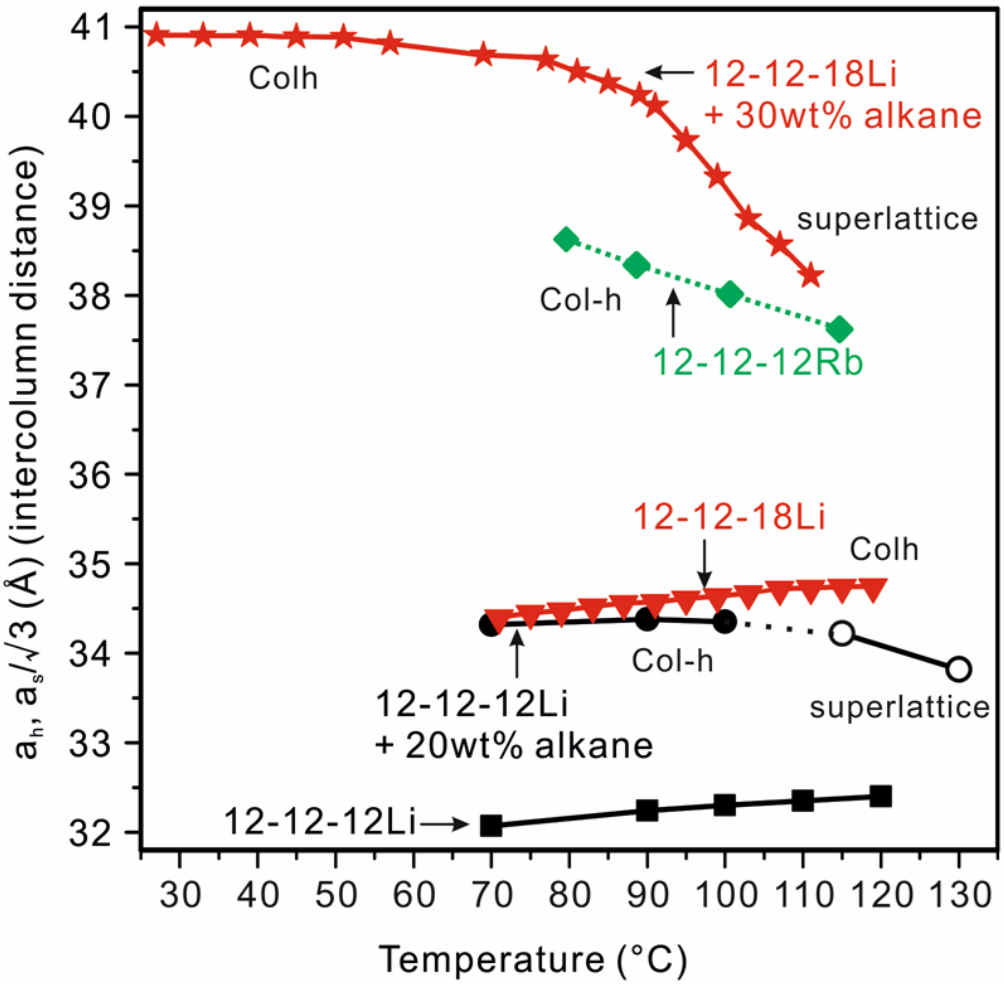

Figure 6.4. The inter-column distance of 12-12-12Rb, 12-12-12Li, 12-12-18Li, 12-12-12Li + 20wt% $C_{19}D_{40}$, and 12-12-18Li + 30wt% $C_{17}H_{36}$ at different temperature.

The inter-column distance in different compounds are plotted in Figure 6.4. In other alkali minidendrons, such as 12-12-12Rb, the diameter of columns declines with rising temperature, while it is almost fixed in both 12-12-12Li and 12-12-18Li. But, the decrease of inter-column distance in the superlattice is observed in both 12-12-12Li and 12-12-18Li blends. In the Colh phase region, the lattice parameter is almost steady. Moreover, although there is only Colh phase shown in 12-12-12Li + 25wt% and 30wt% $C_{19}D_{40}$, the lattice parameter also decreases at higher temperatures. So, with the aid of added alkane, the size of the columns is allowed to shrink in lithium salts. The decrease of the diameter of columns implies that the number of molecules in a stratum also decreases with increasing temperature.

The electron density (ED) map reveals more details about the packing in the Colh phase and superlattice phase. In this project, 12-12-12Li + 20wt% $C_{19}D_{40}$ and 12-12-18Li + 20wt% $C_{19}D_{40}$ are used to reconstruct the ED map since both of them show superlattice liquid crystal. The electron density of different parts of the minidendrons and of $C_{19}D_{40}$ are estimated. We separate the minidendron molecule into aromatic cores (including benzoate group, lithium ion and oxygen spacer) and alkyl tails. The volume of the individual parts of monodendrons are seen as in a crystal and estimated by unitary crystal volumes[7]. The theoretical molecular volume is calculated by sum of the volume increments, or the unitary crystal volume. The unitary crystal volume of atoms (or group of atoms) is evaluated from finding the minimum difference between experimental and theoretical molecular volumes. The volume of $C_{19}D_{40}$ is computed from the density at room temperature. The density of $C_{19}D_{40}$ is 0.904 g/ml at room temperature[8]. The calculated results of electron density are listed in Table 6.2. In both blends, the aromatic cores of minidendrons have the highest electron density. The electron density of the alkyl tails of minidendrons is around 40% lower than the aromatic cores and it is slightly higher than the added alkane. We can assume the electron density of the alkyl tails and added alkane are the same.

Table 6.2. The electron density of different part of 12-12-12Li, 12-12-18Li and $C_{19}D_{40}$

12-12-12Li	Volume/molecule (nm^3)	no. of electrons	electron density ($/nm^3$)
aromatic parts* (+ oxygen spacer)	0.17	87	520.65
alkyl tails*	0.91	291	318.56
12-12-18Li	Volume/molecule (nm^3)	no. of electrons	electron density ($/nm^3$)
aromatic parts* (+ oxygen spacer)	0.17	87	520.65
alkyl tails*	1.06	339	319.12
$C_{19}D_{40}$	0.57	154	271.56

* The volume is estimated by unitary crystal volumes[9]

The ED maps of 12-12-12Li + 20wt% $C_{19}D_{40}$ in the Colh phase and superlattice phase are shown in Figure 6.5 (a) and (b). The relative intensity of each reflections and the preferred phase combination of both Colh phase and superlattice phase are listed below. Other possible phase combinations of density maps in the superlattice are in Appendix. In the Colh phase, one column exists in each unit cell and all of the columns in the density map are the same and composed of high electron density core and low electron density periphery. Since the aromatic core has the highest electron density and the electron density of alkyl chains is lower, the minidendrons arrange into micellar supramolecular columns. The benzoate groups self-assemble together and the aliphatic chains are relegated to the corona region. In the superlattice, each unit cell has three columns in it. However, not all of them are the same. The column situated at the corner of unit cell obviously has smaller high ED core regions than the other two in the centre of unit cell. That means each super cell contains two different kinds of columns. Furthermore, the arrangement of these two kinds of columns has *p6mm* symmetry. Same phenomenon is found in the ED maps of 12-12-18Li + 20wt% $C_{19}D_{40}$ displayed in Figure 6.5 (c) and (d).

(a)

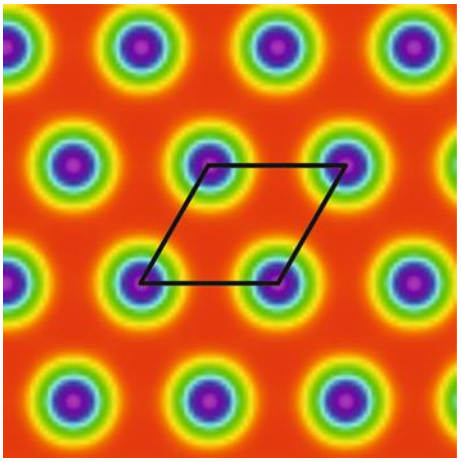

(b)

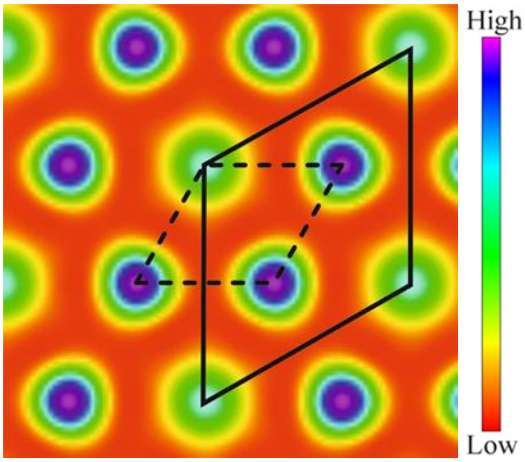

	plane	intensity	phase
Colh	(10)	100.00	0
	(11)	4.13	0
	(20)	0.92	0

	plane	intensity	phase
Cols	(10)	2.33	π
	(11)	100.00	0
	(20)	1.37	π
	(21)	1.40	π
	(30)	3.61	0
	(22)	0.29	0

(c)

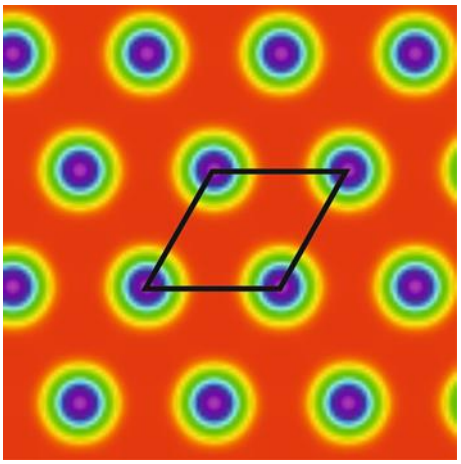

(d)

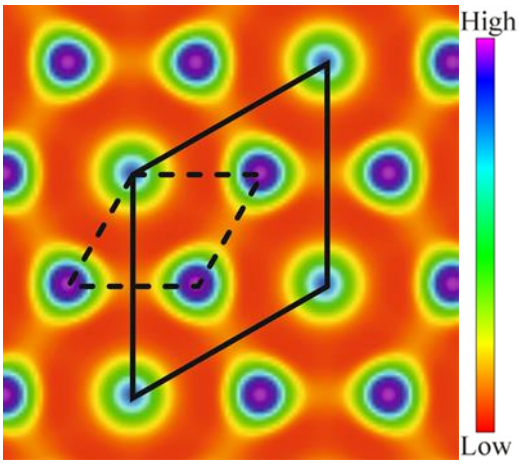

	plane	intensity	phase
Colh	(10)	100	0
	(11)	8.02	0
	(20)	2.07	0

	plane	intensity	phase
Cols	(10)	1.73	π
	(11)	100.00	0
	(21)	1.27	π
	(30)	6.59	0
	(22)	1.00	0

Figure 6.5 Electron density maps of 12-12-12Li + 20wt% $C_{19}D_{40}$ (a,b) and 12-12-18Li + 20wt% $C_{19}D_{40}$ (c,d) in the Colh (a,c) and superlattice phase (b,d).

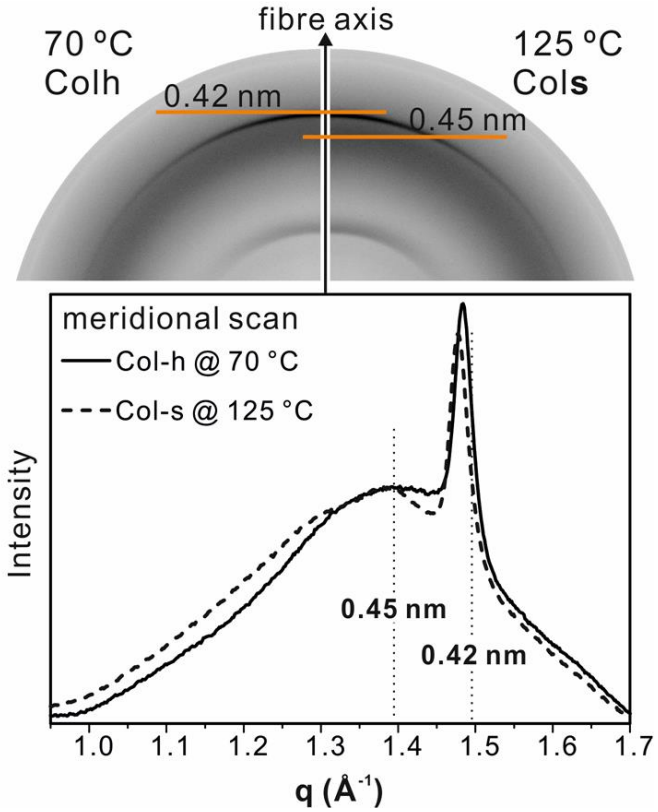

Figure 6.6 Fibre WAXS patterns of 12-12-12Li + 20wt% $C_{19}D_{40}$ in the Colh phase and superlattice phase.

Since the difference between the columns in the superlattice is in the high density area, we believe that the number of molecules in a stratum is different in a wide column (with large high ED area) and a narrow one (with smaller high ED area). In order to estimate the number of molecules in a unit cell, the thickness of a stratum, i.e. *c* parameter, is needed. As the information on c parameter is missing in the SAXS experiments, fibre WAXS experiment is performed on the oriented fibre samples. Figure 6.6 shows the fibre WAXS patterns of 12-12-12Li + 20wt% $C_{19}D_{40}$ in the Colh phase and superlattice. The *q* value of the sharp meridional reflection is the same in both phases and the corresponding spacing is 0.42 nm. As we mentioned in Chapter 4, the sharp meridional reflection results from the π-π stacking of aromatic groups, it can be seen as the spacing between two adjacent layers, i.e. *c* parameter. The fibre WAXS experiment is performed on 12-12-18Li blends as well to obtain *c*

parameter. The WAXS pattern of 12-12-18Li + 20wt% $C_{19}D_{40}$ is displayed in Figure 6.7. From Figure 6.7, *c* parameter is also fixed at 0.42 nm in both Colh phase and superlattice in 12-12-18Li blends.

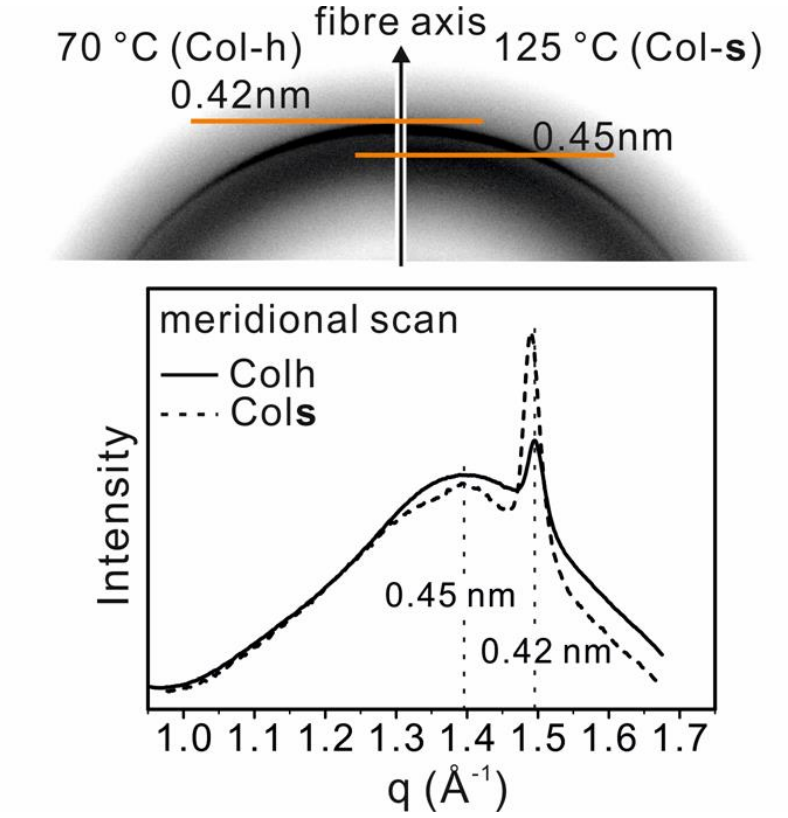

Figure 6.7 Fibre WAXS patterns of 12-12-18Li + 20wt% $C_{19}D_{40}$ in the Colh phase and superlattice phase.

The volume of a unit cell in the Colh phase and superlattice thus can be computed in both 12-12-12Li and 12-12-18Li blends. In addition, to estimate the number of molecules in a unit cell, the molecular volumes are also needed. In this case, we just treat $C_{19}D_{40}$ as $C_{19}H_{40}$. Assuming the thermal expansion coefficient of blends, which is including lithium minidendrons (12-12-12Li or 12-12-18Li) and $C_{19}D_{40}$, is the same as $C_{12}H_{26}$[7]. The thermal expansion coefficient is applied from 0 - 210 °C. The density of 12-12-12Li and $C_{19}H_{40}$ are 1.01 g/ml and 0.79 g/ml at room temperature respectively[3, 8]. Assume the density of 12-12-18Li is 0.99 g/ml at room temperature. The number of molecules in a unit cell can be deduced by:

$$n_1 = \frac{\sqrt{3}}{2} \frac{N_A {a_h}^2 l}{M_1 \left(\frac{1}{\rho_1} + \frac{C_2}{C_1} \cdot \frac{1}{\rho_2}\right)}$$

$$n_2 = \frac{\sqrt{3}}{2} \frac{N_A {a_h}^2 l}{M_2 \left(\frac{1}{\rho_2} + \frac{C_1}{C_2} \cdot \frac{1}{\rho_1}\right)}$$

, where n is the number of molecule in a unit cell of the blend, N_A is Avogadro number, a_h is the lattice parameter of the unit cell in hexagonal columnar phase, and l is the spacing between two adjacent layers. ρ is the density of the molecule, and C denotes to the weight percentage of the molecules in the blends. The subscripts “1” and “2” mean the molecule 1 and molecule 2 in this binary mixture.

The estimated numbers of molecules in a unit cell are listed in Table 6.3 for 12-12-12Li blend and Table 6.4 for 12-12-18Li blend. In 12-12-12Li + 20wt% $C_{19}D_{40}$, the Colh unit cell has three minidendrons and 1.5 free alkane molecules. That means a stratum of the Colh column consists of 3 minidendrons and 1.5 added alkane molecules on average. In a superlattice unit cell, there are 8 minidendrons and 5 added alkanes. Since there are three columns in a Col**s** unit cell, the average number of minidendrons per stratum becomes non-integer. But, as shown by the ED map, the number of molecules in a layer of a wide column should be different from that in a narrow column. The non-integer average molecules in a stratum is possible. In addition, the average number of added alkane per stratum is also non-integer. That implies they may gather more around the narrow columns.

However, from the estimation from the cell volume, only the number of molecules per cell is obtained. However, the distribution of dendrons between the different columns is estimated from the ED maps as follows. When we set the electron density of alkyl chains as background, the excess electron density should belong to the aromatic rings. Thus, the ratio of integrated excess electron densities in the wide and narrow columns must be equal to the ratio of the numbers of minidendrons in those columns. The ED map of 12-12-12Li + 20wt% $C_{19}D_{40}$ in the superlattice is used to calculate the excess density. The integration results and the suggested numbers are listed in Table 6.5. The ratio of integrating excess electron density in the wide and narrow columns is equal

to 1.57. Based on the cell volume, the number of molecules per cell is 7.7. This would give 1.9 minidendrons per layer in the narrow column. We can therefore suggest that a stratum of a narrow column in the superlattice is composed of 2 minidendrons. At the same time a wide column has 2.9 12-12-12Li molecules. Thus, we can suggest the wide one consists of 3 minidendrons in each stratum.

Table 6.3. Estimated number of 12-12-12Li and $C_{19}D_{40}$ molecules in the Colh and superlattice phases

12-12-12Li + 20% $C_{19}D_{40}$		
	Col-h (at 70 °C)	superlattice (at 130 °C)
a (nm)	3.42	5.86
c (nm)	0.42	0.42
V of unit cell (nm^3)	4.26	12.42
V of 12-12-12Li (nm^3/molecule)*	1.16	1.22
V of $C_{19}D_{40}$ (nm^3/molecule)**	0.59	0.63
no. of 12-12-12Li		
estimated in cell	2.77	7.69
in stratum (rounded to nearest integer)	3	2, 3, 3
no. of $C_{19}D_{40}$		
estimated in cell	1.53	4.87
in stratum (rounded to half integer)	1.5	3, 1, 1

*Assuming the thermal expansion coefficient of 12-12-12Li is the same with that of $C_{12}H_{26}$.

** The volume of $C_{19}D_{40}$ is seen the same as that in $C_{19}H_{40}$.

Table 6.4. Estimated number of 12-12-18Li and $C_{19}D_{40}$ molecules in the Colh and superlattice phases by cell volume.

12-12-18Li + 20% $C_{19}D_{40}$		
	Col-h (at 70 °C)	Superlattice (at 105 °C)
a (nm)	3.76	6.39
c (nm)	0.42	0.42
V of unit cell (nm^3)	5.11	14.79
V of 12-12-18Li* (nm^3/molecule)	1.34	1.39
V of $C_{19}D_{40}$** (nm^3/molecule)	0.59	0.61
no. of 12-12-18Li		
estimated in cell	2.93	8.08
in stratum	3	2, 3, 3
no. of $C_{19}D_{40}$		
estimated in cell	2.08	5.75
in stratum	2	3.5, 1, 1

*Assuming the thermal expansion coefficient of 12-12-18Li is the same with that of $C_{12}H_{26}$.

** Assuming the thermal expansion coefficient of $C_{19}D_{40}$ is the same with that of $C_{12}H_{26}$.

Thus the number of 12-12-12Li in wide columns is the same as the number in the Colh columns, while only two 12-12-12Li molecules are found in a narrow column stratum. The total number of 12-12-12Li in a unit cell is eight. It is proposed that the added alkane aggregates preferentially around the 2-dendron columns. Thus, in the superlattice, the two wide columns each contain 3 minidendrons and one free alkane per layer. The third, narrow column, has only two minidendrons and 2 alkane molecules. In 12-12-18Li + 20wt% $C_{19}D_{40}$, the Colh columns also consists of three minidendrons per stratum and there are 2 free alkane aggregating around the columns. In a superlattice cell, there are eight minidendrons and five $C_{19}D_{40}$. Similar with blend of 12-12-12Li, we assume the wide column consist of three 12-12-18Li and one alkane surrounds

the column. The narrow one has only two minidendrons but 3.5 free alkane aggregate around it.

Table 6.5 Number of 12-12-12Li molecules in the 2 types of columns in the superlattice suggested by integrated excess electron density*

12-12-12Li + 20wt% $C_{19}D_{40}$ in the superlattice phase			
	estimated no. of 12-12-12Li	relative excess electron density (using narrow columns as reference) integrated from ED map (-+--++)	Suggested no. of 12-12-12Li
unit cell	7.9	--	8
Col-wide	--	1.57	3
Col-narrow	--	1.00	2
unit cell = 2*Col-wide + 1*Col-narrow			

*set the electron density of the alkyl chains as background

Neutron scattering experiments are performed on 12-12-12Li + 20wt% $C_{19}D_{40}$ and 12-12-18Li + 20wt% $C_{19}D_{40}$ blends. In the neutron scattering experiment, deuterated alkane can be distinguished from non-deuterated alkyl chains because the coherent neutron scattering length of $-CH_2-$ is -0.83 fm and CD_2 is 19.99 fm[10]. Figure 6.8 displays the SANS results of 12-12-12Li + 20wt% $C_{19}D_{40}$ and 12-12-18Li + 20wt% $C_{19}D_{40}$ alongside SAXS results in both the Colh phase and superlattice. The SANS patterns is quite different from the SAXS results and both blends shows similar behaviour. In the Colh phase, the (10) reflection is the strongest in SAXS. But it becomes the weakest reflection in SANS pattern and the strongest reflection in SANS pattern is (11). In the superlattice, (h0) reflections are all stronger in SANS than in SAXS. The strongest peak in SAXS patterns is (11), while (30) is the strongest reflection in SANS results. Note the

weak reflection at q= 0.11 $Å^{-1}$ of 12-12-18Li + 20wt% $C_{19}D_{40}$ in Colh phase is the residual signal of superlattice.

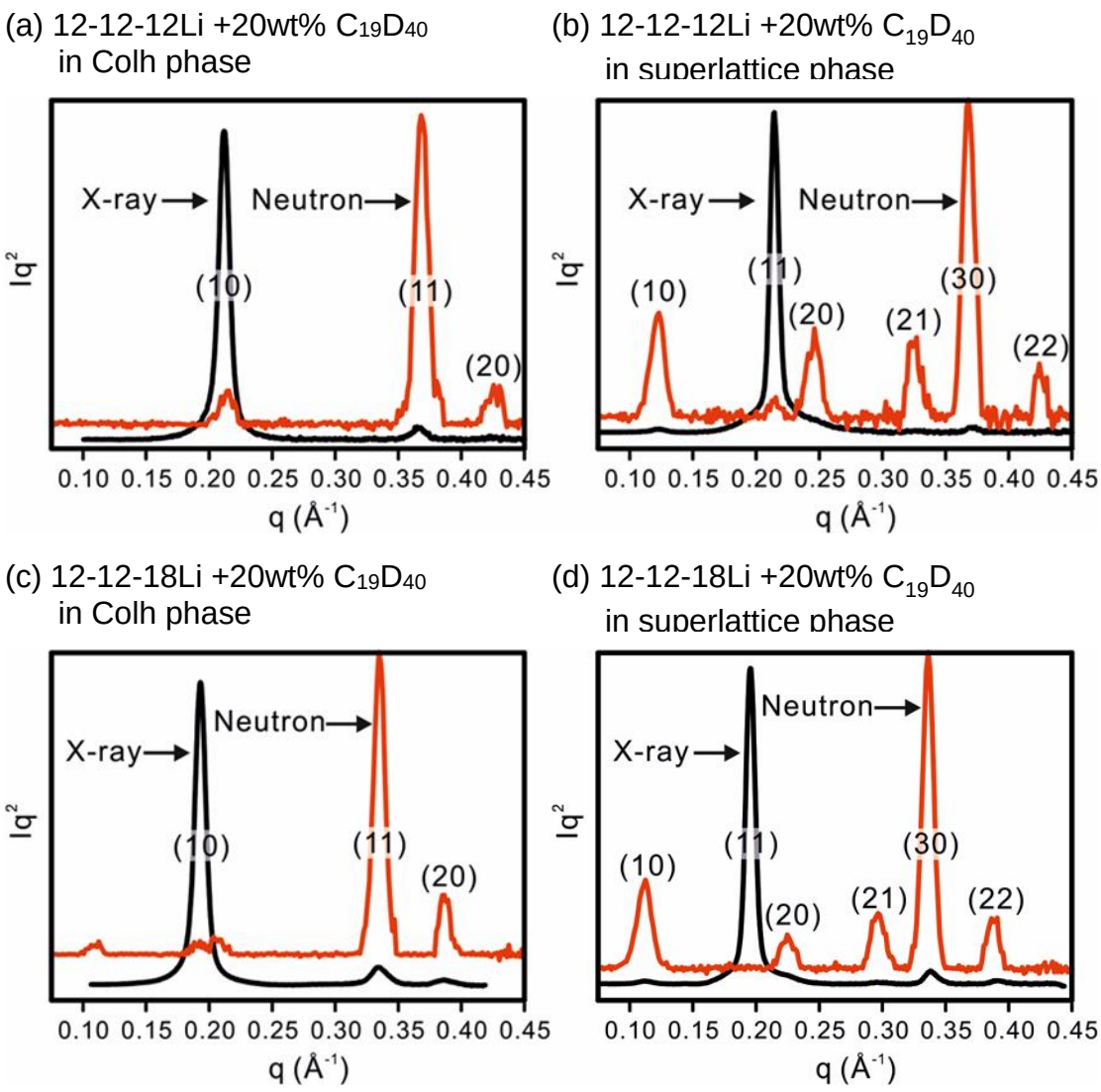

Figure 6.8. The SANS pattern of 12-12-12Li + 20wt% $C_{19}D_{40}$ in the (a) Colh phase and (b) superlattice phase accompanied with SAXS results. The SANS patterns of 12-12-18Li + 20wt% $C_{19}D_{40}$ in the (c) Colh phase and (d) superlattice phase accompanied with SAXS results.

The neutron scattering length density (NSLD) map can be reconstructed from SANS patterns. The NSLD of the different parts of the molecules are computed before the construction of density map. Similar to estimation of electron density, the minidendron is divided into aromatic core (benzoate group, lithium ion and

oxygen spacer) and alkyl tails and unitary crystal volume is used to computed the volumes[9]. At room temperature, nonadecane shows rotator phase and the volume of $C_{19}D_{40}$ is calculated from the density at room temperature[8]. The results of NSLD are listed in Table 6.6. It shows that added deuterated alkane has the highest NSLD. The NSLD of the aromatic core of the minidendron is 45% lower than that of $C_{19}D_{40}$. The alkyl tails have near zero NSLD, in fact slightly negative.

Table 6.6 The neutron scattering length density of different part of 12-12-12Li and $C_{19}D_{40}$

12-12-12Li	Volume/molecule (nm^3)	coherent neutron scattering length (fm)	neutron scattering length density ($10^{-6}/Å^2$)
aromatic parts* (+ oxygen spacer)	0.17	65.85	3.94
alkyl tails*	0.91	-41.10	-0.45
12-12-18Li	Volume/molecule (nm^3)	coherent neutron scattering length (fm)	neutron scattering length density ($10^{-6}/Å^2$)
aromatic parts* (+ oxygen spacer)	0.17	65.85	3.94
alkyl tails*	1.06	-41.10	-0.39
$C_{19}D_{40}$	0.57	393.19	6.93

* The volume is estimated by unitary crystal volumes[9]

(a)

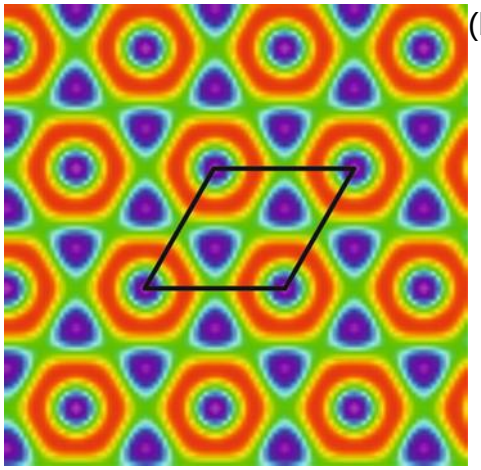

(b)

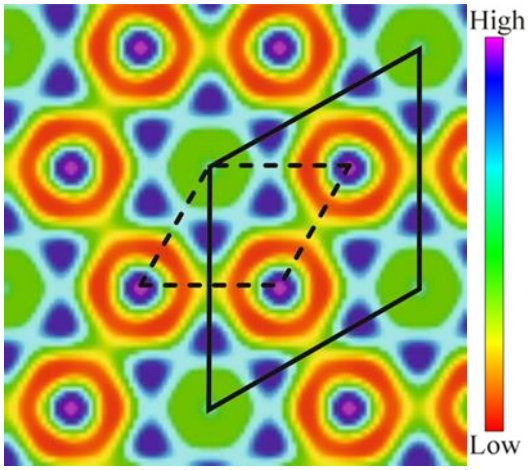

	plane	intensity	phase
Colh	(10)	10.23	π
	(11)	100.00	0
	(20)	12.34	0

	plane	intensity	phase
Col**s**	(10)	36.52	0
	(11)	4.70	π
	(20)	28.08	π
	(21)	23.92	π
	(30)	100.00	0
	(22)	12.32	0

(c)

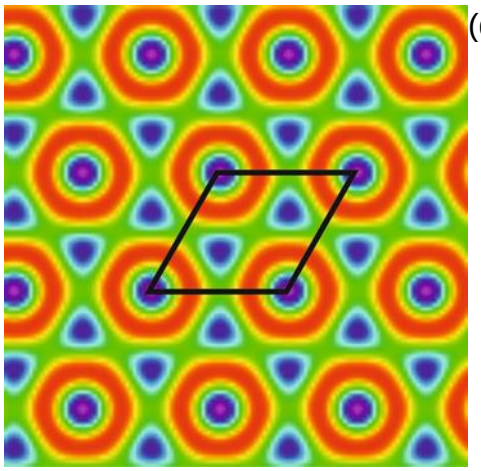

(d)

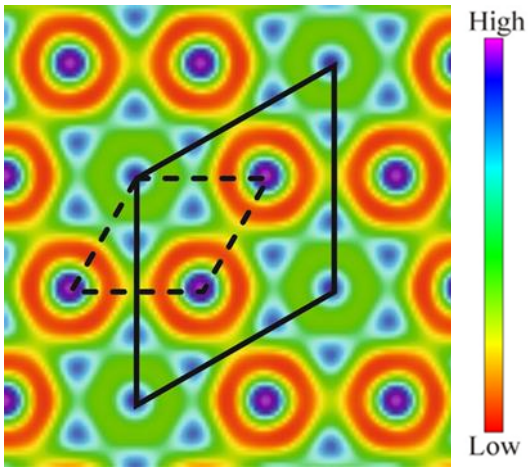

	plane	intensity	phase
Colh	(10)	3.40	π
	(11)	100.00	0
	(20)	18.28	0

	plane	intensity	phase
Col**s**	(10)	35.61	0
	(20)	12.16	π
	(21)	10.77	π
	(30)	100.00	0
	(22)	18.32	0

Figure 6.9 The contour of reconstructed NSLD maps of 12-12-12Li + 20wt% $C_{19}D_{40}$ in the (a) Colh phase and (b) superlattice. NSLD map of 12-12-18Li + 20wt% $C_{19}D_{40}$ in the (c) Colh phase and (d) superlattice phase.

The NSLD maps of 12-12-12Li + 20wt% $C_{19}D_{40}$ in the Colh phase and the superlattice are displayed in Figure 6.9 (a) and (b). In the Colh phase, it is similar to the ED map, every column is identical and composed of high density core and low density periphery. However, between the columns, the spaces are occupied by high density triangles. Since $C_{19}D_{40}$ has the highest NSLD, the high density triangles should come from the added d-alkane. That means in the Colh phase, the added alkanes evenly distribute between the columns. The NSLD map of 12-12-18Li + 20wt% $C_{19}D_{40}$ in the Colh phase (Figure 6.9 (c)) shows similar features. High density triangles in the spaces between columns mark the positions of $C_{19}D_{40}$ aggregating around the coronas of the columns.

In the superlattice, the NSLD maps (Figure 6.9 (b) and (d)) show that wide columns look like the column in the Colh phase, which consist of larger high density core and low density periphery. Other possible phase combination of the density maps in superlattice are in Appendix. That means the apex groups of the minidendron micro-segregate together and pack into supramolecular columns. The alkyl tails are relegated to the corona regions. However, the narrow column is quite dissimilar. The high density central region is still smaller than wide column. This is due to the smaller number of molecules in the narrow columns. But, the density of corona region is higher than the density of the wide column corona. Also, the high density triangles are located closer to the centres of the narrow columns. That means that the d-alkane aggregates preferentially around the narrow columns and mixes more with the alkyl tails of the minidendrons in the narrow columns, raising the average NSLD of their corona. Thus the added paraffin compensates for the shortfall of material in the 2-dendron columns, helping to alleviate lattice strain in an array of mixed-size columns. That explains why the superlattice phase can be stabilised and observed in these minidendron-alkane blends.

As noted before, in both 12-12-12Li and 12-12-18Li blends, the formation of the superlattice is accompanied by the shrinkage of diameter of the columns. As noted above, the Colh phase consists of 3-dendron columns. But, approaching the phase transition temperature, the taper angle of the minidendrons would expand[1] due to the conformational disorder of the alkyl chains. In some columns, the surplus minidendron is expected to be expelled from its original

stratum leaving only two minidendrons and a thinner column. These two different kinds of columns then arrange on a lattice with *p*6*mm* symmetry, rather than in a random fashion. To explain the continuous shrinkage of the superlattice, we propose that the occupancy of the 3-dendron and 2-dendron sublattices are not 100%, but vary with rising temperature. It is possible also that a lattice inversion occurs at higher temperatures, with the 3-3-2 superlattice cell being replaced by a 3-2-2 type.

Based on the above information, molecular models of 12-12-12Li + $C_{19}D_{40}$ blends in the Colh and superlattice phases were built using Materials Studio. Here, the lattice parameter are all doubled to optimise the distribution of the molecules. The periodic box consists of two strata. The molecules in the upper layer are coloured pink and those in the bottom layer red. In the Colh model, there are 3 minidendrons per layer and two adjacent layers are rotated by 60°. The alkane tails of most minidendrons are in all *trans*-conformation. The added alkane molecules (marked green) are inserted between the columns and every two layers share three free alkane molecules. The model is minimized by the minimizer in ForcitePlus module. Then the system was subjected to five molecular dynamics annealing cycles between 300 to 700 °C again using the ForcitePlus module and the Universal force field. The resulting models are displayed in Figure 6.10 (a). We can see that the free alkane surround the outer region of the columns and is uniformly dispersed between them.

In the superlattice phase, the lattice parameter of the model is doubled as well. In an original unit cell, two 3-dendron columns are placed in the centre and one 2-dendron column at the corner. The successive layers in the 3-dendron columns are rotated by 60° and in 2- dendron columns by 90°. The as-built model is first energy minimized and then MD annealed as before. Figure 6.10 (b) shows the molecular model of the superlattice. Most of the free alkane is mixed into the 2-dendron columns and some is found in the gaps between the 2-dendron column and 3-dendron column.

(a) Colh phase

(b) superlattice phase

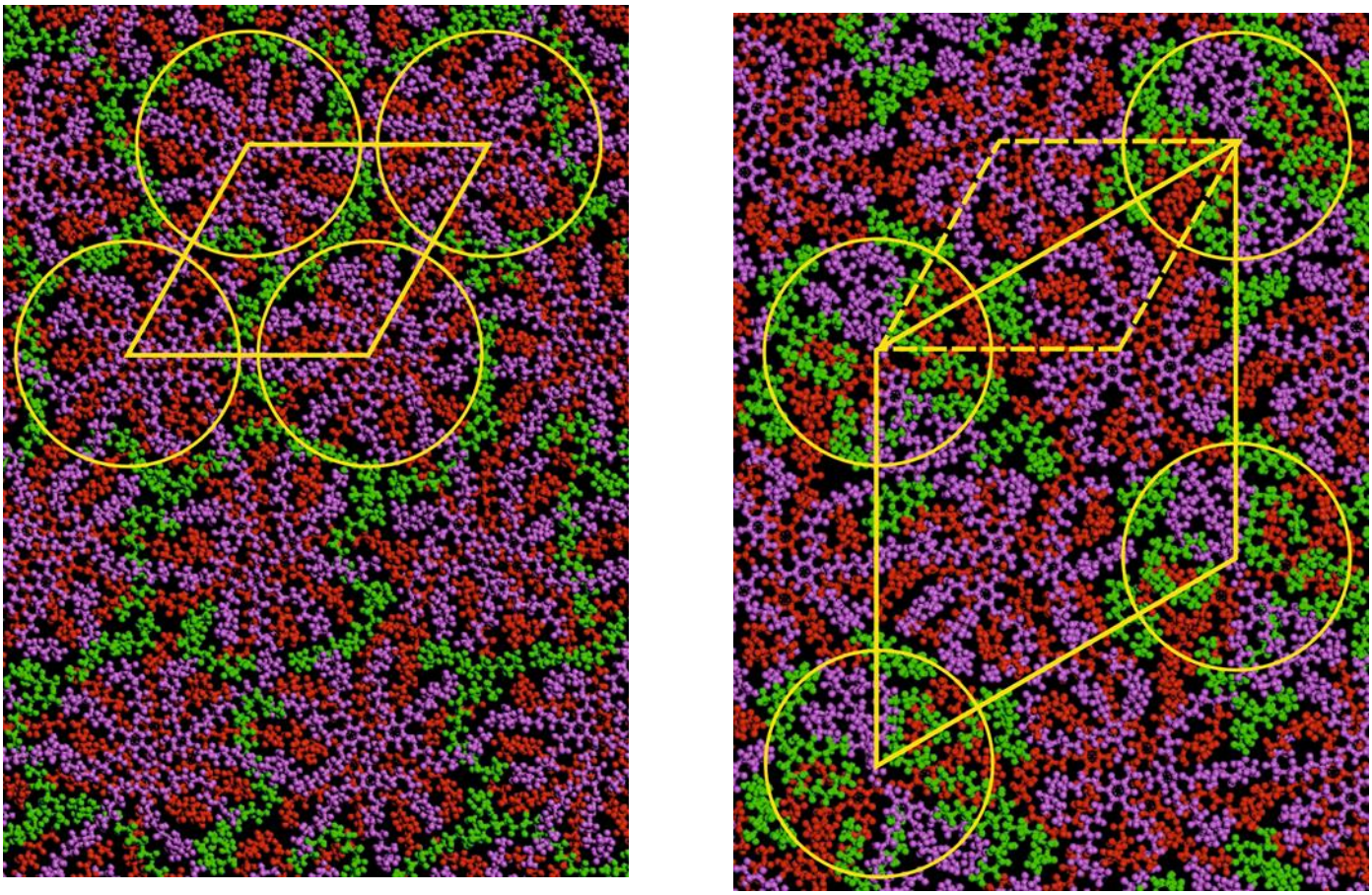

Figure 6.10. Simulation results of 12-12-12Li + $C_{19}D_{40}$ in the (a) Col-h and (b) superlattice phase. Notice that there are two layers of the discs. (pink: upper layer, red: bottom layer, green: d-alkane)

The projections of the Colh and Cols phases on the xy plane are also depicted schematically in Figure 6.11. The minidendrons are pink and the added alkane chains are green. The sketch is self-explanatory.

(a) Colh phase

(b) superlattice phase

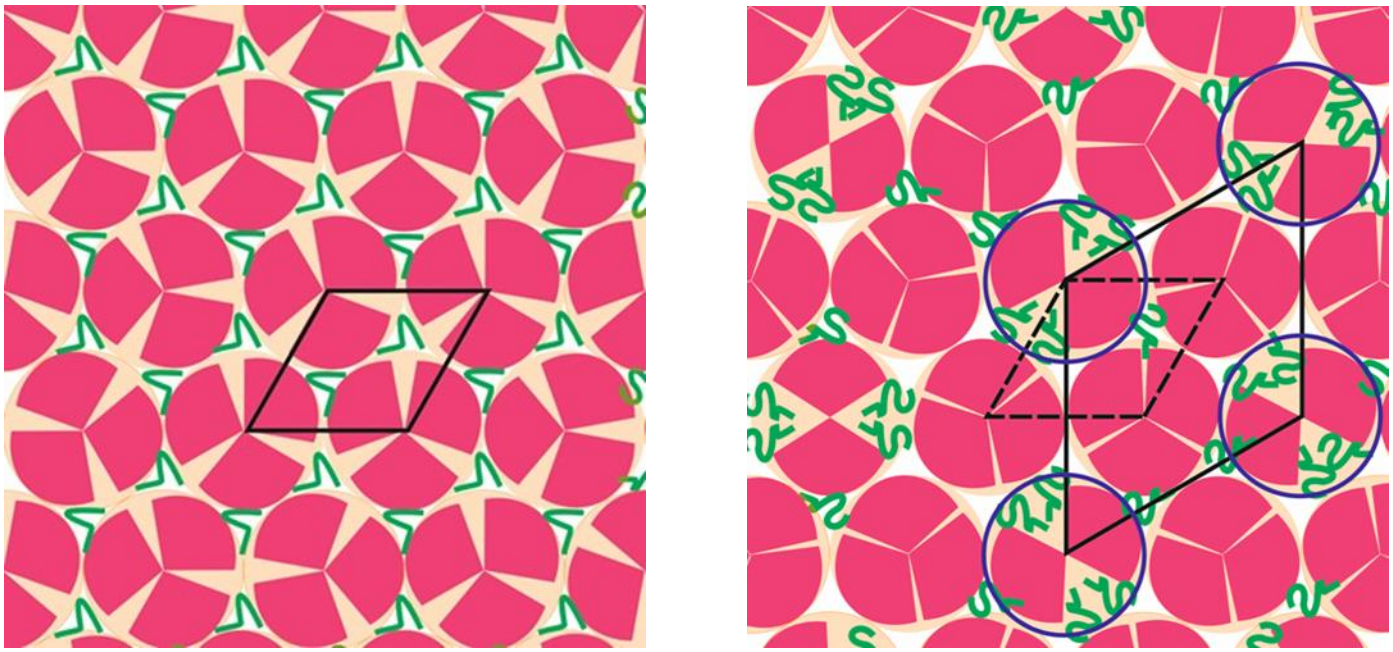

Figure 6.11.The schematic Li 3,4,5-trialkoxybenzoate salts and n-alkane blends in the (a) Col-h and (b) superlattice phases. (pink: minidendrons; green: n-alkane)

6.4 Conclusion

A superlattice in the Li minidendron + n-alkane blends was observed at higher temperature range than the Col-h phase. The added alkanes disperse uniformly between the columns in the Col-h phase. Nonetheless, the conformation disorder of the alkyl tails of the dendron at higher temperature leads the taper angle of the dendrons expands laterally. An excess molecule is expelled from the disc in some columns and it results in unequal number of molecules in each column. The wide columns and narrow columns are self-organized into columnar hexagonal structure. The shortfall of the volume in the narrow columns is compensated by the added alkane and they segregate around the narrow columns rather than distribute evenly. The lattice strain is therefore alleviated by the added alkane. It shows how addition of a dopant may provide a way of creating and stabilizing novel complex LC superstructures.

Reference

1. Ungar, G.; Percec, V.; Holerca, M. N.; Johansson, G.; Heck, J. A., Heat-shrinking spherical and columnar supramolecular dendrimers: Their interconversion and dependence of their shape on molecular taper angle. *Chem. Eur. J.* **2000,** 6, (7), 1258-1266.

2. Liu, Y. S. Two- and three-dimensional liquid crystalline structures in self-assembled supramolecular dendrimers. University of Sheffield, 2004.

3. Percec, V.; Holerca, M. N.; Uchida, S.; Cho, W. D.; Ungar, G.; Lee, Y. S.; Yeardley, D. J. P., Exploring and expanding the three-dimensional structural diversity of supramolecular dendrimers with the aid of libraries of alkali metals of their AB(3) minidendritic carboxylates. *Chem. Eur. J.* **2002,** 8, (5), 1106-1117.

4. Chaiprapa, J. New supramolecular liquid crystal structures in wedge-shaped molecules. Univ. of Sheffield, 2012.

5. Kanie, K.; Matsubara, M.; Zeng, X. B.; Liu, F.; Ungar, G.; Nakamura, H.; Muramatsu, A., Simple Cubic Packing of Gold Nanoparticles through Rational Design of Their Dendrimeric Corona. *J. Am. Chem. Soc.* **2012,** 134, (2), 808-811.

6. Yeh, M. C.; Su, Y. L.; Tzeng, M. C.; Ong, C. W.; Kajitani, T.; Enozawa, H.; Takata, M.; Koizumi, Y.; Saeki, A.; Seki, S.; Fukushima, T., Amphiphilic design of a discotic liquid-crystalline molecule for dipole manipulation: hierarchical columnar assemblies with a 2D superlattice structure. *Angew. Chem. Int. Ed.* **2013,** 52, (3), 1031-1034.

7. Orwoll, R. A.; Flory, P. J., Equation-of-state parameters for normal alkanes. Correlation with chain length *J. Am. Chem. Soc.* **1967,** 89, (26), 6814-6822.

8. http://www.chemicalbook.com/ChemicalProductProperty_EN_CB0269216.htm.

9. Immirzi, A.; Perini, B., Prediction of density in organic crystals. *Acta Cryst.* **1977,** A33, 216-218.

10. http://www.ncnr.nist.gov/resources/n-lengths/.

Future Work

- In the Colh-Colh phase transition, the molecular models in Colh-**1** and Colh-**2** are built. However, there are still other possibilities for these two phases. The fibre WAXS pattern can be simulated from the built models. Comparing with the simulation results and the experimental data, the most probable detailed model can be chosen in these two phases. This would allow a more detail understanding of the packing of molecules in the two phases.
- The HCP phase in minidendron-alkane blends exemplifies the formation of close packed structures in tapered mesogens. This knowledge can be used in designing the shape of mesogens forming FCC or HCP phases.
- The binary phase diagram of 12-12-12Li + nonadecane and 12-12-18Li + nonadecane can be constructed based on the experimental results.

Appendix

A1. Other possible phase combination of electron density map of 12-12-12Li + 20wt% $C_{19}D_{40}$ in the superlattice phase (see Chapter 6). The symbol + is represented phase 0 of (hk) flection and – is π. The sequence is (10), (11), (20), (21), (30), (22). Only half of the combinastions are shown, others are inverse.

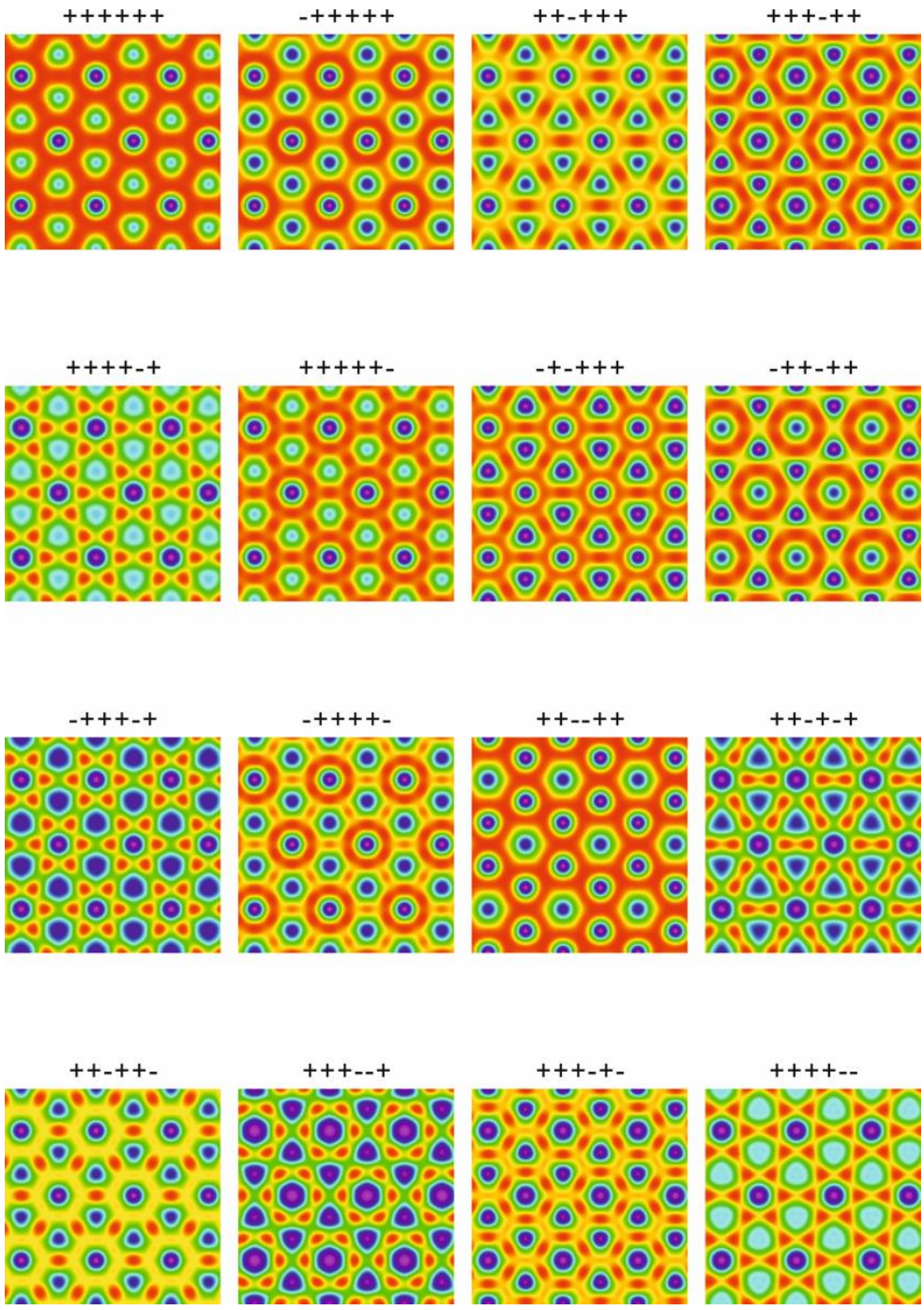

-+-+-+

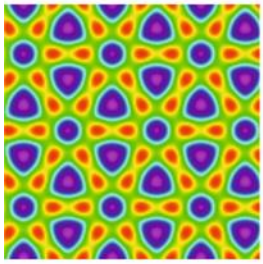

-+-++-

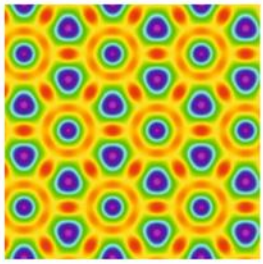

-++--+

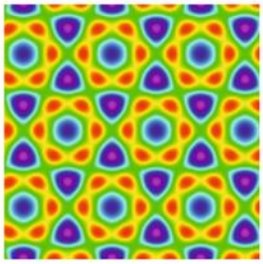

-++-+-

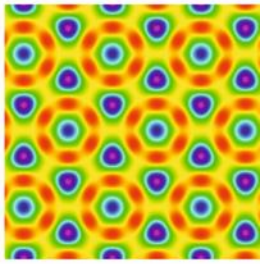

-+++--

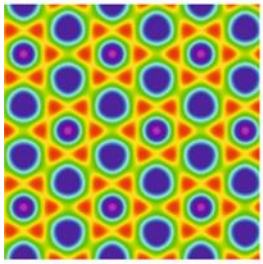

++---+

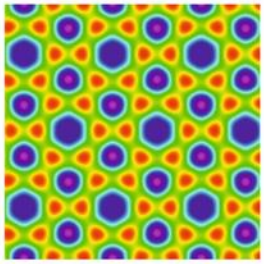

++--+-

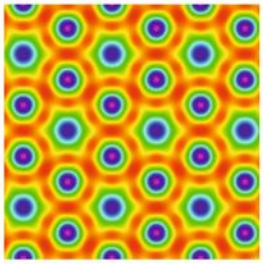

++-+--

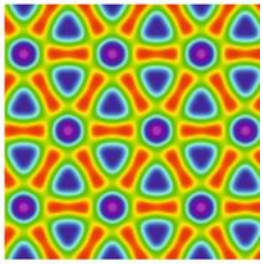

+++---

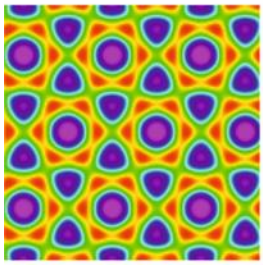

-+---+

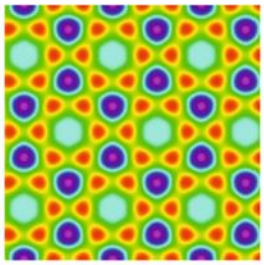

-+--+-

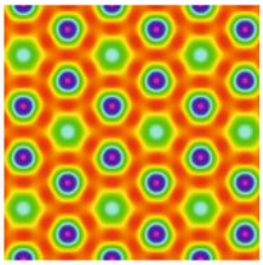

-+-+--

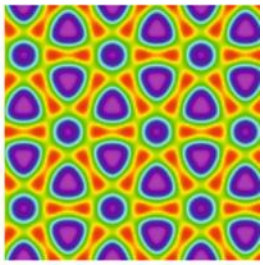

-++---

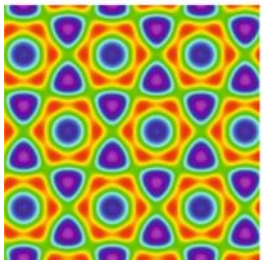

++----

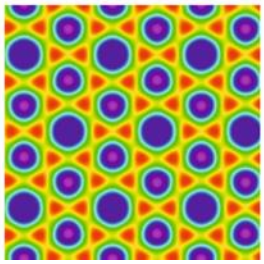

-+----

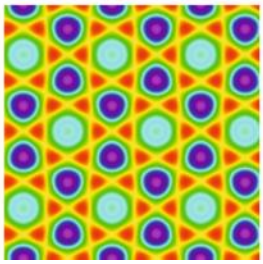

A2. Other possible phase combination of neutron scattering length density map of 12-12-12Li + 20wt% $C_{19}D_{40}$ in the superlattice phase (see Chapter 6). Others are inverse or show unreasonable high-low contrast.

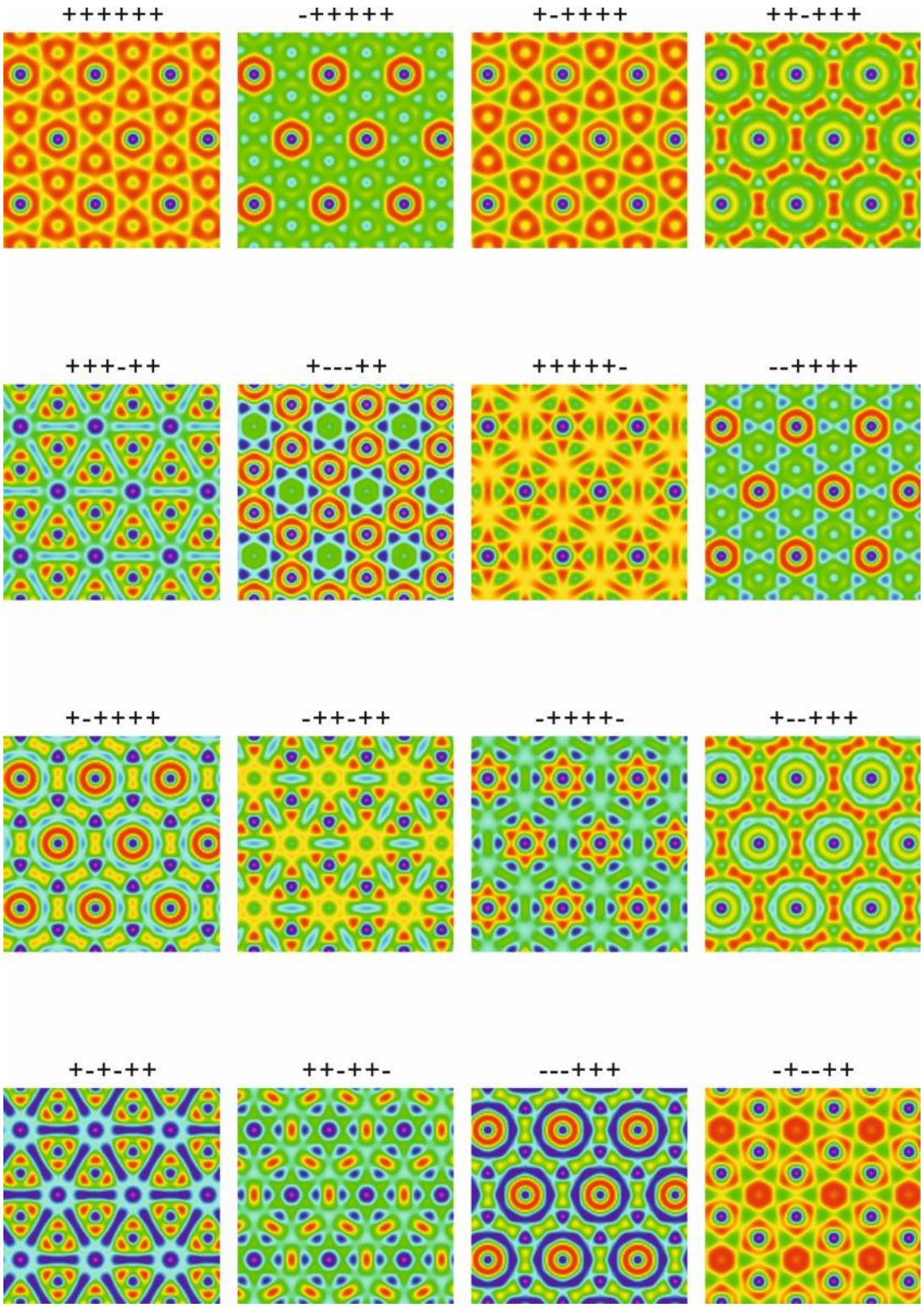

A3. The following data were contributed by our previous colleagues

Experiments performed by Yongsong Liu:

SAXS	12-12-12Li
	12-12-12Na
	12-12-12Rb

Experiments performed by Jitrin Chaiprapa:

SAXS	12-12-12Na + 15% $C_{19}H_{40}$
	12-12-12Rb + 15% $C_{19}H_{40}$
	12-12-18Na
	12-12-18Li
	12-12-18Li + 30% $C_{17}H_{36}$